

Dissertation
submitted to the
Combined Faculties for the Natural Sciences
and for Mathematics
of the Ruperto-Carola University of Heidelberg,
Germany
for the degree of
Doctor of Natural Sciences

presented by
Magister rer.nat. Alexander Kasper
born in: Innsbruck, Austria
Oral examination: 17th December 2003

**Bose-Einstein condensation in a
robust microtrap – the
combination of wire traps and
atom chips**

Referees:

**Prof.Dr. Jörg Schmiedmayer
Prof.Dr. Andreas Wolf**

Zusammenfassung

Bose-Einstein condensation in a robust microtrap – the combination of wire traps and atom chips

In der hier vorgelegten Arbeit wird die erfolgreiche Erzeugung eines Bose-Einstein Kondensats von Rubidium Atomen in einer magnetischen Mikrofalle beschrieben. Die verwendeten Mikrofallen, sogenannte Drahtfallen, werden durch einfache Drähte und homogene Magnetfelder erzeugt. Diese Drahtfallen erlauben es Magnetfallen zu erzeugen, die sich besonders gut zur Bose-Einstein Kondensation eignen. Desweiteren können sehr komplexe Fallengeometrien erzeugt werden, die die magnetische manipulation ermöglichen. Wir kombinieren makroskopische mit mikroskopischen Drahtfallen. Die mikroskopischen Drahtfallen werden durch den sogenannten Atom-chip realisiert (vergleichbar mit einer Leiterplatte aus der Elektronik), die makroskopischen Drahtfallen werden durch eine massive Kupferstruktur erzeugt. Die Leiterstrukturen auf dem Atom-chip realisieren in Zukunft die eigentlichen Experimente. Diese Kombination erlaubte es uns, einen Kondensationszyklus in der makroskopischen Drahtfalle zu entwickeln, der unabhängig von den Strukturen des Atom Chips ist.

Desweiteren werden erste Experimente mit einem Bose-Einstein Kondensat vorgestellt.

Abstract

Bose-Einstein condensation in a robust microtrap – the combination of wire traps and atom chips

In the presented work, we report about the successful creation of a Rubidium Bose-Einstein condensate. We use so called magnetic wire traps, which are especially simple, as they consist out of a wire and a homogeneous bias field. These wire traps are especially suited for Bose-Einstein condensation. Furthermore complex trapping potentials to manipulate a Bose-Einstein condensate can be realized. We combine 'large' and small scale wire traps. The 'large' scale is realized with a massive copper structure, while for the small wire traps we use the so called atom chip. This combination is promising, because it allowed us to develop a condensation process in the copper structure, which is independent of the structures on the atom chip, and thus the exchange of the 'physics' area.

First experiments with the Bose-Einstein condensate are presented and discussed in detail.

Introduction

In the beginning of the last century quantum theory was developed. The development of the new theory had a massive impact, not only onto the view of the world in a physical sense, but it also effected the daily life view. Over a relatively short period, quantum physics was well established, due to the innumerable examples of experimental verifications.

One major discovery (among others) was made in 1924. In this year the Indian physicist Satyendra Nath Bose established a new way of 'counting' photons (the Bose statistics) [1]. Einstein realized, that this statistics could also be applied to atoms [2, 3]. When he studied the new statistics for low temperatures, the thermodynamical limit gives a wrong result - it seemed, that below a certain temperature the density decreased. To overcome this problem, he had to tread the lowest energy term separately, and with this approach he got the right result. This actually means, that the ground state is macroscopically populated!

In these early days, there was no way to investigate this new phenomenon experimentally. It took over seventy years until this new state of matter could be experimentally realized. The laser had to be developed and laser cooling, starting from slowing atomic beams to the development of the magneto optical trap, had to be established [4, 5, 6]. In 1997 Steven Chu, Claude N. Cohen-Tannoudji and William D. Phillips got the Nobel Prize for their contribution to this field. Further on magnetic traps, to confine atoms had to be constructed until it was possible to reach temperatures where this phenomenon became experimentally visible [7]. The development of the evaporation technique [8, 9] was the last step which made it possible to increase the phase space density over the critical value $n\lambda_{dB}^3 \approx 1$ (n is the particle density and λ_{dB} is the de Broglie wave length of the particles). Above this critical value Bose-Einstein condensation sets in. The macroscopic population of the ground state was first observed in ^{87}Rb [10], followed by ^{23}Na and ^7Li [11, 12]. Over the years, experiments succeeded in condensing H, He^* , K, Cs and Yb [13, 14, 15, 16, 17, 18, 19].

The condensation process was studied in detail, and the theoretical understanding was improved. The Bose-Einstein condensate was subsequently manipulated with magnetic and optical fields, and experiments showing the matter wave nature were performed. In 2001 Eric Cornell, Carl Wieman and Wolfgang Ketterle earned the Nobel Price for their achievements in the field of Bose-Einstein condensation.

In 1995 an experiment was performed, which used a wire [20, 21] for trapping a neutral atoms. Then in 1998/99 groups [22, 23, 24] succeeded in the development of more complex trapping structures, which were remarkable

simple. These wire traps used just a single wire and a homogeneous bias field for realizing a magnetic trap. Soon it became clear, that this approach opened a new door to manipulate atoms. The first experiments were performed with thermal atoms. Different trapping potentials were realized in order to guide atoms (see [25] and references therein). This development was followed by the first creation of a Bose-Einstein condensates in such a magnetic microtrap [26, 27]. The creation of a Bose-Einstein condensate strengthened the position of wire traps. Since then, several groups work in this field and developed setups with this new kind of traps.

In the presented work [28, 29], we developed a setup, which combines 'large' and microscopic scale wire traps. This combination consists of a massive copper structure and the atom chip, which houses small wire structures. With such a combination we established a robust condensation procedure in the copper wire, independent of the atom chip. This has the advantage, that the change of the atom chip, containing wires to realize more complex experiments, is easy and fast.

The aim of the presented work was the development and the investigation of magnetic wire traps to establish a Bose-Einstein condensate as well as to prove the flexibility of the atom chip concept.

Contents

1	Bose-Einstein condensation	1
1.1	Basic considerations	1
1.2	Bose-Einstein condensation at finite temperatures	3
1.3	Finite particle number	6
1.4	Interacting atoms - the Gross-Pitaevskii equation	7
1.4.1	Thomas-Fermi approximation	10
1.5	Basic properties of a BEC	12
1.5.1	Free expansion of a Bose-Einstein condensate	12
1.5.2	Exciting oscillations	16
2	Laser cooling	23
2.1	Doppler cooling	23
2.2	Magneto-optical trap	26
2.3	Polarization gradient cooling	27
3	Magnetic trapping	31
3.1	Atom - magnetic/electric field interaction	31
3.2	Magnetic microtraps	33
3.2.1	A straight wire and a bias field	34
3.2.2	Creating three dimensional traps with wires	36
3.2.3	Finite size effects of real wires	41
3.2.4	Trap losses and heating	45
3.3	Evaporative cooling	48
4	Experimental realization	53
4.1	Trapping, transferring and pre-cooling atoms	53
4.1.1	The laser system	54
4.1.2	The double MOT apparatus	66
4.1.3	The atom chip holder	68
4.1.4	The atom chip - basic concepts	72

4.1.5	The mirror MOT	73
4.1.6	The atom transfer	75
4.2	Measuring atom numbers and temperature	77
4.2.1	The fluorescence method	77
4.2.2	The absorption method	79
4.2.3	Temperature measurement	81
4.2.4	The imaging system	82
4.2.5	Interpretation of the pictures	84
4.3	Creating a Bose-Einstein condensate	86
4.3.1	Generating the magnetic fields	87
4.3.2	The U mirror MOT	89
4.3.3	The Molasses phase	91
4.3.4	Loading the magnetic trap	94
4.3.5	Obtaining a Bose-Einstein condensate	97
5	First experiments	111
5.1	Free expansion and collective shape oscillations	112
5.2	Basics studies of the transfer to the atom chip	117
5.3	Two wire trap	122
6	Summary and outlook	127
A	^{87}Rb line data	131
B	The vacuum chamber	133
C	The H structure	135
D	Complex analytical expressions	137
E	Power supplies and noise	139
F	Computer control	143
	Bibliography	156

Chapter 1

Bose-Einstein condensation

In this chapter we will summarize the theoretical fundament of Bose-Einstein condensation in dilute gases. We will derive several basic properties of the Bose-Einstein condensate, which show its uniqueness and its difference from an 'ordinary' thermal gas. These properties can be related to experimentally observable, and they allow us to detect the state the atoms are in. The condensation process itself is described as a quantum statistical phase transition [1, 2, 3], where we find a macroscopic population of the ground state. This occurs below a certain critical temperature T_C . That the atoms populate the ground state macroscopically is a result of the bosonic character of the sample. Fermions in contrast do not show such behavior. In the following chapter we will mainly follow the derivation given in [30] and [31].

1.1 Basic considerations

Before we are going to derive basic quantities of a Bose-Einstein condensate and the condensation process itself, we want to consider the case, where we have already a macroscopic population of the ground state (a Bose-Einstein condensate).

We start this discussion by assuming that the atoms do not interact and that the sample is confined in a harmonic trap of the form

$$V_{ext}(r) = \frac{m}{2}(\omega_x x^2 + \omega_y y^2 + \omega_z z^2), \quad (1.1)$$

where m is the atomic mass and $\omega_{i=x,y,z}$ are the oscillator frequencies. This potential is relevant since the confining traps used in the experiment can be safely approximated as harmonic potentials (at least for low temperatures;

a detailed discussion of the used trapping potentials can be found in section 3.2.2). For noninteracting particles the many-body Hamiltonian can be written as a sum of single-particle Hamiltonians with the eigenvalues

$$\varepsilon_{n_x n_y n_z} = \left(n_x + \frac{1}{2}\right) \hbar \omega_x + \left(n_y + \frac{1}{2}\right) \hbar \omega_y + \left(n_z + \frac{1}{2}\right) \hbar \omega_z, \quad (1.2)$$

where $\{n_x, n_y, n_z\}$ are non-negative integers. To obtain the ground state $\phi(r_1 \dots r_N)$ for N noninteracting bosons confined in a potential of the form of equation 1.1, we consider all atoms to be in the lowest single-particle state ($n_x = n_y = n_z = 0$), which is $\phi(r_1 \dots r_N) = \prod_i \varphi_0(r_i)$, where φ_0 is

$$\varphi_0(r) = \left(\frac{m\omega_{ho}}{\pi\hbar}\right)^{3/4} \exp\left[-\frac{m}{2\hbar}(\omega_x x^2 + \omega_y y^2 + \omega_z z^2)\right], \quad \omega_{ho} = (\omega_x \omega_y \omega_z)^{1/3} \quad (1.3)$$

where ω_{ho} is the geometric average of the trap frequencies. We can write the density distribution as $n(r) = N|\varphi_0(r)|^2$. The average size of the Gaussian distribution of equation 1.3 is

$$a_{ho} = \left(\frac{\hbar}{m\omega_{ho}}\right)^{1/2}. \quad (1.4)$$

This quantity we will note as the harmonic oscillator ground state size. Equation 1.4 is independent on N and that it is only valid for noninteracting particles.

Consider the case of a thermal cloud $k_B T \gg \hbar \omega_{ho}$ and using the classical Boltzmann distribution $n_{cl} \propto \exp(-V_{ext}(r)/k_B T)$, where V_{ext} is the confining potential from equation 1.1. With this thermal cloud we get a Gaussian width of

$$R = a_{ho}(k_B T / \hbar \omega_{ho})^{1/2}, \quad (1.5)$$

and we find that R is larger than a_{ho} .

This discussion reveals, that when we have a Bose-Einstein condensate, the atoms will appear on a length scale of a_{ho} , in contrast, thermal atoms will be distributed on a length scale R . When we calculate the Fourier transform

of the ground state wave function we have access to the momentum distribution of the trapped atoms. Here we find that the momentum width of a thermal cloud is again wider than the width of the Bose-Einstein condensate.

Up to now we considered isotropic traps, but in our experiment (and in most of the others) the trap is cigar-shaped, with an axial oscillator frequency of ω_x and a radial oscillator frequency $\omega_\perp = \omega_y = \omega_z$. Rewriting equation 1.3, we get

$$\varphi_0(r) = \frac{\lambda^{1/4}}{\pi^{3/4} a_\perp^{3/2}} \exp \left[-\frac{1}{2a_\perp^2} (r_\perp^2 + \lambda x^2) \right], \quad (1.6)$$

where $r_\perp = (y^2 + z^2)^{1/2}$, $\lambda = \omega_x / \omega_\perp$ (the aspect ratio) and $a_\perp = (\hbar / m\omega_\perp)^{1/2}$ denotes the harmonic oscillator length in the yz plane.

If we take the Fourier transform of equation 1.6, we can determine the momentum distribution of the atoms for the different directions (radial and longitudinal). The momentum ratio of the different directions is:

$$\sqrt{\langle p_x^2 \rangle / \langle p_\perp^2 \rangle} = \sqrt{\lambda}. \quad (1.7)$$

When we switch off the confining potential, the expansion will be an ellipse. In contrast to this, the distribution for a thermal cloud (here the atoms are distributed over many eigenstates of higher energy) would be isotropic, according to the equipartition principle. Here we would find a aspect ratio of 1. In other words, a thermal cloud does not 'remember' its confining trap.

1.2 Bose-Einstein condensation at finite temperatures

In the grand-canonical ensemble, the number of atoms at a given temperature T is the sum

$$N = \sum_{n_x, n_y, n_z} \frac{1}{\exp[\beta(\varepsilon_{n_x n_y n_z} - \mu)] - 1}, \quad (1.8)$$

where μ is the chemical potential, $\beta = (k_B T)^{-1}$ (k_B is the Boltzmann constant) and the expression is the Bose distribution. The total energy is

given by

$$E = \sum_{n_x, n_y, n_z} \varepsilon_{n_x n_y n_z} \frac{1}{\exp[\beta(\varepsilon_{n_x n_y n_z} - \mu)] - 1}. \quad (1.9)$$

We can now separate the lowest eigenvalue ε_{000} from the sum 1.8, and introduce N_0 as the number of atoms in this state. It is now interesting, that N_0 can become macroscopic, when the chemical potential becomes equal to ε_{000} ,

$$\varepsilon_{000} = \frac{3}{2} \hbar \bar{\omega} \quad , \quad \bar{\omega} = (\omega_x + \omega_y + \omega_z)/3 \quad (1.10)$$

$$\mu \rightarrow \mu_C = \frac{3}{2} \hbar \bar{\omega} \quad (1.11)$$

where $\bar{\omega}$ is the arithmetic average of the trap frequencies. Separating out 1.10 we get from equation 1.8

$$N - N_0 = \sum_{n_x, n_y, n_z \neq 0} \frac{1}{\exp[\beta \hbar (\omega_x n_x + \omega_y n_y + \omega_z n_z)] - 1}. \quad (1.12)$$

With $N \rightarrow \infty$ the discrete level spacing can be neglected and the sum in equation 1.12 can be rewritten by an integral

$$N - N_0 = \int_0^\infty \frac{dn_x dn_y dn_z}{\exp[\beta \hbar (\omega_x n_x + \omega_y n_y + \omega_z n_z)] - 1}. \quad (1.13)$$

Equation 1.13 is valid when N is large and $k_B T \gg \hbar \omega_{ho}$. Integrating equation 1.13 leads to

$$N - N_0 = \zeta(3) \left(\frac{k_B T}{\hbar \omega_{ho}} \right)^3, \quad (1.14)$$

where $\zeta(n)$ is the Riemann ζ function. From equation 1.14 the transition temperature T_C can be derived, by putting $N_0 \rightarrow 0$ at the transition, and

we get

$$k_B T_C = \hbar \omega_{ho} \left(\frac{N}{\zeta(3)} \right)^{1/3} = 0.94 \hbar \omega_{ho} N^{1/3}. \quad (1.15)$$

For equation 1.15, we use the thermodynamical limes $N \rightarrow \infty$ and $\omega_{ho} \rightarrow 0$ (keeping the product $N\omega_{ho}$ constant). If we insert equation 1.15 into equation 1.14 we get

$$\frac{N_0}{N} = 1 - \left(\frac{T}{T_C} \right)^3. \quad (1.16)$$

Equation 1.16 means, that for $T < T_C$ the particle number in the ground state rises with the power to the 3, and for $T = 0$ it is 1.

Another approach to the presented results is, to consider the density of states instead. The number of states is proportional to the volume between two surfaces of energy ε and $\varepsilon + d\varepsilon$. When we calculate the density of states, the volume is determined by the confining potential $V(r)$, and we find [32]

$$\rho(\varepsilon) = \frac{2\pi(2m)^{3/2}}{h^3} \int_{\overline{V(\varepsilon)}} \sqrt{\varepsilon - V(r)} d^3r, \quad (1.17)$$

where $\overline{V(\varepsilon)}$ is the reachable volume with the energy ε . Integrating this for a box potential gives

$$\rho(\varepsilon) = \frac{V}{2\pi} \left(\frac{2m}{\hbar^2} \right)^{3/2} \sqrt{\varepsilon}. \quad (1.18)$$

We can in principle derive the same quantities with the density of states approach as we did with the grand-canonical ensemble. Note here that equation 1.18 varies of the form $g(\varepsilon) = C_\alpha \varepsilon^{\alpha-1}$, where α is the dimension of the problem, which is the case for many situations.

We start with

$$N = N_0 + \int_0^\infty d\varepsilon \rho(\varepsilon) f^0(\varepsilon), \quad (1.19)$$

where $f^0(\varepsilon)$ is the occupation number of particles in a specific energy level ε . Investigating the transition temperature T_C , we can neglect the fractions of atoms in N_0 and just compute the integral in equation 1.19 (it maximizes for $\mu=0$). This leads to

$$kT_C = \frac{N^{1/\alpha}}{[C_\alpha \Gamma(\alpha) \zeta(\alpha)]^{1/\alpha}}, \quad (1.20)$$

where $\Gamma(\alpha)$ is the gamma function and we used the more general form as stated above. With equation 1.20 we can now derive the transition temperature for different trapping potentials.

Another useful quantity is the phase-space density (PSD). It is defined as the number of particles in a volume λ_{dB}^3 ,

$$PSD = n\lambda_{dB}^3, \quad \lambda_{dB} = \left(\frac{2\pi\hbar}{mkT} \right)^{3/2}, \quad (1.21)$$

where λ_{dB} is the de Broglie wavelength and $n = N/V$ is the atom density. If we reduce T , λ_{dB} becomes larger and the phase-space density increases (keeping n constant). Combining equation 1.21 with 1.20 for the case $\alpha = 3/2$ we get the value for the phase transition to a Bose-Einstein condensate $PSD = \zeta(3/2) \approx 2.612$.

1.3 Finite particle number

When discussing the condensation process, we also have to include a finite particle number, as this is the situation we have in the laboratory. To calculate the properties of a Bose-Einstein condensate assuming a finite number of particles, we can carry out the sum 1.8 for a finite number N [33]. Here it turns out that the condensate fraction $N_0(T)/N$ is smaller than the prediction in equation 1.16. The effect of a finite particle number was found to be significant for $N < 10^4$ atoms [33]. Carrying out the sum analytically in equation 1.8 for the limit of large N [34], one finds a correction to equation 1.16,

$$\frac{N_0}{N} = 1 - \left(\frac{T}{T_C} \right)^3 - \frac{3\bar{\omega}\zeta(2)}{2\omega_{ho}\zeta(3)^{2/3}} \left(\frac{T}{T_C} \right)^2 N^{-1/3}. \quad (1.22)$$

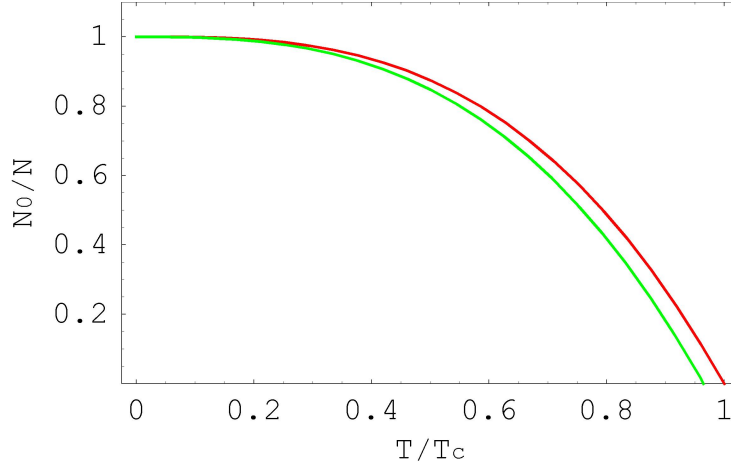


Figure 1.1: Condensate fraction versus temperature: the red curve shows equation 1.16, while the green curve represents equation 1.22 (both for an ideal gas, $N = 1000$). The effect of a finite atom number (green curve) is expressed in a reduced condensate fraction. However, when the atom number is increased, we find that the green curve approaches the ideal gas calculations.

We see that the correction decreases with $N^{-1/3}$ to the lowest order and that it depends on the ratio of $\bar{\omega}/\omega_{ho}$. The finite atom number thus causes a shift of the onset of the macroscopic population of the ground state compared with the thermodynamical limit (see figure 1.1), meaning that it reduces the condensate fraction and as a result it reduces the transition temperature. The shift can be estimated by setting the left hand side of equation 1.22 to zero. The estimate we get is

$$\frac{\delta T_C}{T_C} = \frac{\bar{\omega}\zeta(2)}{2\omega_{ho}\zeta(3)^{2/3}} . \quad (1.23)$$

We see that the trap properties enter through the arithmetic and geometric averages of the oscillation frequencies of the confining trap.

1.4 Interacting atoms - the Gross-Pitaevskii equation

So far we treated the problem excluding interactions between the atoms. For a more realistic treatment we have to include the interactions. The

many-body Hamiltonian for N interacting particles (bosons) confined in an external potential $V_{ext}(r)$ can be written in second quantization as [30]

$$\begin{aligned} \hat{H} = & \int dr \hat{\Psi}^\dagger(r) \left[-\frac{\hbar^2}{2m} \nabla^2 + V_{ext}(r) \right] \hat{\Psi}(r) + \\ & \frac{1}{2} \int dr dr' \hat{\Psi}^\dagger(r) \hat{\Psi}^\dagger(r') V(r-r') \hat{\Psi}(r') \hat{\Psi}(r) , \end{aligned} \quad (1.24)$$

where $\hat{\Psi}(r)$ and $\hat{\Psi}^\dagger(r)$ are the boson field operators, which annihilate or create a particle at position r and $V(r-r')$ is the two-body interatomic potential (compare with equation 1.28). The field operators can be written as $\hat{\Psi}(r) = \sum_\alpha \Psi_\alpha a_\alpha$, where Ψ_α are the single particle wave functions and a_α are the corresponding annihilation operators. They fulfill the commutation relations

$$[a_\alpha, a_\beta^\dagger] = \delta_{\alpha,\beta} \quad , \quad [a_\alpha, a_\beta] = 0 \quad , \quad [a_\alpha^\dagger, a_\beta^\dagger] = 0 . \quad (1.25)$$

From equation 1.24 we can now again derive the relevant quantities, but for large numbers of N this can be difficult. Therefore, we use a mean field approach, which was first formulated by Bogoliubov [35]. The main idea here is to treat the condensate fraction and small perturbations to it like

$$\hat{\Psi}(r, t) = \Phi(r, t) + \hat{\Psi}'(r, t) , \quad (1.26)$$

where $\Phi(r, t) \equiv \langle \hat{\Psi}(r, t) \rangle$ is the expectation value of the field operator (in the Heisenberg representation). $\Phi(r, t)$ is a classical field, which is generally called the wave function of the Bose-Einstein condensate. Writing the time evolution of the field operator $\hat{\Psi}(r, t)$ using the Heisenberg equation and the Hamilton 1.24 simplifies to

$$\begin{aligned} i\hbar \frac{\partial}{\partial t} \hat{\Psi}(r, t) &= [\hat{\Psi}, \hat{H}] \\ &= \left\{ -\frac{\hbar^2 \nabla^2}{2m} + V_{ext}(r) + \int dr' \hat{\Psi}^\dagger(r', t) \right. \\ &\quad \left. \times V(r' - r) \hat{\Psi}(r', t) \right\} \hat{\Psi}(r, t) . \end{aligned} \quad (1.27)$$

The interaction potential in equation 1.27, in general complicated, can be replaced with a simple form, under the condition of a dilute, cold gas, where the energies are low. In this case the s-wave scattering length describes the system completely¹. Under these conditions the interaction potential $V(r - r')$ can be replaced by

$$V(r - r') = g\delta(r' - r) \quad , \quad g = \frac{4\pi\hbar^2 a}{m} \quad (1.28)$$

which have the same scattering length a as the real potential. With such an interaction potential, the Hamiltonian 1.24 becomes

$$\begin{aligned} \hat{H} = \int dr \left\{ -\hat{\Psi}^\dagger(r) \frac{\hbar^2}{2m} \nabla^2 \hat{\Psi}(r) + V_{ext} \hat{\Psi}^\dagger(r) \hat{\Psi}(r) \right. \\ \left. + \frac{g}{2} \hat{\Psi}^\dagger(r) \hat{\Psi}^\dagger(r) \hat{\Psi}(r) \hat{\Psi}(r) \right\} . \end{aligned} \quad (1.29)$$

We can now use this Hamiltonian for equation 1.27, and using 1.26 (neglecting $\hat{\Psi}'(r, t)$ corrections)

$$i\hbar \frac{\partial}{\partial t} \Phi(r, t) = \left(-\frac{\hbar^2 \nabla^2}{2m} + V_{ext}(r) + g|\Phi(r, t)|^2 \right) \Phi(r, t) . \quad (1.30)$$

This equation is called the Gross-Pitaevskii equation (GP) [37, 38].

Equation 1.30 is only valid in the dilute gas approximation, which means that the average density \bar{n} is small compared to the number of atoms in a volume $|a|^3$ (a the scattering length). However the condition $\bar{n}|a|^3 \ll 1$ means, that we have a dilute gas, but this does not necessarily imply a weakly interacting gas. In the interacting case we have to compare different energy scales with each other. For this it is convenient to derive the ground state of the system.

We write for the condensate wave function $\Phi(r, t) = \phi(r) \exp(-\mu t/\hbar)$, where μ is the chemical potential and $\phi(r)$ is real and normalized to the total number of atoms N_0 ($\int dr \phi^2 = N_0 = N$). Inserting this into equation 1.30

¹at the considered temperatures only the s-wave scattering contribute to the interaction potential [36]

leads to

$$\left(-\frac{\hbar^2 \nabla^2}{2m} + V_{ext}(r) + g\phi^2(r) \right) \phi(r) = \mu\phi(r) . \quad (1.31)$$

Equation 1.31 is of the form of a non-linear Schrödinger equation, where the non-linear character comes from the mean field term in the equation, which is proportional to the density of the atoms $n(r) = \phi^2(r)$. If we set $g = 0$, we obtain the known Schrödinger equation for a single particle. If we assume a spherical trap with trap frequencies ω_{ho} and if we rescale the equation using a_{ho} (length), a_{ho}^{-3} (density) and $\hbar\omega_{ho}$ (energy), we obtain

$$\left(-\tilde{\nabla}^2 + \tilde{r}^2 + \frac{8\pi a N}{a_{ho}} \tilde{\phi}^2(\tilde{r}) \right) \tilde{\phi}(\tilde{r}) = \tilde{\mu} \tilde{\phi}(\tilde{r}) , \quad (1.32)$$

where tilde denotes the rescaled quantities. In this notation the first term on the left hand side corresponds to the kinetic energy E_{kin} , the third term to the inter-action energy E_{int} . If we compare these energies we find

$$\frac{E_{int}}{E_{kin}} \propto \frac{Na}{a_{ho}} . \quad (1.33)$$

This ratio can be quite large, meaning a strongly interacting gas, while the dilute gas condition is still fulfilled $\bar{n}|a|^3 \ll 1$. Even though equation 1.33 is not fulfilled in most of the experiments, the Gross-Pitaevskii equation can be applied in most cases.

1.4.1 Thomas-Fermi approximation

In section 1.4 we discussed the different energy scales, and we found that the interaction energy E_{int} can be large compared to the kinetic energy E_{kin} . Neglecting the kinetic energy, having a large number of atoms N and treating the case for a repulsive interaction ($a > 0$), we can derive simple equations for a Bose-Einstein condensate. This approach is called the Thomas-Fermi approximation.

Neglecting the kinetic energy, we get from equation 1.31 the atom density $n(r)$

$$n(r) = \phi^2(r) = \frac{1}{g}(\mu - V_{ext}(r)) , \quad (1.34)$$

in the region $\mu > V_{ext}(r)$ and $n = 0$ for the rest. Equation 1.34 is an inverted parabola and it describes the spatial density distribution of a Bose-Einstein condensate. Equation 1.34 connects the chemical potential with the atom number, and by integration we get

$$\mu = \frac{\hbar\omega_{ho}}{2} \left(\frac{15Na}{a_{ho}} \right)^{2/5}. \quad (1.35)$$

Equation 1.34 maximizes in the center to $n_{TF}(0) = \mu/g$, and it vanishes for $\mu = V_{ext}(R)$. For a spherical harmonic trap, this means that the chemical potential is $\mu = m\omega_{ho}^2 R^2/2$. If we insert equation 1.35 we find for the condensate radius R

$$R = a_{ho} \left(\frac{15Na}{a_{ho}} \right)^{1/5}, \quad (1.36)$$

which can be significantly larger than a_{ho} (note here that this is with respect to the noninteracting case (equation 1.5) a significant change). Equation 1.36 is often noted as the Thomas Fermi radius. For the traps used in the experiment (cigar shaped traps) we get different radii

$$R_{\perp} = \sqrt{\frac{2\mu}{m\omega_{\perp}^2}}, \quad R_x = \sqrt{\frac{2\mu}{m\omega_x}}. \quad (1.37)$$

Comparing the densities $n_{ho}(0)$ for the ideal, non interacting case and the interaction case, and comparing the relevant widths we find

$$\frac{n_{TF}}{n_{ho}} = \frac{15^{2/5}\pi^{1/2}}{8} \left(\frac{Na}{a_{ho}} \right)^{-3/5}, \quad \frac{R}{a_{ho}} = \left(\frac{15Na}{a_{ho}} \right)^{1/5}. \quad (1.38)$$

We see, that due to the repulsive interaction ($a > 0$), the density at the center of the trap decreases with N (is flattened out), while the size of the Bose-Einstein condensate increases with N (it is bigger than in the non interaction case).

As it will turn out, when we treat collective shape oscillations of the Bose-Einstein condensate (see section 1.5.2), the Thomas-Fermi approximation is especially in the regime, where the kinetic energy can not be neglected, not always valid.

1.5 Basic properties of a BEC

A Bose-Einstein condensate, as it is a macroscopic quantum state, shows unique behavior. In this chapter we will discuss how it behaves when we release it from a trap and let it freely expand. From this expansion we will deduce the trap frequencies, based on simple scaling factors. Based on these scaling factors, we can characterize the dynamics of a Bose-Einstein condensate in time varying potentials. Here we will see, that collective shape oscillations are most likely to occur. This is of importance, because time varying potentials play an important role when manipulating a Bose-Einstein condensate.

1.5.1 Free expansion of a Bose-Einstein condensate

In this section we will discuss the free expansion characteristics of a Bose-Einstein condensate at rest. First the Bose-Einstein condensate is confined in a trap, then we open the trap instantaneously and the Bose-Einstein condensate can freely expand. To describe this, we use a time dependent potential, which is anisotropic but harmonic:

$$U(\vec{r}, t) = \frac{1}{2} \sum_{j=1,2,3} m\omega_j^2(t)r_j^2, \quad (1.39)$$

where m is the mass and ω is the trap frequency. The equation, which governs the time evolution is the time dependent Gross-Pitaevskii [39](see equation 1.30) and the solution to it in the Thomas-Fermi approximation is (see equation 1.34),

$$\Phi_{TF}(\vec{r}) = \left(\frac{\mu - U(\vec{r}, 0)}{Ng} \right)^{1/2}, \quad \mu \simeq g|\Phi(\vec{0})|^2. \quad (1.40)$$

In the discussed case of time varying potentials, the Thomas Fermi approximation (neglecting the kinetic term of equation 1.30) can not be applied, because potential energy could be converted to kinetic energy.

We will now discuss a semi-classical model, which motivates an ansatz we will present later in this section (see equation 1.47).

The solution of equation 1.30 is in general very difficult, but in this case (with some restrictions) it is possible [40]. Consider first a classical gas,

where each particle experiences the force

$$\vec{F}(\vec{r}, t) = -\nabla(U(\vec{r}, t) + g\varrho_{CL}(\vec{r}, t)), \quad (1.41)$$

where $\varrho_{CL}(\vec{r}, t)$ is the spatial density distribution at equilibrium.

Releasing the atoms from the trap ($t > 0$), the classical gas will experience a stretching, and the particles will follow the trajectories

$$R_j(t) = \lambda_j(t)R_j(0) \quad , \quad j = 1, 2, 3, \quad (1.42)$$

where $R_j(0)$ is the initial size at $t = 0$ (see equation 1.36) and $\lambda_j(t)$ is a scaling factor. Applying Newton's law $m\ddot{R}(t) = F_j[R(\vec{R}(t), t)]$, using the ansatz 1.42, we get

$$\begin{aligned} m\ddot{\lambda}_j(t)R_j(t) &= -\partial_{r_j}U[\vec{R}(t), t] + \frac{1}{\lambda_j\lambda_1\lambda_2\lambda_3}\partial_{r_j}U[\vec{R}(0), 0] \\ j &= 1, 2, 3 \end{aligned} \quad (1.43)$$

The second part of equation 1.43 is obtained, expressing $\varrho_{CL}(\vec{r}, t)$ as

$$\varrho_{CL}(\vec{r}, t) = \frac{1}{\lambda_1(t)\lambda_2(t)\lambda_3(t)} \varrho_{CL}[\{r_j/\lambda_j\}_{j=1,2,3}, 0], \quad (1.44)$$

and using the equilibrium condition $\nabla g\varrho_{CL}(t = 0) = -\nabla U(t = 0)$. The scaling factors satisfy the equation

$$\ddot{\lambda}_j = \frac{\omega_j^2(0)}{\lambda_j\lambda_1\lambda_2\lambda_3} - \omega_j^2(t)\lambda_j \quad , \quad j = 1, 2, 3, \quad (1.45)$$

with the initial conditions $\lambda_j(0) = 1$ and $\dot{\lambda}_j(0) = 0$. Deriving equation 1.42, we get an expression for the velocity (in each direction j) of the expanding sample

$$v_j(\vec{r}, t) = r_j \frac{\dot{\lambda}_j(t)}{\lambda_j(t)}. \quad (1.46)$$

Note here, that the velocity is position dependent. The presented classical description does not depend on the interaction strength g (especially equation 1.45) at all. The spatial density is the only quantity which contains the interaction strength.

We can now construct an ansatz for equation 1.30, based on this classical model, of the form [40]

$$\begin{aligned} \Phi(\vec{r}, t) &= e^{-i\beta(t)} \exp \left(m \sum_j i r_j / 2\hbar \cdot r_j \dot{\lambda}(t) / \lambda(t) \right) \\ &\cdot \frac{\tilde{\Phi}[\{r_k / \lambda_k(t)\}_{k=1,2,3}, t]}{\sqrt{\lambda_1 \lambda_2 \lambda_3}}. \end{aligned} \quad (1.47)$$

Ansatz 1.47 is a unitary transformation, which combines a scaling in \vec{r} (last part of the equation) and a gauge transformation (first part). This part of the ansatz contains a position dependent velocity (of the form $\exp(ik(r)r)$). Inserting 1.47 into equation 1.30, we get

$$\begin{aligned} \left[i\hbar \partial_t + \frac{\hbar^2}{2m} \sum_j \frac{1}{\lambda_j^2(t)} \partial_{r_j}^2 \right] \tilde{\Phi}(\vec{r}, t) = \\ \frac{1}{\lambda_1(t)\lambda_2(t)\lambda_3(t)} [-\mu + U(\vec{r}, 0) + Ng|\tilde{\Phi}(\vec{r}, t)|^2] \tilde{\Phi}(\vec{r}, t), \end{aligned} \quad (1.48)$$

where we use $\hbar \dot{\beta}(t) = \mu / \lambda_1(t)\lambda_2(t)\lambda_3(t)$ and the initial condition $\tilde{\Phi}(\vec{r}, 0) = \Phi(\vec{r}, 0)$. We can now check how equation 1.48 behaves, when we are in the regime, where the Thomas-Fermi approximation can be applied. The right hand side will be initially very small, the left hand side, containing the kinetic energy terms, will also be initially very small, and can be expected to stay small (the additional kinetic energy, caused by the change of the potential, was accounted for in the unitary transformation 1.47). $\tilde{\Phi}(\vec{r}, t)$ will therefore not change much in time. This important point becomes clearer, when we write $\tilde{\Phi}(\vec{r}, t) = \Phi(\vec{r}, 0) + \delta\tilde{\Phi}(\vec{r}, t)$, and insert this into equation 1.48 and 1.31. From this we get, that $\delta\Phi(\vec{r}, t)$ is governed by a nonlinear inhomogeneous equation, with the source term

$$S(\vec{r}, t) = -\frac{\hbar^2}{2m} \sum_{j=1}^3 \left(\frac{1}{\lambda_j^2(t)} - \frac{1}{\lambda_1(t)\lambda_2(t)\lambda_3(t)} \right) \partial_{r_j}^2 \Phi(\vec{r}, t). \quad (1.49)$$

For the Thomas-Fermi approximation, the spatial derivatives of $\Phi(\vec{r}, t)$ can be neglected, and subsequently the source term can be neglected. In this case, $\delta\tilde{\Phi}(\vec{r}, t)$, which is initially zero, stays zero and $\Phi(\vec{r}, t)$ stays constant. From these considerations follows, that we can write

$$\tilde{\Phi}(\vec{r}, t) \simeq \Phi(\vec{r}, 0) \quad (1.50)$$

which simply means, that the derived scaling factors in equation 1.45, which lead to the resulting equation 1.50, contain the complete dynamics of the macroscopic wave function of the Bose-Einstein condensate.

With this conclusion we obtained a powerful tool, as we can now derive the trap frequencies from the expansion of a Bose-Einstein condensate.

In a first step, we consider a sudden switch off of the confining potential. From equation 1.45 we then get the simple expressions

$$\frac{d^2}{d\tau^2}\lambda_{\perp} = \frac{1}{\lambda_{\perp}^3 \lambda_x}, \quad (1.51)$$

$$\frac{d^2}{d\tau^2}\lambda_x = \frac{\epsilon}{\lambda_{\perp}^2 \lambda_x^2}, \quad (1.52)$$

where λ_{\perp} stands for the radial direction, λ_x is the longitudinal direction, $\tau = \omega_{\perp} t$ is a dimensionless variable and $\epsilon = \omega_x(0)/\omega_{\perp}(0) \ll 1$. Equation 1.52 can be solved analytically, and $\lambda_x = 1$ to the lowest order in ϵ , so that we get

$$\lambda_{\perp}(\tau) = \sqrt{1 + \tau^2}, \quad (1.53)$$

and to second order in ϵ we get

$$\lambda_x(\tau) = 1 + \epsilon^2[\tau \arctan(\tau) - \ln \sqrt{1 + \tau^2}] + O(\epsilon^4). \quad (1.54)$$

Equation 1.53 and 1.54 show how the spatial width will change, when a Bose-Einstein condensate is freely expanding (under the condition of a sudden switch off). When we now insert these scaling factors into

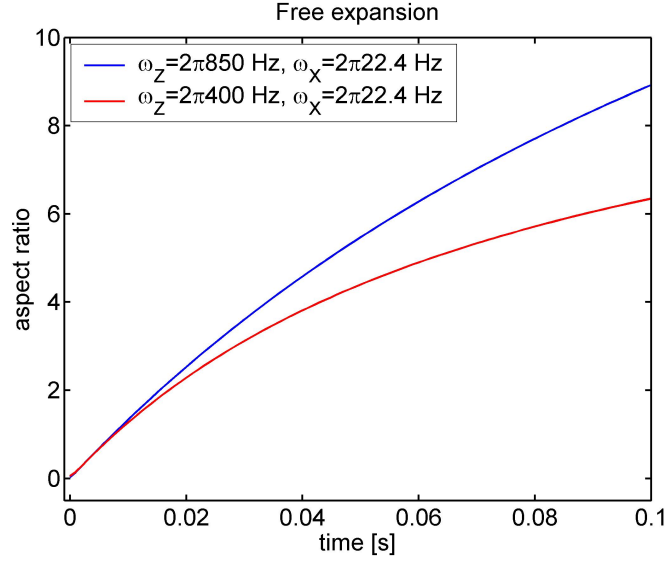


Figure 1.2: Free expansion of a Bose-Einstein condensate: the blue curve shows how the aspect ratio (see equation 1.55) evolves in time. The trap frequencies for the blue curve are: $\omega_{\perp} = 2\pi 850 \text{ Hz}$ for the radial and $\omega_x = 2\pi 22.4 \text{ Hz}$ for the axial direction, and for the red curve: $\omega_{\perp} = 2\pi 400 \text{ Hz}$ and $\omega_x = 2\pi 22.4 \text{ Hz}$.

equation 1.40, we can derive for the axial W_{\perp} and radial W_x widths of the density distribution the equation

$$\frac{W_x}{W_{\perp}} = \frac{\lambda_x(t)}{\lambda_{\perp}(t)} \frac{1}{\epsilon}. \quad (1.55)$$

Figure 1.2 shows equation 1.55 for a trap frequencies $\omega_{\perp} = 2\pi 850 \text{ Hz}$ and $\omega_x = 2\pi 22.4 \text{ Hz}$.

1.5.2 Exciting oscillations

The model discussed in 1.5.1 can be applied to more complex situations in such a sense, that we can study the transfer from a starting trap to a final trap, meaning that the trap frequencies of the confining traps change over time. The evolution of the shape of the Bose-Einstein condensate in the trap will be determined by the same scaling factors 1.45, and the Bose-Einstein condensate will carry out a collective shape oscillation in the final trap, according to these scaling factors. The energy needed for the oscillation comes from the potential energy of the starting trap, which is converted into

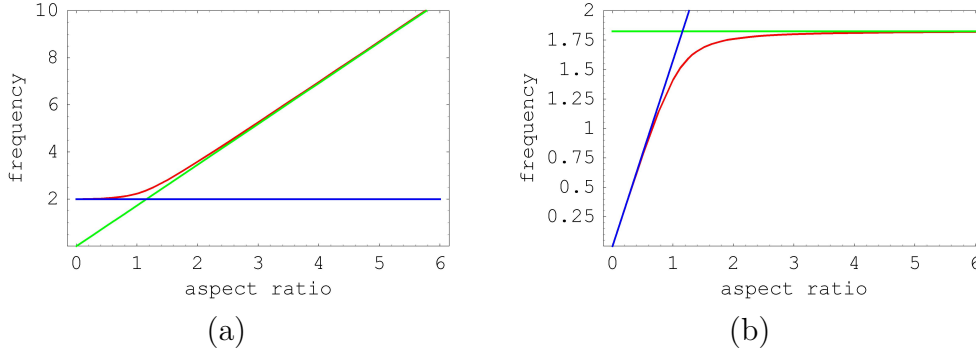


Figure 1.3: Trap frequency aspect ratio against shape oscillation frequency: red curves represent the two solutions of equation 1.57 (slow and fast frequencies), blue and green curves are asymptotic limits for big and small ϵ .

kinetic energy. When we switch off the trap, the dynamics on the trap become visible and are magnified by the expansion.

First, let us consider the in trap dynamics. For a small change in the size/shape of the Bose-Einstein condensate, we can linearize equation 1.45, and we obtain

$$\begin{aligned} \frac{d^2}{d\tau^2} \delta\lambda_{\perp}(\tau) &= -4\delta\lambda_{\perp}(\tau) - \delta\lambda_x(\tau), \\ \frac{d^2}{d\tau^2} \delta\lambda_x(\tau) &= -2\epsilon^2 \delta\lambda_{\perp}(\tau) - 3\epsilon^2 \delta\lambda_x(\tau), \end{aligned} \quad (1.56)$$

where $\delta\lambda_{\perp}$ and $\delta\lambda_x$ are the change of width from the equilibrium. Calculating the eigenmodes of the system 1.56 leads to [41]

$$\omega_{osc}^2 = 2 + \frac{3}{2}\epsilon^2 \mp \frac{1}{2}\sqrt{9\epsilon^4 - 16\epsilon^2 + 16} \quad (1.57)$$

where ω_{osc} is the oscillation frequency of the widths in units of ω_{\perp} . It is now interesting to look at the behavior of equation 1.57 for different regimes of ϵ . Figure 1.3 a) and b) shows the aspect ratio ϵ against the shape oscillation frequency.

For the regime of $\epsilon \ll 1$ (a cigar shaped type trap), we obtain for the slow $\omega_{osc}^{slow} = \sqrt{5/2}\omega_x$ and for the fast oscillation frequency $\omega_{osc}^{fast} = 2\omega_{\perp}$. For the limit of $\epsilon \gg 1$ (a disc type trap), we obtain $\omega_{osc}^{slow} = \sqrt{10/3}\omega_{\perp}$ and

$\omega_{osc}^{fast} = \sqrt{3}\omega_x$ for the longitudinal and radial shape oscillation frequency. In our experiment we have a cigar shaped trap, and we are deep in the regime of $\epsilon \ll 1$ ($\epsilon = 0.027$). Note here, that the derived equation 1.57 and its solutions are only valid for small perturbations.

For large perturbations the non linear character of equation 1.45 becomes important. Equation 1.45, which describes the evolution dynamics of the Bose-Einstein condensate, describes three classical harmonic oscillators, which are coupled via a non linear term $\sim \omega_j^2(t)/\lambda_j\lambda_1\lambda_2\lambda_3$. This term establishes the coupling between the different shape oscillation modes, and when we want to treat large perturbations it is this equation, which we have to solve [42, 43].

To study the effect of the oscillations in the trap, we expand the Bose-Einstein condensate at different times, the hold time. Here the dynamics of the oscillations in the trap dominate the expansion behavior, depending on the hold time. To illustrate the shape oscillations, we numerically solve equation 1.45. This is done with a MATLAB program², where a frequency change from an initial frequency to an end frequency is implemented. The change between the frequencies is done with a frequency ramp, corresponding to the experimental situation (see chapter 5.1). The trap is kept at the final frequencies for the adjustable hold time. After the trap is switched off, we calculate the behavior i.e its aspect ratio.

In figure 1.4a) the trap is still closed and we plot the widths in radial and longitudinal direction. The shape oscillations for the radial and longitudinal directions are out of phase. This can be understood with a simple pressure argument. The term $1/\lambda_1\lambda_2\lambda_3$ (see equations 1.43 and 1.57), representing a volume, changes when the sample changes its size. If it expands in one direction, the pressure is reduced in the other direction, and the size in the latter direction will be reduced. Figure 1.4b) shows the expansion behavior, which is different from the behavior we get from the steady state (sudden switch off of the trap).

The expansion behavior for a series of hold times is plotted in figure 1.5a). Note here, that the dynamics in the trap are magnified in the expansion behavior. If we open the trap at a turning point of the shape oscillation (see figure 1.4a)), we will get a different expansion behavior compared to another hold time. For a specific expansion time, and for a variable hold time we will observe a oscillating aspect ratio. Figure 1.5b) shows the aspect ratio oscillation after an expansion time of 19 ms. The period is as predicted. The peaks of the aspect ratio are pronounced, while the valleys are smoothed out.

Experimentally the (slow) oscillation frequency can be easily measured,

²the code was written by M. Andersson

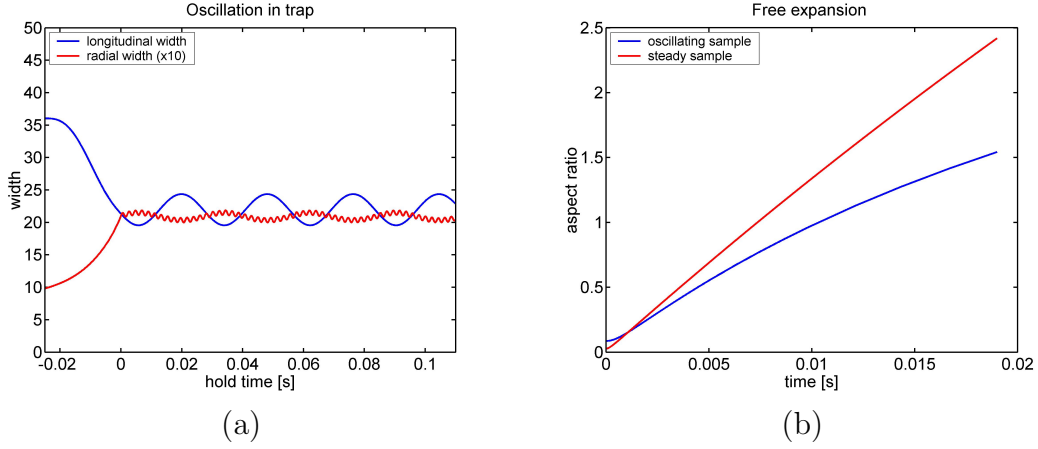


Figure 1.4: Oscillating Bose-Einstein condensate: the conditions are: starting trap, with trap frequencies of $\omega_{\perp} = 2\pi 827.1 \text{ Hz}$ and $\omega_x = 2\pi 22.5 \text{ Hz}$, then the frequencies are changed in 25 ms to $\omega_{\perp} = 2\pi 234.7 \text{ Hz}$ and $\omega_x = 2\pi 22.4 \text{ Hz}$. a) At $t = 0$ the frequency ramp from the initial frequencies to the final frequencies is accomplished. Then, for $t > 0$, the shape oscillations in the longitudinal and radial direction are plotted (the Bose-Einstein condensate is still in the trap). At $t = 0.09 \text{ s}$ the trap is switched off and the sample expands. The expansion characteristic, shown in b), differs (blue curve) from the expansion we expect when we switch off the trap instantaneous (red curve represents equation 1.55).

using the procedure described above. For a given expansion time we monitor the oscillating aspect ratio (see figure 1.5). The fast oscillation frequency is experimentally not easy to detect, due to the Nyquist-Shannon theorem [44, 45] (sampling rate must at least be greater than $2 \times$ oscillation frequency, and for our traps ω_{\perp} is in the kHz range). The small amplitude of the fast oscillation puts another restriction to the measurement.

It is now interesting to look at longer expansion times. Here the inner dynamics are more magnified. Figure 1.6 was generated exactly the same way as it was done for figure 1.5, but now we let the Bose-Einstein condensate expand for 400 ms. We see, that the moderate behavior, which we observed for short expansion times, is now completely different. Note here, that the model assumes still the Thomas Fermi limit (neglecting the kinetic energy part). At huge aspect ratio changes (the Bose-Einstein condensate is strongly compressed in one direction), an applicable model must take this kinetic energy term into account.

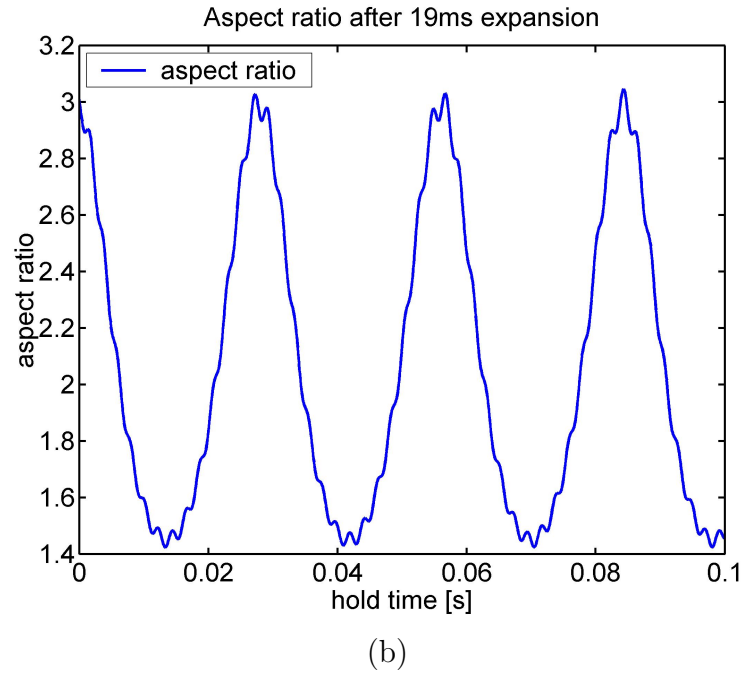
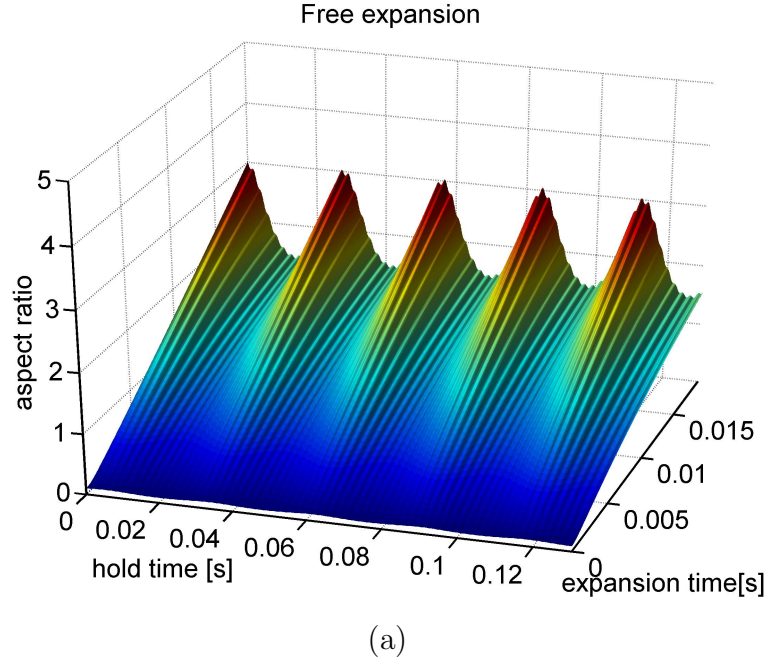


Figure 1.5: Collective shape oscillation of a Bose-Einstein condensate and free expansion: a) we excite collective shape oscillations as described in the caption to figure 1.4, but now we calculate the expansion behavior every ms for an expansion time of up to 19 ms. b) shows the aspect ratio after 19 ms of expansion. The valleys correspond to a low aspect ratio (more round shaped Bose-Einstein condensate, see figure 5.3), the peaks represent a high aspect ratio (axially more elongated Bose-Einstein condensate). The period is as predicted, but the peaks are more pronounced due to the non linear coupling of the different modes.

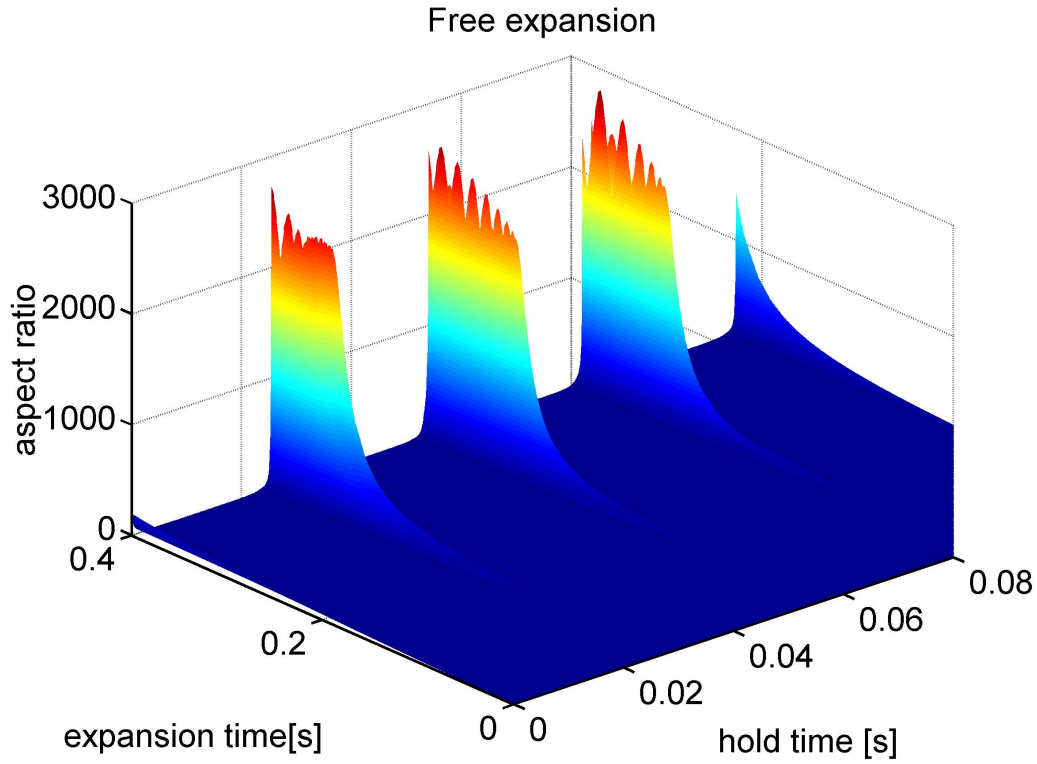


Figure 1.6: Expansion behavior of a oscillating Bose-Einstein condensate for long expansion times: the sample is expanded for 400 *ms* and the aspect ratio for different hold times (every ms) is plotted. Aspect ratios of up to ~ 2500 can be observed. This behavior is due to the non linear nature of the coupling between the modes.

Chapter 2

Laser cooling

Laser cooling is based on the fact that a photon carries momentum [46, 47], and that this momentum can be transferred to the atom via absorption of the photon. As a result the atom will change its momentum, and as a consequence can be cooled [48, 49]. This basic idea made it possible to trap and cool atoms down to temperatures not reachable with conventional techniques.

In this chapter we discuss the basics steps, which are involved to cool atoms with laser light. We start from Doppler cooling and the concept of atom - light interaction. Then we introduce the more complex polarization gradient cooling, which allows us to overcome the limits of Doppler cooling. We will see that these two concepts allow us to reach reasonable low temperatures. Both mechanisms work only in momentum space. To trap and cool the atoms in position space, we employ a magneto-optical trap (MOT)¹.

2.1 Doppler cooling

Doppler cooling relies on the fact, that when an atom absorbs or emits a photon, its momentum is changed [50, 51].

In general the direction of the emitted photons are randomly distributed over 4π . If we shine a laser beam from one direction onto the atom, the atom will change its momentum in *average* by $\Delta\vec{p} = \hbar\vec{k}$ in the direction of the laser beam.

Considering the one dimensional case, a two level atom, with a resonant absorption frequency ω_A , mass m and a velocity v . We shine a laser beam, with a frequency ω_L and a wavevector $k_L = \omega_L/c$ (c is the speed of light), onto this atom. Calculating the velocity change of the atom, and the

¹One can find a good treatment of the coming section in ??.

frequency difference of the re-emitted photon after a resonant absorption gives us

$$v_R = \frac{\hbar k}{m} \quad , \quad \Delta\omega = kv + \frac{\hbar k^2}{2m} \quad , \quad (2.1)$$

where v_R is the recoil velocity (the velocity change an atom experience when it absorbs a single photon) and kv is the Doppler shift ($kv = \omega_L v/c$). The second term in the second equation of 2.1 is the so called recoil shift, and is equal to the kinetic energy in frequency units.

In general we can write $\delta = \omega_A - \omega_L$ where δ is the so called detuning of the laser (it will play an important role for laser cooling). Exciting an atom resonantly, we have to take the Doppler shift $\delta_{Dopp} = kv$ into account. This leads us to an effective detuning of $\delta_{eff} = \delta - kv$. An atom, irradiated with light with this detuning, will experience an *average* force F

$$F = \hbar k \frac{\Gamma}{2} \frac{I/I_0}{1 + I/I_0 + [\frac{2(\delta - kv)}{\Gamma}]^2} \quad , \quad (2.2)$$

where I is the intensity of the laser, I_0 is the saturation intensity. Equation 2.2 is simply the product of the photon momentum $\hbar k$ times the scattering rate. The scattering rate is the rate, at which the atom can absorb and re-emit spontaneously a photon. The force saturates for large intensities and a laser detuning of $\delta = kv$ to $F = \hbar k \Gamma / 2$. It is clear from equation 2.2, that it depends on Γ , the linewidth of the atomic transition.

Expanding the example to two counter propagating laser beams ($I/I_0 \ll 1$) we get for the total force on the atoms (still in one dimension):

$$F(v) = \hbar k \frac{\Gamma}{2} \frac{I/I_0}{1 + I/I_0 + [\frac{2(\delta - kv)}{\Gamma}]^2} - \hbar k \frac{\Gamma}{2} \frac{I/I_0}{1 + I/I_0 + [\frac{2(\delta + kv)}{\Gamma}]^2} \quad . \quad (2.3)$$

Figure 2.1 illustrates this force. For small velocities v and I/I_0 we can derive an expression:

$$F(v) = 2\hbar k^2 \frac{(2I/I_0)(2\delta/\Gamma)v}{[1 + (\frac{2\delta}{\Gamma})^2]^2} \quad . \quad (2.4)$$

Equation 2.4 is in a form where the velocity dependence of the force is more

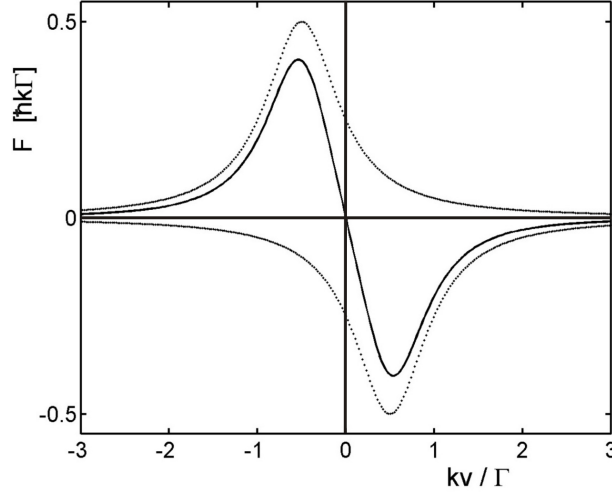


Figure 2.1: Force on an atom: the dotted lines indicate the force of a single laser beam from the left/right (equation 2.2). The solid lines corresponds to the sum of the two forces (equation 2.3).

explicit. The force can be associated with a friction force as it is proportional to the velocity v , and it can be simplified to $F = -\alpha v$. This beam configuration is known as "optical Molasses".

An important question to ask is the lowest temperature reachable with this method. Up to now we looked at the time *average*, but every absorption/emission transfers a discrete amount of momentum, leading to a fluctuating force. This tends to heat the atoms, because the emission direction is uncorrelated to the absorption. This randomness of the direction causes the atom to undergo a random walk, with a step size of $\hbar k$. From a random walk treatment we get for the mean square momentum after N emissions $\langle p_x^2 \rangle = N \hbar^2 k^2$. The rate of increase of p^2 , the momentum diffusion coefficient, is defined as

$$2D_{spont} = \langle \dot{p} \rangle = 2\hbar^2 k^2 \frac{\Gamma}{2} \frac{I/I_0}{1 + (2\delta/\Gamma)^2} \quad . \quad (2.5)$$

To the limit of how deep we can cool, we equate the rate on which the kinetic energy increases with the rate on which the kinetic energy decreases due to the damping. This gives us

$$\langle \dot{E}_{heat} \rangle = \frac{\langle \dot{p}^2 \rangle}{2m} = \frac{D}{m} - \langle \dot{E}_{cool} \rangle = \alpha \langle v^2 \rangle \quad , \quad (2.6)$$

and

$$k_B T = \frac{D}{\alpha} = \frac{\hbar\Gamma}{4} \left(\frac{\Gamma}{2\delta} + \frac{2\delta}{\Gamma} \right). \quad (2.7)$$

The temperature minimizes for $\delta = -\Gamma/2$, and leads us to

$$k_B T_{Dopp} = \frac{\hbar\Gamma}{2}. \quad (2.8)$$

T_{Dopp} is the so called Doppler cooling limit. It depends just on Γ , the natural linewidth of the atomic transition. In the case of ^{87}Rb , the linewidth is $\Gamma = 2\pi 6.065$ MHz, which gives us a Doppler cooling limit of $T_{Dopp} = 145.5 \mu\text{K}$. To cool below the Doppler limit, one has to employ a different technique (see section 2.3).

Note here that the atoms are slowed down in *momentum space*, and the cold atoms are not localized at a specific location in real space.

2.2 Magneto-optical trap

In section 2.1 we saw, that slowing down the atoms in momentum space is possible. It is also possible to show, due to the optical Earnshaw theorem, that it is not possible to form a trap which is just based on absorption and emission [52, 50].

For trapping atoms in real space we must generate a position dependent force which confines the atoms at a localized position in space. This can be done by adding a magnetic field to the atoms. The field is generated by a pair of coils, where the current runs in opposite directions. The resulting field is a quadrupole field, where the magnitude is proportional to the distance from the center and the direction reverses at the trap center. Due to the magnetic field, the magnetic sub-levels m_F experience a Zeeman shift, and thus the atoms are detuned from the resonance. The used laser beams are circular polarized, where opposing beams have counter-rotating polarizations. Thus the atoms scatter more photons from that laser beam, which is counter propagating to their direction of motion, and thus they are pushed to the center of the configuration [4, 53, 54]. Figure 2.2 shows the laser beam setup and the Zeeman splitting. This configuration is called magneto-optical trap

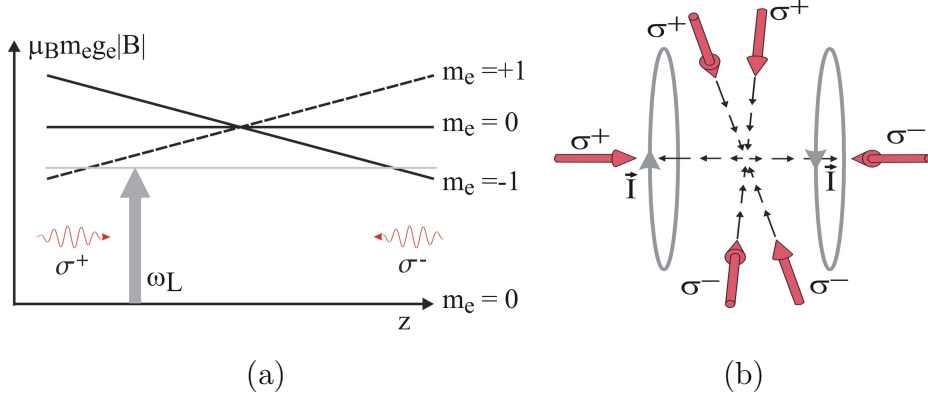


Figure 2.2: Magneto optical trap: a) shows the energy splitting due to the Zeeman effect and the corresponding polarizations. b) gives an schematic overview how the coils for the quadrupole field look like and how the polarizations should be.

(MOT) or Zeeman assisted radiation pressure trap (ZARPT). The force depends now not only on the laser detuning δ and the atom velocity v , but also on the value of the magnetic field at a certain position. This gives us

$$\begin{aligned}
 F = F_{\sigma^+} + F_{\sigma^-} &= \frac{\hbar k \Gamma}{2} \left[\frac{I/I_0}{1 + 4 \left(\frac{\delta - kv + \mu |B(r)|/\hbar}{\Gamma} \right)^2} - \frac{I/I_0}{1 + 4 \left(\frac{\delta + kv - \mu |B(r)|/\hbar}{\Gamma} \right)^2} \right], \\
 \mu &= \mu_B (g_e m_e - g_g m_g)
 \end{aligned} \tag{2.9}$$

where m_e and m_g are the magnetic quantum numbers of the ground state (g) and excited state (e), and g_e , g_g are the corresponding Landé factors.

2.3 Polarization gradient cooling

We saw in section 2.1, that the temperature is just determined by the atomic property. However with this method we can reach reasonable temperatures. To get lower temperatures we have to employ a different mechanism, the polarization gradient cooling [55].

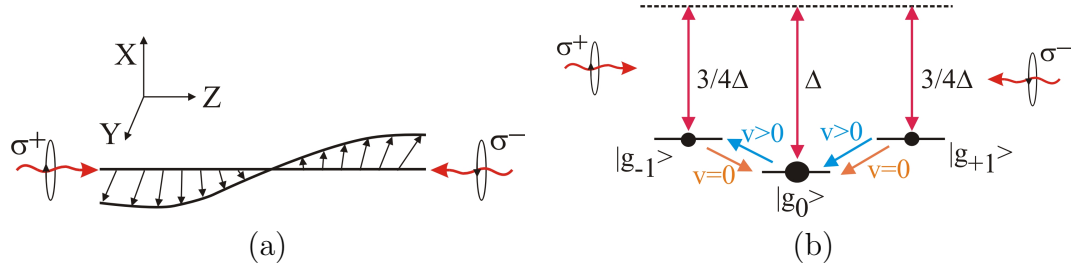


Figure 2.3: Polarization gradient cooling: a) we have two counter propagating laser beams, which circular polarizations are counterrotating, we get a linear polarization, which forms a helix with a period of $\lambda/2$ (λ is the wavelength). Such a polarization arrangement is identical to the arrangement we get for a magneto-optical trap (see figure 2.2b)). b) shows the situation of the shifted light levels. Due to the different Clebsh-Gordan coefficients, the $|g_0\rangle$ ground state is more shifted and higher populated.

As an example, we analyze two circular polarized, counter propagating laser beams. The polarizations are opposite circular polarized². With such a configuration (see figure 2.3a)), we created a polarization, which is linear (π polarized) and forms a helix with a period of $\lambda/2$ (λ is the wavelength). The laser intensity is always the same. The energy levels of a multi level atom in this laser field will experience an energy shift Δ , the so called light shift [51, 56] (also noted as the AC-Stark shift),

$$\Delta \propto \frac{\Omega^2}{\delta} \quad , \quad \Omega^2 = \frac{\Gamma^2}{2} \frac{I}{I_0} \quad , \quad (2.10)$$

where δ is the laser detuning and Ω is the Rabi frequency. The populations in the ground level will depend on the Clebsh-Gordan coefficients. For a transition $J = 1 \rightarrow J = 2$ we have the following situation: as a π transition from the ground state $|g_0\rangle$ to the excited levels is $4/3$ stronger than a transition from $|g_{\pm 1}\rangle$ to the excited levels, the light shifts are smaller for the $|g_{\pm 1}\rangle$ ground states (the $|g_0\rangle$ state couples stronger to the light field). Furthermore the transitions $|g_{\pm 1}\rangle \rightarrow |g_0\rangle$ is stronger than the transition $|g_0\rangle \rightarrow |g_{\pm 1}\rangle$, which means, that we will accumulate a larger population in $|g_0\rangle$ (see figure 2.3b)). Note here, that for the above considerations the atom was at rest. When an atom moves in Z direction with a velocity $v > 0$, it will see a linear polarization, which rotates around the beam axis (the Z axis, and it

²we choose this, because such a configuration we get for 'free' (see section 2.2)

rotates in the X/Y plane). We can introduce in the atomic rest frame a rotating frame, where the linear polarization points always in the same direction. In this moving rotating frame, a fictitious field will appear (Larmor's theorem), which looks like a magnetic field parallel to the Z axis. If we analyze the new situation, and compare it to the steady state, which we discussed above, we find, that we get a motion induced spin orientation in the atomic ground state, which means that we do not find the steady state population but we find more atoms in the $|g_{-1}\rangle$ state than in the $|g_{+1}\rangle$ state (for $v > 0$ and $\delta < 0$). This unbalance in population will result in an unbalance of the radiation pressure of the σ^+ and σ^- light, thus the atom will absorb more counterpropagating σ^- photons than copropagating σ^+ photons. Due to the unbalanced absorption the atom is slowed down, and as a result the motion induced orientation of the atoms is reduced (and therefore the unbalanced population), and thus the damping gets smaller with reduced velocity.

The resulting force can be expressed as

$$\langle F \rangle \propto \hbar k^2 \frac{-\delta \Gamma}{5\Gamma^2 + 4\delta^2} v. \quad (2.11)$$

Here again a minimum temperature can be reached. Following the arguments in section 2.1, we obtain

$$k_B T = \frac{\hbar \Omega^2}{|\delta|} \left[\frac{29}{300} + \frac{254}{75} \frac{\Gamma^2/4}{\delta^2 + (\Gamma^2/4)} \right] \quad (2.12)$$

As we see, the temperature now depends on the laser detuning δ and on the Rabi frequency $\Omega = \Gamma \sqrt{I/2I_0}$, and therefore on the intensity of the laser. Both parameters can be experimentally tuned, which means, that with this method we are able to cool further than the Doppler cooling limit. This cooling technique works good for small velocities, meaning that the $\Gamma' \ll \Gamma$, where Γ' is the mean scattering rate.

For completeness it should be mentioned, that a configuration consisting of two linear polarized laser beams (the polarizations are perpendicular to each other) can also be used.

For the polarization gradient cooling exists also a limit, which is the so called recoil limit (thats the energy a single photon can transfer to the atom).

Chapter 3

Magnetic trapping

To cool neutral atoms down to ultra low temperatures ($\sim \mu K$ regime) we have to employ a different technique, than the one presented in chapter 2, which does not rely on the interaction with light. We found, that this limits us to the recoil energy. To overcome this, we can use the magnetic moment of an atom and a magnetic field [7]. This interaction gives rise to a potential, in which the atoms can be trapped. This alone will of course not cool the atoms, but it allows us to implement the evaporation technique (see section 3.3), which is capable to reach temperatures in the sub μK regime.

We start with a brief discussion on how atoms interact with inhomogeneous magnetic fields. This interaction gives rise to the possibility, to trap atoms in magnetic potentials at well defined locations in space. To generate this potentials, we use magnetic micro traps. They consist of simple wires and homogeneous magnetic bias fields. This arrangement, is in comparison to commonly used magnetic traps, extremely simple, and allows almost arbitrarily designed magnetic trapping potentials. We discuss 2 and 3 dimensional trapping geometries, as well as finite size effects, as the structures which generate the trapping potentials are of finite size (mm to μm range). In the end of this chapter we will consider the role of current noise and its affect on the atoms.

3.1 Atom - magnetic/electric field interaction

An atom, carrying a total spin \vec{F} and a magnetic moment $\vec{\mu}$, will experience a force in an inhomogeneous magnetic field \vec{B} of the form

$$\vec{\mathcal{F}} = \vec{\nabla} (\vec{\mu} \cdot \vec{B}) \quad , \quad \vec{\mu} = -g_F \mu_B \vec{F} \quad , \quad (3.1)$$

where g_F is the Landé factor, μ_B is the Bohr magneton, \vec{F} is the total spin of the atom, and thus $\vec{\mu}$ is the magnetic moment of the atom. The force $\vec{\mathcal{F}}$ is proportional to the gradient of the magnetic field component, with respect to the axis of the magnetic moment of the atom. The potential the atom experiences in such a magnetic field is

$$V_{mag} = -\vec{\mu} \cdot \vec{B} = g_F \mu_B m_F B. \quad (3.2)$$

Normally, the motion of an atom in a vector coupled potential is quite complicated (first part in equation 3.2). Assuming that the magnetic moment of the atom follows the direction of the magnetic field adiabatically, the motion of the atom becomes simplified. In other words, if the Larmor frequency $\omega_{Larmor} = \mu_B B / \hbar$ is faster than the change of the magnetic field, m_F becomes a constant of motion and we can neglect transitions between different m_F states. This can be written

$$\omega_{Larmor} = g_F \mu_B B / \hbar \quad , \quad \left| \frac{d}{dt} \frac{\vec{B}(r(t))}{|\vec{B}(r(t))|} \right| < \omega_{Larmor} \quad , \quad (3.3)$$

where $r(t)$ is the position of the atom. The second part of equation 3.3 will be noted as the adiabatic criterium. We will find this criterium in different notations many times throughout this work.

Two cases can be distinguished when we look at the orientation of μ with respect to a static magnetic field.

1) μ points in the *same* direction as the magnetic field: this results in $V_{mag} < 0$ meaning that the atom is attracted to high magnetic fields. This state is called *strong field seeking state*. It is the lowest energy state of the system and potential minima can be found at maxima of the magnetic field. However, the Earnshaw theorem [57, 58] prohibits magnetic field maxima in a source free space.

2) μ points in the *opposite* direction to the magnetic field: this results in $V_{mag} > 0$, meaning that the atoms are attracted to low magnetic fields and repelled by high ones. This state is called *low field seeking state*. Minima of the potential are found at minima of the modulus of the magnetic field. This

is not forbidden by the Earnshaw theorem, and therefore we can generate such minima easily in free space.

Up to now we just looked at the magnetic interaction. It is also possible that we use the interaction of an atom, with the electric polarizability α , with an electric field. Normally this interaction is complicated, as α is in general a tensor. For simple atoms with only one unpaired electron in the s-state, α can be replaced by a scalar, and the calculation becomes simpler. The potential is

$$V_{el}(r) = -\frac{1}{2}\alpha E^2(r), \quad (3.4)$$

where E is the applied electric field. The potential 3.4 is attractive, which means that the atoms can not be trapped with static electric fields, as the atoms will fall onto the charged structure (in the case of a charged wire they will fall onto the wire [59, 20, 22]). A possible way to trap atoms, but still using the electrical interaction, is the combination with the magnetic interaction [60] (a combination with an optical interaction is also possible [25]). This combination gives us a trapping potential of the form

$$V(r) = g_F \mu_B m_F B - \frac{1}{2}\alpha E^2(r), \quad (3.5)$$

where the first part of equation 3.5 is the known magnetic potential.

In this work the electric interaction can be neglected, because the electric fields caused by the voltage drop across a wire is too small.

3.2 Magnetic microtraps

In section 3.1 we saw, that in potential minima, neutral atoms can be trapped. There are various ways to generate a field geometry, which provides such minima [7, 10, 11]. Here we will discuss different trapping arrangements, where the trapping fields are generated by especially simple geometries, using the field of current carrying wires and homogeneous magnetic bias fields, generated by coils [61, 62, 22]. We will see that the scaling laws can be deduced from simple considerations. In addition, these wires and bias field geometries allow a complex modelling of the trapping potentials, which would be hard to realize with common approaches.

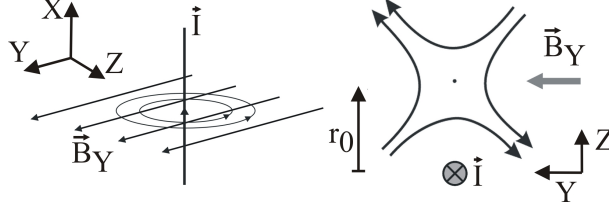


Figure 3.1: A wire with a current I and a homogeneous bias field B_Y : the bias field B_Y compensates the wire field at a point r_0 and creates a minimum above the wire.

3.2.1 A straight wire and a bias field

We start with the simplest trap, the field of a single current carrying wire superimposed by a homogeneous bias field. The modulus of the magnetic field of a straight, infinitely long and thin wire is

$$B(r) = \frac{\mu_0 I}{2\pi r} \quad (3.6)$$

where r is the distance from the wire, μ_0 is the permeability constant and I is the current through the wire. When we now add a homogeneous magnetic bias field B_Y , perpendicular to the wire, we see when we look at the vector nature of the magnetic field, that the bias field B_Y will compensate at a certain distance r_0 the magnetic field of the wire (see figure 3.1, here the coordinate system is also defined; we will use this throughout this work). At this point the magnetic field will be zero. When we move from this point towards the wire, the magnetic potential will rise. If we move away from r_0 the potential will increase to the value of the bias field. In figure 3.1 it becomes clear, that the potential looks like a quadrupole potential along the radial direction (around r_0) and the trap depth is determined by the bias field B_Y . Along the wire the potential is open. This configuration allows us to trap low field seeking atoms at the potential minimum. It forms a 2-dimensional 'tube' and will be referred to as side guide. Point r_0 can be simply calculated from equation 3.6, leading us to

$$B(r_0) = B_Y \quad , \quad r_0 = \frac{\mu_0 I}{2\pi B_Y} . \quad (3.7)$$

To further characterize the trap we calculate the gradient (around r_0). For

this we simply derive the gradient of equation 3.6 and substitute r with r_0 . This leads to

$$\frac{dB(r)}{dr} = -\frac{\mu_0}{2\pi} \frac{I}{r^2}, \quad (3.8)$$

$$\left. \frac{dB(r)}{dr} \right|_{r_0} = -\frac{2\pi}{\mu_0} \frac{B_Y^2}{I} = \frac{B_Y}{r_0} \quad (3.9)$$

At r_0 the magnetic field vanishes, and the adiabatic criterium 3.3 is not fulfilled. Atoms at this point can undergo Majorana spin flips, because the magnetic moment of the atoms can not follow the direction of the magnetic field, and spin flips into non trapped states are possible [63, 64]

To avoid Majorana spin flips, we can apply a magnetic field B_{IP} along the wire (X direction). This 'plugs' the magnetic hole and near the minimum, the potential change from a linear to a harmonic behavior. This kind of potential is often called Ioffe-Pritchard trap, and B_{IP} is the Ioffe-Pritchard offset field. The curvature of the potential with the additional bias field is

$$\frac{d^2B(r)}{dr^2} = \left(\frac{2\pi}{\mu_0} \right)^2 \frac{B_Y^4}{B_{IP} I^2} = \frac{B_Y^2}{r_0^2 B_{IP}}. \quad (3.10)$$

We can now approximate the resulting potential with a harmonic oscillator. This is applicable near the minimum of the trapping potential. Calculating the curvature of the harmonic potential gives us access to the trap frequencies

$$\frac{\omega}{2\pi} = \frac{1}{2\pi} \sqrt{\frac{\mu_B g_F m_F}{m} \left(\frac{d^2B}{dr^2} \right)} \propto \frac{B_Y}{r_0} \sqrt{\frac{1}{m B_{IP}}}, \quad (3.11)$$

where m is the mass of the particle. Equation 3.11 reveals the importance of B_{IP} for the trap frequencies. In the experimental section we will see that we directly manipulate B_{IP} , to achieve different trapping frequencies.

Equation 3.9 reveals an important fact, that a smaller current causes higher gradients. Equation 3.8 can be evaluated in the limit $r \rightarrow R$, where R is the wire radius. This leads us to

$$\frac{dB(r)}{dr} = -\frac{\mu_0}{2\pi} \frac{I}{R^2} \propto j, \quad (3.12)$$

where j is the current density in the wire. This and equation 3.8 indicates, that with smaller structures, tighter confinements are achievable [65].

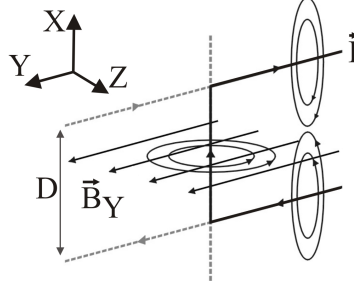


Figure 3.2: The U-wire trap: a single wire is bent into a U shape and a bias field B_Y is added. In such a way we can generate a three dimensional confinement. The potential is quadrupole like.

3.2.2 Creating three dimensional traps with wires

The presented potential in section 3.2.1, can trap atoms in two dimensions. To realize a three dimensional confinement, a different strategy is necessary. Normally wire traps, which are capable of this, consist out of a single bent wire, where some parts of the wire provide a field, which closes the trap in the third dimension. Here we will discuss two configurations for three dimensional trapping, the U-wire trap and the Z-wire trap. The names are self explanatory for the wire geometry.

U-wire trap

Bending a wire into a U shape, we get the base for the U-wire trap [23]. It consists of two so-called leads, and a central wire. The bias field B_Y is perpendicular to the central wire. Figure 3.2 illustrates this configuration. The central wire together with the B_Y field will form as discussed in section 3.2.1 a minimum along the central wire. This minimum (it's a zero!) is sealed off by the contribution of the leads. The field of the leads (counter propagating currents) will be less in the geometrical center of the construction (the field here points in Z direction), as it decays with $1/r$, compared with the share closer to the leads. B_Y is parallel to the leads and can therefore be neglected. The fact, that the field of the leads point in Z direction in the center of the geometry, causes a shift of the minimum in Y direction. This can be understood in such a way, that the fields are vectorial added. If we add a component in Z direction to the field displayed in figure 3.1, the minimum would move in Y direction. This shift can be compensated by simply adding an additional external field B_Z in the Z direction. We can now compute the resulting potential (wire+ B_Y + B_Z),

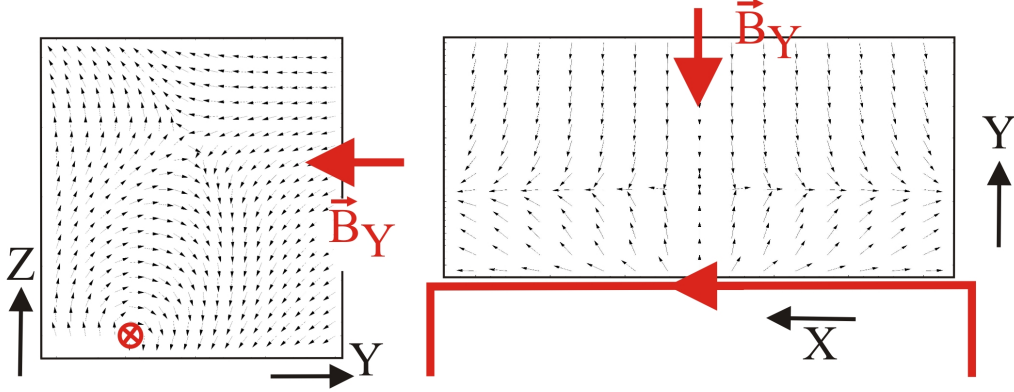


Figure 3.3: The U-wire trap: a cut through the Y/Z plane (left) reveal, that the minima is shifted outwards, and that the axis of the quadrupole field are tilted (compare with figure 3.1). In the X/Y plane (right), the quadrupole nature is clearly visible.

which gives us a sufficient complex result (see Appendix D), but still we can deduce the main properties of the geometry.

The main feature of the created potential is, that it is a quadrupole like field in three dimensions. Figure 3.3 illustrates this. Another important property for the experiment is the height z_0 of the minimum above the wire. The ratio of the two bias fields, B_Z and B_Y for $y_0 = 0$ is

$$\frac{B_Z}{B_Y} = \frac{2z_0}{\sqrt{D^2 + 4z_0^2}}, \quad (3.13)$$

where D is the distance between the leads. Another important property are the gradients achievable with a U-wire configuration [66]. They can be written as

$$\begin{aligned} \left. \frac{dB}{dy} \right|_{z_0} &= \frac{2\mu_0}{\pi} \frac{IDz_0}{(4z_0^2 + D^2)^2} \\ \left. \frac{dB}{dz} \right|_{z_0} &= \left. \frac{dB}{dx} \right|_{z_0} = -\frac{\mu_0}{2\pi} \frac{I}{z_0^2}. \end{aligned} \quad (3.14)$$

This is valid for $r = (0, 0, z_0)$. Here we have a difference to a quadrupole

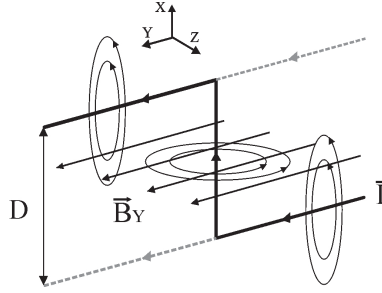


Figure 3.4: The Z-wire trap: a single wire is bent into a Z shape and a bias field B_Y is added. In such a way we can generate a three dimensional confinement. The potential is Ioffe-Pritchard trap with a non zero minimum.

configuration generated by coils (anti Helmholtz configuration). In this configuration the ratio between the strong and weak axis is always 2, but here it depends on the length D , the distance of the leads. The generated field, as it is a quadrupole field, and can be used to serve a MOT (see section 2.2). As can be seen in figure 3.3, the quadrupole axes are tilted with respect to the plane of the structure. This, one has to take into account when using such a field for a MOT, as it means that the laser beams have to be also tilted. Note here that the shift of the minimum with the help of B_Z does not change this behavior, but improves the properties of the quadrupole field as the region where it is in a good approximation a quadrupole field, is enlarged [67, 68].

Z-wire trap

To produce a magnetic trap in three dimensions with a no zero minimum, we have to employ different wire geometries. A geometry which fulfills this, is a wire bent into a Z shape [69]. We have again a center wire and two leads, but in contrast to the U wire, the current in the leads is co propagating (see figure 3.4). The wire carries a current I and the bias field B_Y is again perpendicular to the center wire. The magnetic field of the leads will now point in the same direction, which is the X direction, providing us with the necessary plug already discussed in section 3.2.1. With this geometry we designed a magnetic trap without zero minimum. It is a Ioffe-Pritchard trap. The field component at the minimum points essentially in the X direction. It can be expressed (for $X=0$, $Y=0$) as:

$$B_X = \frac{2\mu_0}{\pi} \frac{Iz}{(D^2 + 4z^2)}, \quad (3.15)$$

where \mathcal{B}_X is the field component in X direction generated by the Z-wire structure. This means that the magnitude of the X component changes with height, which consequently means, that the tilt of the field $\vec{B}_Y + \vec{B}_X$ changes with the height as well, as the two components have to be added vectorially. \vec{B}_X maximizes for $z = D/2$ to $\mathcal{B}_X = \mu_0 I / 2\pi D$. When we now compare the position of the minimum, which we would expect from a side guide, with the position of the minimum we get from the Z-wire trap, we see that the values differ slightly from each other because of the z dependance of equation 3.15. If we add now externally a field in X direction (\vec{B}_X), the trap will change slightly its position according to the new field (see chapter 5).

Figure 3.5 (right) is a contour plot of the field at the minimum in the X/Y plane. It reveals another important character of a Z-wire trap. Due to the contributions of the leads to the field in Z direction (stronger closer to the leads than in the middle of the structure), the trap is rotated around the X axis. When we characterize our trap, we approximate the trapping potential with a harmonic oscillator (valid near the minimum). The trapping frequencies are then proportional to the second derivative of the potential. If we derive this, we have to use a tilted coordinate system, to account for the rotated geometry (see figure 3.5 right). Using the derivatives along the geometrical coordinates would give a wrong result.

The problem can be solved, when we search for the eigenvectors and eigenvalues of the Hesse matrix.

$$\mathbf{H} = \begin{pmatrix} \frac{\partial^2 B}{\partial x^2} & \frac{\partial^2 B}{\partial x \partial y} & \frac{\partial^2 B}{\partial x \partial z} \\ \frac{\partial^2 B}{\partial y \partial x} & \frac{\partial^2 B}{\partial y^2} & \frac{\partial^2 B}{\partial y \partial z} \\ \frac{\partial^2 B}{\partial z \partial x} & \frac{\partial^2 B}{\partial z \partial y} & \frac{\partial^2 B}{\partial z^2} \end{pmatrix}$$

We have to diagonalize the Hesse matrix at the trap minimum. The trap frequencies are then simply

$$\omega_i = \sqrt{\frac{\lambda_i}{m}} \Big|_{(x_0, y_0, z_0)}, \quad i = 1, 2, 3, \quad (3.16)$$

where λ_i are the eigenvalues of the Hesse matrix, x_0, y_0, z_0 is the position of the minimum and i correspond to the different directions in space X, Y, Z . The eigenvectors $\tilde{x}, \tilde{y}, \tilde{z}$ are the new coordinate system of the tilted trap. The trap frequencies, which we get for the \tilde{y} and \tilde{z} direction, are almost equal, as the problem is point symmetric. We will note these in future as the

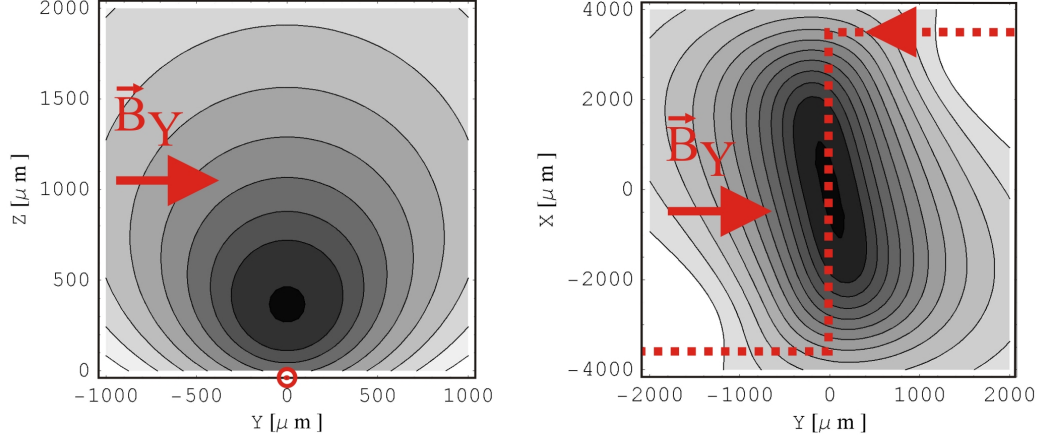


Figure 3.5: Contour plot of a Z-wire trap: the left figure is a cut through the Y/Z plane. The right figure is a cut through the minima of the trap. Here the tilt, due to the contributions of the leads is visible (lines are equipotential curves of 0,5, ... 65 G).

radial direction/trap frequency. In the \tilde{x} direction the trap frequencies are lower. We will note this as the longitudinal direction/trap frequency. The analytical expressions for the trap frequencies (derived with MATHEMATICA, see appendix D) are complex, and are therefore not displayed here, but all following calculations of trap frequencies and trap geometries include the full treatment.

Another important factor, which we have to include in our calculations, is the effect of gravity. It modifies the gradient and the position of the potential only in the Z direction as

$$\frac{dB}{dz} = \pm m \cdot g, \quad (3.17)$$

with g the gravitational constant and m the mass. Here one has to note the direction of the Z component (\pm in equation 3.17). If the trap 'hangs' (this is the case in our experiment), meaning that the Z direction points in the same direction as gravity, this will weaken the confinement and changes the position of the minima. Never the less, it is essential that the strong axis is always on axis with gravity (see figure 3.6).

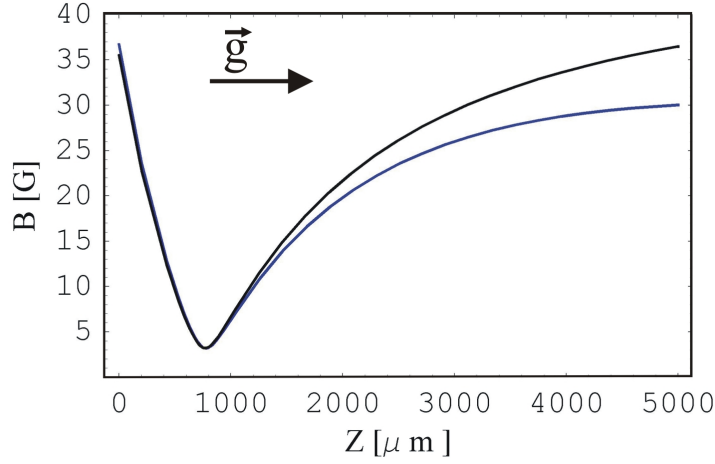


Figure 3.6: Gravitational effect on the trapping potential: gravitation points to the right (see arrow). Due to the gravitation the trap depth is reduced. The gravitational effect can lead to an atom loss, when the atoms have enough energy to overcome the trapping potential.

3.2.3 Finite size effects of real wires

When we deal with wire traps and when we calculate the magnetic fields we approximate the used geometries with infinite thin wires. This completely neglects the fact, that in real life, we have wires with a physical dimension.

The field of a cylindrical wire can be approximated with a infinite thin wire, but as we will see later, the wires used in this work are square on a mm to μm scale. There exists an analytic solution for the field of a infinitely thin and long, but broad wire [70, 25]:

$$B(z) = \frac{\mu_0 I}{\pi b} \operatorname{arccot} \left(\frac{2z}{b} \right) = \frac{\mu_0 I}{\pi b} \left(\frac{\pi}{2} - \operatorname{arccot} \left(\frac{2z}{b} \right) \right), \quad (3.18)$$

where b is the wire width, I the current and z is the distance from the center. When we compare this field (equation 3.18), with one from a infinite wire, we see that it differs. For distances $z < b$ and especially at $z = 0$ equation 3.18 simplifies to

$$B(z) \approx \frac{\mu_0 I}{\pi b} \left(\frac{\pi}{2} - \frac{2z}{b} \right) \quad (3.19)$$

$$B(z = 0) = \frac{\mu_0 I}{2 b}. \quad (3.20)$$

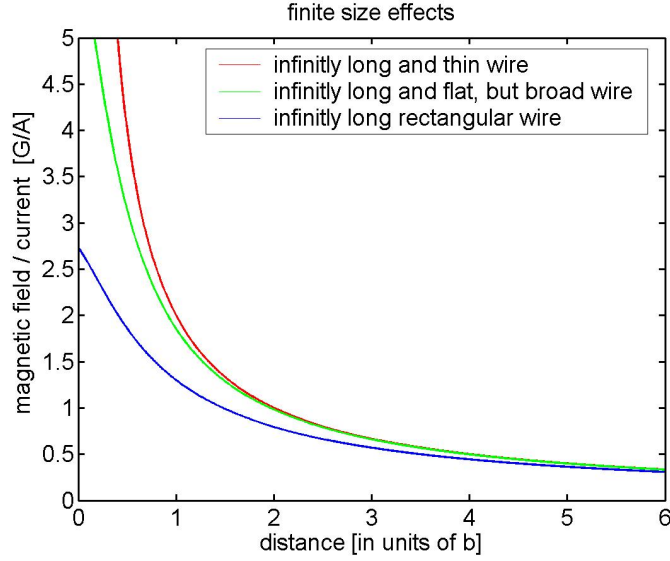


Figure 3.7: Finite size effect: the figure shows the magnetic field resulting from different wire geometries (infinitely thin - red, broad wire - green, broad and thick wire - blue). It is clear that when one approaches distances to the wire, which are comparable to its width, the gradient differ from the infinitely thin wire.

Equation 3.20 allows to give an upper limit to the trap depth as this is the maximum field the bias field can have (a larger bias field would move the trap into the wire). Here it is already clear, that we will get different results for the position of a trap compared to the ideal case in section 3.2.1. For the gradient of the real wire (equation 3.18) (still infinitely thin, but broad) we get

$$\frac{dB(z)}{dz} = -\frac{\mu_0}{2\pi} \frac{I}{z^2 + (b/2)^2}. \quad (3.21)$$

This behavior is different from the $1/z^2$ behavior as we would expect from a ideal wire. It is of a Lorentzian form (see figure 3.7). When we want to calculate real traps, even when they are simple, we have to take also the third dimension into account (up to now we introduced just the second dimension). There exists an analytical expression for a infinitely long but square wire (it is broad and wide, see Appendix D).

When we compare the fields generated by the different wire geometries (infinitely thin, two dimensions, three dimensions), we find that for distances

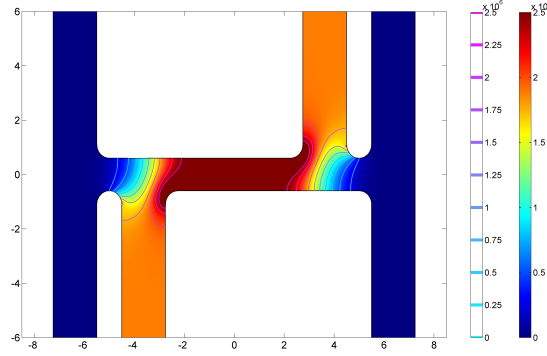


Figure 3.8: Current density distribution of macroscopic wires: we calculate the current density of a H shaped structure (later we will see, that we use this structure for generating a Z-wire trap). The current density distribution is different from the geometrical outline, and thus it reduces the central wire (see figure 3.4, parameter D). This we have to take into account, when we calculate the trapping potentials (scales are in mm).

large compared to the wire size, the different geometries give the same result. For distances comparable to the wire size, the finite size of the wires can no longer be neglected (see figure 3.7)¹. Most of the experiments presented in this work were performed at distances large compared to the wire dimension. We can therefore use the infinitely thin wire approach. Note here, that there is a second finite size effect, which arises from the fact, that our structures are bent, and due to this, the current flow will differ from the geometrical outline of the wire (see coming paragraph).

To address these problems, but still have a program which is reliable, fast and easy to handle, we choose a different approach. Using a finite size element program (FEMLAB), we calculate the three dimensional current density of the used wire structure, and then we modify, with the obtained current density, a simple infinite thin wire model. We found that this is a good and reliable way to treat three dimensional and complex wire structures. Figure 3.8 shows the current density of a structure, which we will discuss in detail in the experiment section. It is H shaped, and by addressing

¹To implement the third dimension, one can think that the wire geometry can be approximated in such a way, that one uses a bunch of infinitely thin wires and put them beside each other. This is problematic in two ways. One, it will be difficult to find an over all criterium on how much wires are necessary for the approximation and second the numerical effort can be huge.

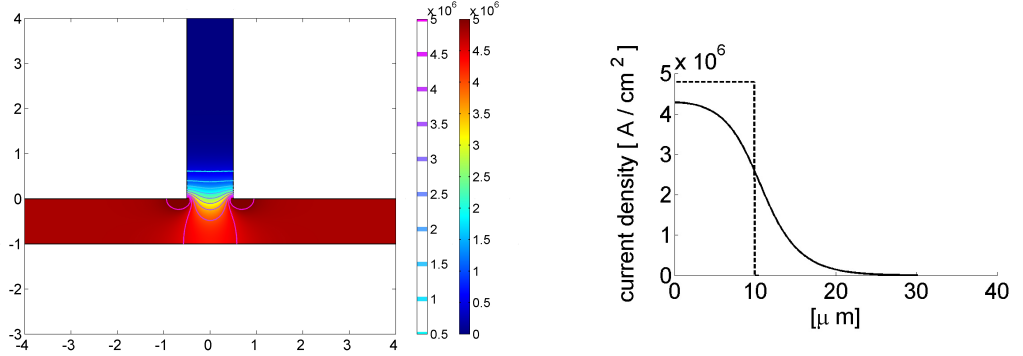


Figure 3.9: Current density distribution of a T crossing: a) the current flows in the horizontal wire, the perpendicular wire is not connected (dead arm). At the junction the current density is reduced. b) cut through the current density distribution at the junction ($X=0$). The current spreads out into the dead arm. If a side guide is generated, this can cause a potential barrier or a dimple in the side guide.

different ports it allows us to realize U- and Z-wire traps. Here we calculated the current density of a Z-wire geometry. The colors indicate the current density distribution. It is clear from the plot that the current path differs significantly from the geometrical one. The current density rises around the curves of the wire. This means that the current path is shorter than the geometrical path for the central wire. This we have to take into account, as for example equation 3.15 depends strongly on the distance D between the leads. Figure 3.9 shows another current density plot. Here we calculated a T crossing on a much smaller scale. The current flows just from left to right. The wire connected perpendicular to it is 'dead', meaning that there is no 'external' current flow. We see that the current spreads out into the dead arm. If we generate a side guide with such a wire (see section 3.2.1), the resulting trapping potential will have a dimple or a barrier in the potential (depending on the orientation of the structure with respect to gravity), where the 'dead' wire is connected to the structure. It can also be, that the adiabatic condition for this region is not fulfilled, and therefore, if a Bose-Einstein condensate is guided in such a structure, the condensate can loose atoms or can be excited by the distortion of the potential [71]. To calculate the magnetic field of the used wire and bias field arrangements we developed two kind of programs. One is a program written in MATHEMATICA, which analytically calculates the field, and second we apply MATLAB, which uses numerical methods.

Both programs use infinitely thin wires to calculate the trapping potential, but the geometric outline of the structures account for the current density distribution obtained by the finite element program. Note that we used the finite size program to calculate the current density and not the magnetic field, which would in principle be possible. But we found, that calculating the trapping potential does not always lead to a converging solution. This is due to the fact that we deal with quite different length scales. We have structures on a μm to a mm scale, but we want to know the magnetic field on a much bigger scale. But, as we saw previously in this paragraph, as long as we investigate traps which are much further away than the wire dimension, we do not get a significantly different result. This motivates our approach, that the modification of the geometry, due to the different current density distribution, which we put into the infinite thin wire model is valid. As we found out in the experiment, this is to a good approximation fulfilled.

3.2.4 Trap losses and heating

Now, as we can trap atoms in three dimensions, it is interesting to investigate trap losses and heating of the atoms. There are two major reasons for trap losses and heating. One is, as already briefly discussed, Majorana spin flips, secondly the noise on the current will also effect the atoms. In the case of high densities (for example a Bose-Einstein condensate), three-body losses will also play an important role.

Majorana spin flips

We mentioned already, that when the adiabaticity condition (equation 3.3) is not fulfilled, which means that the magnetic moment of the atoms can not follow the magnetic field, spin flips into untrapped states can occur. In the case of a Ioffe-Pritchard trap, as the Z-wire trap is, we can calculate the loss rate [63, 64](for a spin 1 particle)

$$\Gamma_M = 4\pi\omega e^{-2\omega_L/\omega} \quad (3.22)$$

where ω is the largest trap frequency of the treated trapping geometry. Note here, that ω_L depends on B_{IP} , the trap bottom. In general B_{IP} will be equal to equation 3.15. If we add an external bias field B_X to compress the trap, this is no longer the case. In figure 3.10 we displayed the dependance of the Majorana spin flip rate on the trap frequencies and on the trap floor B_{IP} .

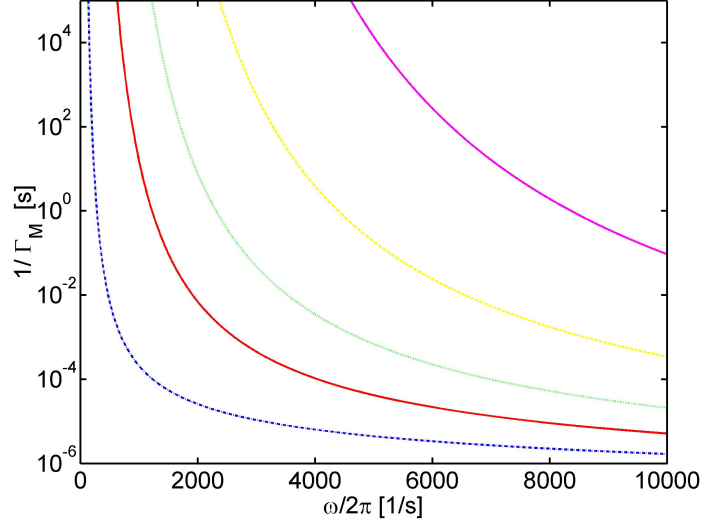


Figure 3.10: Majorana spin flip rate: the figure displays equation 3.22 ($1/\Gamma_M$) for different trap frequencies and different B_{IP} . The values for B_{IP} are: 1, 5, 10, 20 and 40 mG (blue, red, green, yellow and magenta).

Current noise

As we have to use a current to generate our trapping fields, noise on the current will effect the atoms. First it can induce spin flips and atoms will be expelled from the trap, and second it will modify the trap geometry, as a position shaking will lead to heating. The rate of these processes is given by Fermi's golden rule

$$\Gamma_{i \rightarrow f} = \frac{2\pi}{\hbar} \sum_{I,F} p(I) |\langle F | \langle f | H_{int}(I, i) | i \rangle | I \rangle|^2 x \delta(E_F + E_f - E_I - E_i), \quad (3.23)$$

where $|I\rangle$, $|F\rangle$ are the initial and final states of the environment, $|i\rangle$, $|f\rangle$ are the initial and final states of the atom. $E_{j=F,f,I,i}$ denotes the corresponding energies, $p(I)$ is the probability of $|I\rangle$ and $H_{int} = -\mu B(x)$ is the interaction Hamiltonian. Following the derivation in [72, 73], we can calculate the spin flip rate. In general we can write

$$\Gamma_{i \rightarrow f} \sim 0.01 s^{-1} \left(\frac{\mu}{\mu_B} \right)^2 \frac{S_{\alpha\beta}(r, \omega_L)}{pT^2/Hz}, \quad (3.24)$$

where r is the position, μ is the magnetic moment, μ_B is the Bohr magneton and $S_{\alpha\beta}$ is the magnetic noise spectrum (α, β denote magnetic field components). In equation 3.24 the Larmor frequency ω_L appears, as it is the relevant frequency in the system. Equation 3.24 gets more 'handy' if we evaluate $S_{\alpha\beta}$ for a side guide (single wire and a bias field),

$$S_B(r, \varpi) = \frac{\mu_0^2 e I}{4\pi^2 \hbar^2} \frac{S_I(\varpi)}{SN_I}, \quad SN_I = e \cdot I \approx 0.16 n A^2 \frac{I}{A}, \quad (3.25)$$

where SN_I is the shot noise, which comes from the discrete value of the electron charge e , I is the current in the wire, h is the height and $S_I(\varpi)$ is the noise spectrum of the current (here ϖ is a frequency range). The used notation, including the units, is motivated by the fact that the units are not in common use and are important when we want to compare experimental measurements and results to the theory. Substituting $S_{\alpha\beta}$ with the quantity derived in equation 3.25, and replacing ϖ with ω_L , as it is the relevant frequency, we get for the spin flip rate

$$\Gamma_{i \rightarrow f} \sim 1s^{-1} \frac{(\mu/\mu_B)^2}{(h/\mu m)^2} \frac{S_I(\omega_L)}{SN_I} \frac{I}{A}. \quad (3.26)$$

where $|i\rangle$ is the initial state of the atom before (trapped) and $|f\rangle$ is the final state of the atom (untrapped) after the distortion. Equation 3.26 will be, in general, significant at small height above a surface.

The current noise $S_I(\varpi)$ also distorts the trap in a geometrical way. This can be understood in such a way, that the DC current (direct current) produces the trap, and the AC component (alternating current) of the current, in our treatment the noise, causes the trap to shake. From the equations already derived, we know that this will result in a change in position of the minimum and in a change of the trap frequencies.

Consider atoms in the motional ground state $|0\rangle$ of the trap. The 'shaking' of the potential can induce a transition to the first excited state $|1\rangle$ of the trap, which means that the atoms are heated. The two contributions to the heating, trap position change and trap curvature change, can be written as

$$\begin{aligned}
\frac{dT_{0 \rightarrow 1}}{dt} &= \frac{\hbar\omega}{k_B} \cdot 3s^{-1} \cdot (m/amu) \cdot \left(\frac{\omega}{2\pi 100kHz}\right)^3 \frac{I/A}{(B_{IP}/G)^2} \frac{S_I(\omega)}{SN_I} \\
\frac{dT_{0 \rightarrow 2}}{dt} &= \frac{\hbar\omega}{k_B} \cdot 3 \cdot 10^{-8}s^{-1} \cdot \left(\frac{\omega}{2\pi 100kHz}\right)^3 \frac{1}{I/A} \frac{S_I(2\omega)}{SN_I}, \quad (3.27)
\end{aligned}$$

where m is the mass, B_{IP} is the magnetic field at the minimum of the trap, I the current through the wire and ω is the trap frequency. Note that $S_I(\varpi)$ can be easily measured using a spectrum analyzer, which is a standard measurement device in the lab. In the experimental section we will go into details of how to measure this quantity. The relations also motivate our development of ultra stable current supplies (for noise spectrums see Appendix E).

Note here that the noise does not only cause spin flips and heating, it will also effect the coherence properties of a coherent matter wave. Another effect, which is not treated here, are thermally excited currents (Johnson-Nyquist noise) in the metal surface. They will cause a magnetic field, which then subsequently couples to and influences the atoms. Both effects get significant at low distances. In this work we never performed measurements at distances ($< 100\mu m$), where these contributions will effect the measurement.

3.3 Evaporative cooling

As already discussed in chapter 2, the temperature of the laser cooled atomic sample is limited by the recoil momentum. Additionally the achievable densities are limited due to radiation pressure. All this is caused, because the atoms interact with light. To overcome these limits we have to employ a different technique. We introduced magnetic traps in section 3.2, which are capable to trap and hold large numbers of atoms just with magnetic fields. These kind of traps give rise to a new cooling mechanism, the so called evaporative cooling (also named radio frequency cooling). It was first proposed by Hess [74] for spin polarized hydrogen, but it is applicable to any trapped atom. The main task of the process is not only to reduce the temperature, but also to increase the phase space density $n\lambda_{dB}^3$ (n is the density and λ_{dB} is the de Broglie wave length) of the sample.

The physics behind this process relies on the fact, that from a sample of atoms (with a finite binding energy) the hottest are most likely to leave the sample. The remaining energy has to redistribute to fulfill the Maxwell-Boltzmann distribution. After this the average temperature is lower \rightarrow the sample is colder.

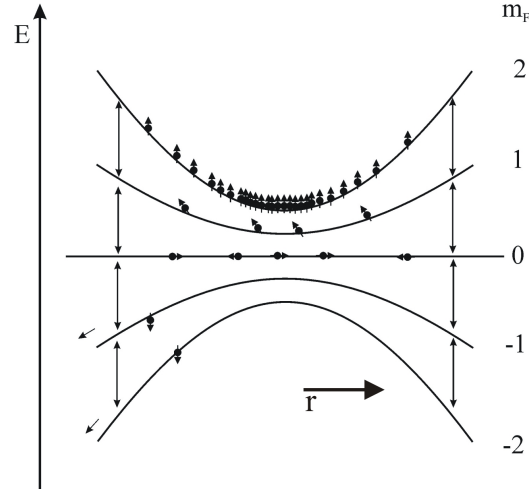


Figure 3.11: Evaporative cooling: due to the position dependent Zeeman energy splitting we can position selectively remove atoms by driving radio frequency transitions to untrapped states.

Let's transfer this picture to our situation. We have an atomic sample in a magnetic trap with a finite depth. The hottest atoms have enough energy to run up the potential and as a result they can be found at larger distances from the trap center (consequently colder atoms will be found close at or near the trap center). The atoms will experience, due to the inhomogeneity of the magnetic field, different Zeeman energy splitting ($E = g_F m_F \mu_B B(r)$) depending on the position of the atom. To remove atoms from the trap, we drive a radio frequency transition between two Zeeman levels. One is a trapped state, the other one is an untrapped state². The energy needed to drive this transition from one Zeeman level to another is

$$g_F \mu_B B = \hbar \omega_{RF}, \quad (3.28)$$

where ω_{RF} is the radio frequency. As the Zeeman splitting is position dependent (due to the energy of the atom), we can energy selective remove atoms from the trap (see figure 3.11)³.

When we now remove hot atoms from the trap, means that we cut off the tail of the Maxwell-Boltzmann distribution. The atoms will collide and

²It can also be that more than one RF photon is needed to reach an untrapped state

³Note here that the Zeeman splitting is still in the linear regime and therefore the splitting between the different hyperfine levels is the same.

reestablish a Maxwell-Boltzmann distribution, but now the mean temperature will be lower. Note here that both processes, the removal of hot atoms and the rethermalization are needed to increase the phase space density [75]. One process alone will not be enough.

A simple analytic model which describes the evaporation process is given in [76, 77]. The model treats the evaporation cycle as discrete steps with a truncation parameter $\eta = E_{cut}/k_B T$, where T is the temperature of the sample. For large η , a small fraction of atoms will leave the trap. The radio frequency cuts in, removes the atoms and then let the atoms thermalize in the unperturbed potential. The model shows that the best results (in gain of phase space density) is achieved in a 3 dimensional linear potential. This can be understood in such a way that the elastic collision rate

$$\frac{1}{\tau_{el}} = n \cdot \sigma_{el} \cdot v \quad , \quad \sigma_{el} = 8\pi a^2 \quad (3.29)$$

where n is the density, v the velocity, σ_{el} is the elastic collision cross-section⁴ and a the scattering length, responsible for the thermalisazion of the atoms, is highest for a linear potential as the volume scales as $V \sim T^{d/m}$ [32]. Here T is the temperature of the atoms, d is the dimension and m is the factor of the used potential $U(r) = r^m$. A Ioffe-Pritchard magnetic trap can be treated as in two dimensions linear and in one dimension harmonic. Our traps fulfill this condition.

The time scale on which the evaporation cycle should be performed is for example also dependent on the collisions with back ground gas atoms. If the pressure is high, background gas atoms will perturb the cold trapped atoms, and due to this we have an additional trap loss. In general, if the loss rate is high, evaporation must be performed fast. To reach the so called "run-away evaporation", meaning that the elastic collision rate increases with evaporation time, we have also to take two and three body losses into account. The ratio

$$R = \frac{\tau_{loss}}{\tau_{el}} \quad , \quad (3.30)$$

where τ_{loss} is the time it takes that an atom is expelled from the trap. τ_{loss} can be written

$$\frac{1}{\tau_{loss}} = G_{2b}n + G_{3b}n^2 + v_{HG}\sigma_{HG}n_{HG} \quad , \quad (3.31)$$

⁴In the temperature range of interest we can assume, that we just have s-wave scattering

where n is the particle density of the trapped atoms, n_{HG} is the density of the background gas, G_{2b} and G_{3b} are two and three body loss constants, v_{HG} is the mean velocity of the background gas, σ_{HG} is the cross section of the dominant background gas and n_{HG} is the density of the dominant background gas. Note here, that the three body loss is dominant for ^{87}Rb [78]. For "run-away evaporation" R has to be

$$R \geq R_{min} \propto \frac{\tau_{ev}}{\tau_{el}}, \quad (3.32)$$

where τ_{ev} is the time constant for the evaporation.

In an experiment we continuously remove atoms (we sweep the radio frequency). For this case the model has to be modified, but the principal aspects are still valid.

Chapter 4

Experimental realization

In this chapter we will give a detailed description of the experimental components and the procedure to reach a Bose-Einstein condensate. The chapter is structured in three sections. We start with the very basic components we need to manipulate atoms. Here the laser system, the laser stabilization and the vacuum chamber are discussed followed by a discussion of the mirror magneto-optical trap (MOT) and the atom transfer. The second part is engaged with the measuring and interpreting of the basic atomic properties of an atomic cloud, such as the number and temperature of the sample. The third part is completely dedicated to the achievement of a Bose-Einstein condensate. First measurements concerning the basic properties of a Bose-Einstein condensate are presented and discussed.

In addition we will report in section 4.1.3 and section 4.1.6 about results which were obtained in different setups. These setups were built in advance to the existing chamber to test some basic concepts.

4.1 Trapping, transferring and pre-cooling atoms

In this section we discuss the basic components we need for atom manipulation in general, in our case the spring board to achieve a Bose-Einstein condensate.

First we go into the details concerning the developed laser system. It must have features like a small linewidth, compared to the natural linewidth of the atoms (6.07 MHz in the case of ^{87}Rb), and sufficient laser power. Then we will address the vacuum part. For the vacuum system there are in principle two approaches. One can have one chamber, where the complete experiment is performed. Here the disadvantage is a short lifetime, due to

background collisions and limited optical access. The 'classical' approach is, having two chambers, one at a relatively high pressure (HP) and one in the ultra high vacuum (UHV), is our choice. This has the advantage of long lifetimes in the magnetic trap as we will discuss later in this chapter. It has the disadvantage that we have to transfer the atoms from the HP chamber to the UHV chamber. The atom transfer is closing the section.

4.1.1 The laser system

General remarks

For the operation of a magneto-optical trap (MOT) for ^{87}Rb , one of the elementary ingredients is a well controlled laser. The ^{87}Rb D2 line ($5s^2S_{1/2} \rightarrow 5p^2P_{3/2}$) is the atomic transition, which we use for this experiment¹. We need a laser system which fulfils the following conditions:

- small linewidth ($< 1 \text{ MHz}$) compared to the natural linewidth $\Gamma = 6.07 \text{ MHz}$
- stability to an atomic transition
- high laser power
- robust implementation and easy to handle

Note here, that we distinguish between the laser linewidth, and the stability to an atomic transition. In general a laser is free running, and due to environmental effects it will change its frequency. When we want stability to an atomic transition, we have to employ some feedback loop to keep the laser at the desired atomic transition.

Nowadays there are three approaches to satisfy the above requirements. There are Ti:sapphire lasers, tapered amplifier systems and grating stabilized lasers diodes. Out of a financial (Ti:sapphire lasers are expensive) and a historical reason (tapered amplifier lasers were not well tested when we started the project) our choice were self made grating stabilized laser diodes in a Littrow configuration.

In the coming sections we will discuss the different requirements, and how we solve the problems and how we implement the solutions into the experiment.

¹A complete study of the Rubidium lines can be found in [79].

Laser diode

A free running laser diode in general has a typical linewidth of $\sim 50 \text{ MHz}$, which is inadequate for laser cooling. However there are several schemes which allow to reduce the linewidth. All approaches have in common that they use a frequency selective feedback element. This can be an external cavity/etalon [80, 81, 82] or a grating [83]. In our setup we use a Littrow configuration (see figure 4.2), which uses a grating as frequency selective element. This ensures the small laser linewidth. The collimated laser beam shines onto the reflection grating, which is adjusted under the Littrow angle in such a way, that the first diffraction order is reflected back into the laser diode, forming an 'external cavity' (back facet of the laser diode and diffraction grating). The angle fixes the frequency range where the laser is operated (depending on the gain curve of the laser diode). The zeroth order is used for the experiment.

To ensure a good mechanical stability of the external cavity over time, a special laser diode mount was developed following the idea in [84]. We took special care in the choice of the used materials and components. With this method we achieved the desired linewidth ($< 1 \text{ MHz}$). To tune the laser in frequency, we simply shorten or lengthen the external cavity (this is done with a piezo crystal behind the grating). With this method we could achieve tuning ranges up to several GHz .

In figure 4.1 the complete electronic setup to control the laser diode is illustrated. The laser diode can be controlled via the so called 'lock-box' (LB)². When the laser is not stabilized, we tune the frequency continuously (scan mode), by applying a saw tooth voltage to the piezo crystal, which amplitude and offset can be adjusted by the LB. For the laser diode itself, as their wavelength changes with temperature and current, we need to temperature stabilize the setup (to $\sim 1 \text{ mK}$). For this we use a temperature controller³. A NTC (negative temperature coefficient resistor) is used to measure the temperature and a peltier element heats/cools the laser. A PID circuit (proportional (P) plus integral (I) plus derivative (D) circuit) in the temperature controller allows us to achieve the necessary temperature stability. In addition the applied current has to be extremely stable⁴. The current controller allows us in addition to add an external modulation to the current. Later we will see, that we use this feature for stabilizing the laser to an atomic transition.

²the LB is self built

³Profile, TED200

⁴Profile, LDC202

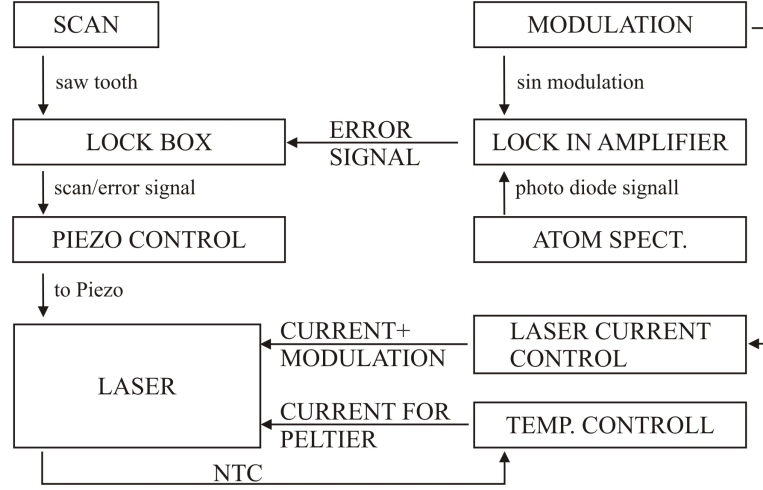


Figure 4.1: Electric circuit for the laser diode: during scan mode a saw tooth signal, amplified through the piezo control, is connected to the piezo behind the grating in the Littrow configuration; when the laser is frequency stabilized, the lock in amplifier generates the error signal, which is subsequently amplified and acts also on the pierzo crystal. The lock box allows switching from scan mode (amplitude and offset of the saw tooth can be adjusted) to lock mode. Here the lock box acts like a PID controller (Proportional plus Integral plus Derivative controller). The strength of the different shares can be adjusted in the lock box.

The piezo control⁵, which drives the piezo crystal has also to be noise free. A jitter would effect the cavity length and subsequently the output frequency. Note here that the maximum frequency, on which the piezo can act was measured to be 25 kHz. Figure 4.2 shows the complete assembly of the laser diode housing. For the picture a protective hood was removed.

Laser stabilization and spectroscopy

As we saw in chapter 2, it is important that the laser frequency can be stabilized to an atomic transition. A free running laser, without stabilization, will never stay at a specific frequency. Even small environmental effects (like temperature change or noise), will cause a frequency drift when the laser is not actively stabilized.

In order to stabilize the laser at a specific frequency, he have to know the frequency of the laser. The easiest way (in our case), to determine the frequency is by using atom spectroscopy with an Doppler free saturation

⁵type A128, self built; V=0-400V, 100mA

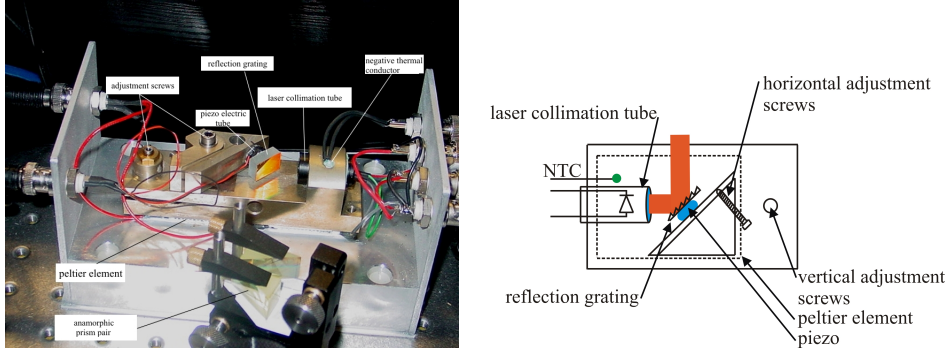


Figure 4.2: The laser diode housing (left): all the necessary components can be seen. Note the grating (with the piezo crystal behind it) and the collimation tube, which houses the laser diode. These two components form the external cavity, where the grating acts as a frequency selective device. In the front of the picture anamorphic prisms can be seen. They change the special laser beam profile from a elliptic to a round shape. Right: technical overview.

spectroscopy method [85] (in our case the D2 line of ^{87}Rb at 780.24 nm)⁶.

In order to stabilize the laser to a specific frequency, we have to have some kind of frequency dependent feedback to the laser, a so called error signal. This error signal can be applied to the laser in three ways, either to the current of the laser diode (the laser frequency changes with current) or onto the piezo crystal (a change of the external cavity length changes the frequency) or on both. There are various ways to produce such a error signal, but most of the schemes have in common that they use the atomic transition itself (and this signal we have already, as we used it to determine the laser frequency), on which the laser should be stabilized, to generate the error signal.

Figure 4.3 shows the basic setup for a Doppler free saturation spectroscopy. We use self built Rubidium vapor cells with good optical quality windows. In order to improve the spectroscopy signal (recorded with a photo diode), we subtract the Doppler background (obtained by letting a laser beam pass only once through the vapor cell). The Doppler background is then electronically subtracted from the Doppler free saturation spectroscopy signal, which contains the Lamb dips and cross overs [85]. The obtained signals can be seen in figure 4.4.

This spectroscopic method allows us to know the absolute laser frequency. To get the frequency dependent error signal we electronically produce the first

⁶For a complete overview of the Rb optical transitions, please see [79]

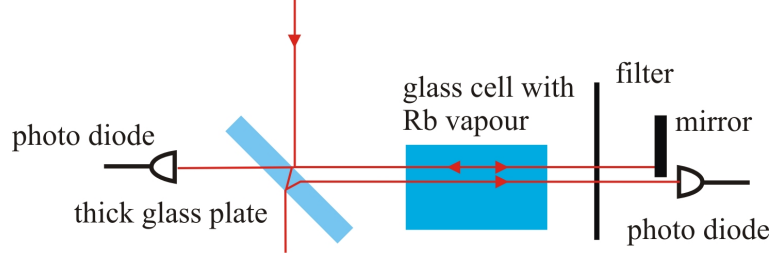


Figure 4.3: Setup to record a Doppler free atomic spectrum of ^{87}Rb . The thick glass plate is used to generate two parallel laser beams. The right hand photo diode, which records the laser beam after it passed only once through the vapor cell, gives just the Doppler broadened transition. The left photo diode, which records the beam after it passed through the cell twice, records the Doppler free absorption signal. To improve the signal quality, we subtract both signals.

derivative of the spectroscopy signal (blue line in figure 4.4). This is done with a simple Lock-In method [86], using a good Lock-In amplifier⁷.

We modulate slightly the laser diode current (through the modulation input at the current controller), which results in a modulation in the laser frequency (as mentioned above) [83]. The Lock-In can only see this modulation in frequency, when there is an atomic transition, and therefore gives out a signal. If there is no atomic transition, the Lock-In can't detect the modulation as the photo diode signal is constant, and puts out zero. The obtained signal is the first derivative of the atomic line spectra. It has a zero crossing at the maximum of a Lamb dip and is positive/negative on the edge of the atomic transition.

This error signal is now fed back to the piezo crystal via the LB, using a proportional-integral-derivative element (PID element). The electronic feedback effects the length of the external cavity, and so the laser frequency. When the laser is right on an atomic transition, the error signal is zero and the cavity length is unchanged. If the laser drifts, the error signal is different from zero and as a result, the cavity length is changed. When the phase of the error signal is adjusted correctly, the change of the cavity length brings the laser back to the desired atomic transition.

As mentioned, the error signal is applied to the laser diode via a PID loop in the LB. We can switch from the scan mode to lock mode (this is when the PID is on) continuously⁸.

In principle the error signal can also be fed back to the laser diode current,

⁷Stanford Research, SR 530

⁸for the electronic circuit please see Appendix A

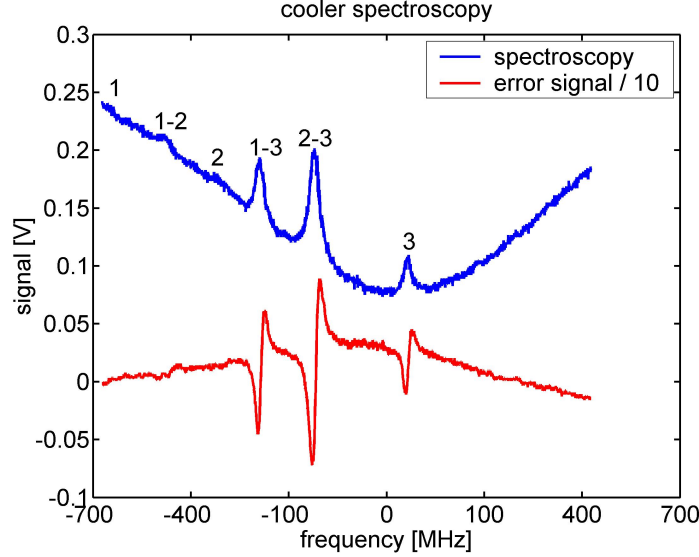


Figure 4.4: Doppler free saturation signal of the D2 transition $F=2 \rightarrow F'$. The signal shows clearly the single transitions, which one would expect from the level diagram A.1. The transition marked 1-2, 1-3, 2-3 are cross over signals. The signal below is the error signal, obtained with the discussed lock-in method.

but in our case, the bandwidth of the error signal is limited by the Lock-In amplifier, and it would make no sense to apply the error signal to the current. Never the less, for our purposes a feedback to the piezo is sufficient enough.

An error signal, which can also be applied to the current must have a larger bandwidth. Acting with the error signal on the current has the effect, that the laser linewidth can be further reduced ($\sim 10 \text{ kHz}$ range). In a diploma thesis [87], we developed the electronics for a frequency modulation feedback lock (FM lock) [88, 89] and a frequency offset lock [90], which generates a error signal, which is fast enough to be applied to the laser current. The developed lock scheme will be implemented soon in the existing laser system, as for future experiments it is required.

Off resonant stabilization

The described locking method allows us to stabilize a laser diode exactly on an atomic transition. For trapping atoms in a MOT, or for Molasses cooling it is necessary to be detuned by an amount δ (in the case of Molasses cooling this has even to change over time). Normally this can be done with a double-pass acousto optical modulator [91], on the cost of light power (one has to

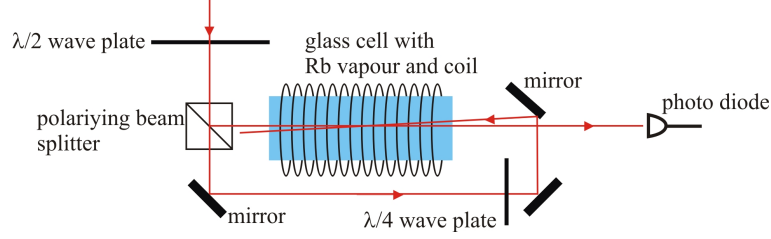


Figure 4.5: Setup for the Doppler free saturation spectroscopy used for off resonant stabilization. Note here that in contrast to figure 4.3 we have the possibility to apply a homogeneous magnetic field to the spectroscopy cell. This allows us to 'detune' the atomic transition due to the Zeeman effect. The $\lambda/2$ wave plate in conjunction with the polarizing beam splitter controls the intensity in the two exit ports. The $\lambda/4$ wave plate improves the spectroscopy signal, because with circular polarized light we pump the different magnetic sublevels, which are accessible due to the present magnetic field.

pass two times through the acousto-optic modulator (AOM), the diffraction efficiency of an AOM is typically 80%). The approach in our setup maximizes the available light power for the experiment. It is based on detuning the atomic transition with the help of the Zeeman shift. This approach does not require a double pass AOM. In figure 4.5 the spectroscopy setup is shown. It is almost identical with the setup seen in figure 4.3, but with the difference that around the spectroscopy cell a magnetic field coil is wound, and that the pump beam is circular polarized⁹. In normal operation (no B-field, coil current off) we observe the expected Doppler free saturation spectroscopy (see figure 4.4). When we switch on the B-field, the magnetic sublevels of the atoms experience an energy shift due to the Zeeman effect ($E = \mu|\vec{B}|$), which results in a frequency shift of the atomic transition. With the Lock-In method described above, we can now stabilize the laser to a Lamb dip or cross over, and then detune it changing the current in the coil. The resulting magnetic field of the coil, and consequently the frequency shift of the levels, determines the detuning of the laser. The current through the coil and thus the shift can be controlled externally by the experimental computer control.

When we stabilize the laser to the cross over transition 2 – 3 (see figure 4.4), we can detune the laser from this transition by $\sim 40 \text{ MHz}$ with the described method (see figure 4.9). In addition we can dynamically change the detuning on a time scale of $\sim 1 \text{ ms}$.

⁹The setup is almost identical with a polarization spectroscopy setup [85], except that the analyzer is missing

Measuring the linewidth of a laser

Now, as we can stabilize the laser to an atomic transition, we can easily measure the linewidth $\delta\nu$ of the laser (ν is the laser frequency). We have two identical setups in the experiment (for the repumping and cooling transition), we can use these lasers¹⁰.

By overlapping the beams of the two lasers and focusing them onto a fast photo diode (bandwidth $> 200 \text{ MHz}$), the two lasers will produce a signal on the photo diode of the form:

$$\begin{aligned} I(t) &\sim [E_{L1}(t) + E_{L2}(t)]^2 \\ &\sim [E_{0,L1} \sin(2\pi\nu_1 t + \phi_1(t)) + E_{0,L2} \sin(2\pi\nu_2 t + \phi_2(t))]^2 \\ &\sim A + E_{0,L1} E_{0,L2} \sin[2\pi(\nu_1 - \nu_2)t + (\phi_1(t) - \phi_2(t))], \end{aligned} \quad (4.1)$$

where $E_{0,L1}$ is the electrical field amplitude of the first laser, $E_{0,L2}$ the one of the second laser, $\phi_1(t)$ and $\phi_2(t)$ are the phases of the lasers and ν_1 and ν_2 the appropriate laser frequencies. A contains all high frequency terms. The second term in equation 4.1 will produce a oscillating signal on the photo diode with a frequency $\nu_{beat} = \nu_1 - \nu_2$, the so called 'beat note'. This signal, as it is moderate in frequency, can be measured with a photo diode. We lock the lasers to a atomic transition in order to have a fixed frequency difference (if the lasers are not stabilized, the laser frequency would change due to the environment, and the beat note would also change). As each laser has a linewidth $\delta\nu$, the beat signal will also show a linewidth $\delta\nu_{beat}$. To get the spectral information, we send the signal to a spectrum analyzer. The output of the spectrum analyzer can be interpreted as the spectral power density of the electric field $S_E(\nu)$ of the laser. The meaning of $S_E(\nu)$ is, how much laser power is in the frequency interval of 1 Hz around some frequency $\bar{\nu}$. The characteristics of $S_E(\nu)$ are determined by the nature of the frequency noise [92]. As measured earlier [87], we can assume that we have mostly flicker frequency noise, which results in a Gaussian profile¹¹ around ν_0 and the linewidth is then given by

$$\delta\nu_{1/f} = \frac{4}{\pi} \nu_0 \sqrt{\ln 2 \ln \left(\frac{5}{\omega_l \tau_c} \right)} h_{-1}, \quad (4.2)$$

¹⁰It is important to have two completely independent lasers

¹¹White noise would cause a Lorentzian shaped spectral density

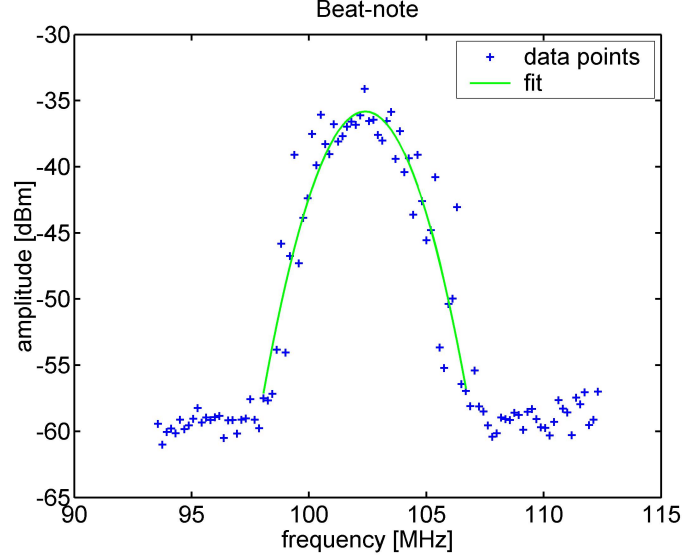


Figure 4.6: The beat note: the signal is recorded with a fast photo diode, and then it is Fourier transformed with an electrical spectrum analyzer. The linewidth measured is $<1\text{MHz}$.

with ν_0 the laser frequency, ω_l the lower cut-off frequency (because of a finite measuring time) and τ_c the coherence time of the laser.

The linewidth of the beat signal can then be calculated with (assuming a Gaussian distribution):

$$(\delta\nu_{beat})^2 = (\delta\nu_1)^2 + (\delta\nu_2)^2. \quad (4.3)$$

This holds only true if we can assume that both lasers have the same characteristic, which is fulfilled in our measurement setup. In figure 4.6 we can see a beat signal. The fit to it is a quadratic function as the scaling is logarithmic. In a linear representation it would be a Gauss curve as expected. We measure a linewidth for each laser of $<1\text{ MHz}$.

Master slave setup

Up to now we discussed grating stabilized lasers with low power. We use these diodes, because they are easy to control. But for trapping a large number of atoms, high power is required [53]. To gain more power we use a

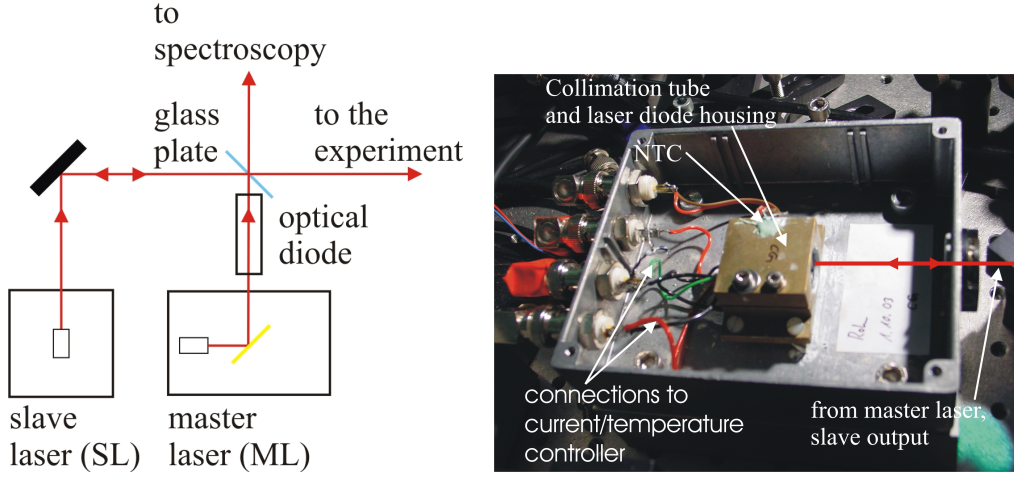


Figure 4.7: The slave laser mounting (right) and the the beam path (left) of the master slave setup. Some light of the master laser is seeded into the slave laser. Here the stability of the optical beam path ensures stable seeding of the slave laser. The right picture shows the slave laser itself. The high power laser diode is collimated and temperature stabilized.

so called 'maser-slave' configuration. The master laser (ML) is the discussed grating stabilized and well controllable laser, the slave laser (SL) is a high power laser diode, which can not easily be stabilized with a grating. A small portion of the light of the ML is fed into the SL. Because of the seeding light from the ML, the inversion for the free running mode of the SL is reduced and by choosing the right condition, such as current and temperature of the SL, the free running mode is completely suppressed and the SL runs only on the injected ML mode [93]. We monitor this behavior with an optical spectrum analyzer, a Fabry-Perot interferometer. We use $< 2 \text{ mW}$ of ML light to seed the SL and measure a capture range (this is the range where the SL follows the ML) of about 800 MHz , which is in good agreement with measurements performed in [94, 95]. To prevent back reflection from the SL into the external cavity of the ML, we use an optical diode (60 dB attenuation). As we found, it is not necessary to isolate the slaves from the experiment. Figure 4.7 shows the optical path and a picture of the SL. Note here that we took special care that the beam path from the ML to the SL is stable. This was awarded with a long term stability (no further optical adjustment) of $\sim 1 \text{ year}$ ¹². The used slave laser diodes give us $50 - 70 \text{ mW}$

¹²essentially we do not have to adjust the SL at all

of laser power¹³

Experimental implementation

We have now discussed all necessary components for the laser setup. The remaining part is the experimental implementation. Here we should first consider which laser frequencies are needed for the experiment (see Appendix A and figure A.1). The above table gives an overview of the needed light frequencies, to which atomic transition we stabilize the appropriate lasers to, and how the laser light is subsequently shifted in frequency to get the needed light.

needed atomic transition	purpose	stabilized to	frequency shift
$F = 2 \rightarrow F = 3$	cooling	cross over 2-3	shifted by magnetic field and AOM (+80 MHz)
$F = 1 \rightarrow F = 2$	repumping	direct to transition	-
$F = 2 \rightarrow F = 3$	imaging	cross over 2-3	shifted by AOM +133.3 MHz
$F = 2 \rightarrow F = 2$	optical pumping	cross over 2-3	shifted by AOM -133.3 MHz

The light for the last two points (imaging and optical pumping) are generated by the same laser. Figure 4.8 shows the beam path used in the experiment. Again special care was taken to ensure maximum stability of the used components to guarantee the mechanical robustness.

The light for cooling the atoms for the upper and lower MOT comes from two independent SL, which are seeded from the same ML. The ML is shifted from the cross-over transition 2 – 3 to the blue (with the method described in 4.1.1), and this light seeds the SL. As this variable detuning is not enough (see figure 4.9), the SL are further shifted by acousto-optical modulators. The AOMs in addition to the frequency shift are used for fast switching off of the light (switching times $\sim 3 \mu s$). To have sufficient laser light for repumping the atoms from the $F = 1$ state back to the cooling cycle, a single SL amplifies the light.

¹³during the development of the experiment, we used different SL diodes.

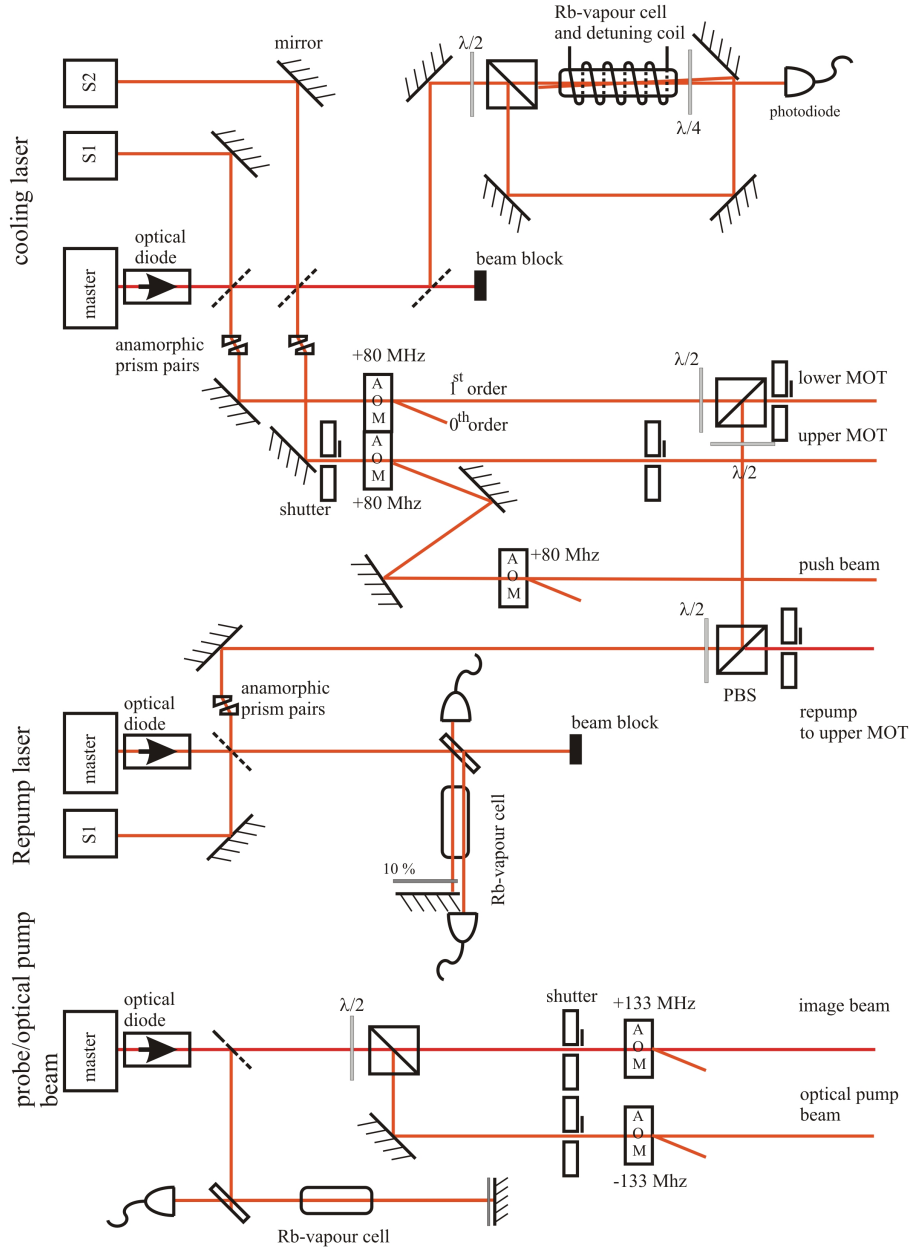


Figure 4.8: The complete laser system: it consists of the cooling and repumping laser for MOT operation. The cooling laser seeds two SL, one for each MOT. The repump laser seeds just one SL, which is then split in two for the MOTs. In addition we have a grating stabilized laser, the probe laser, which provides the light for optical pumping and imaging. The acousto-optical modulator (AOM) shift the light in frequency and acts as fast optical switches. In order switch off the light completely (AOM's have an extinction ratio of ~ 1000), additional mechanical shutters are installed for each laser beam. Note that for the probe laser just a simple Doppler free saturation spectroscopy, where the Doppler background is not subtracted is used.

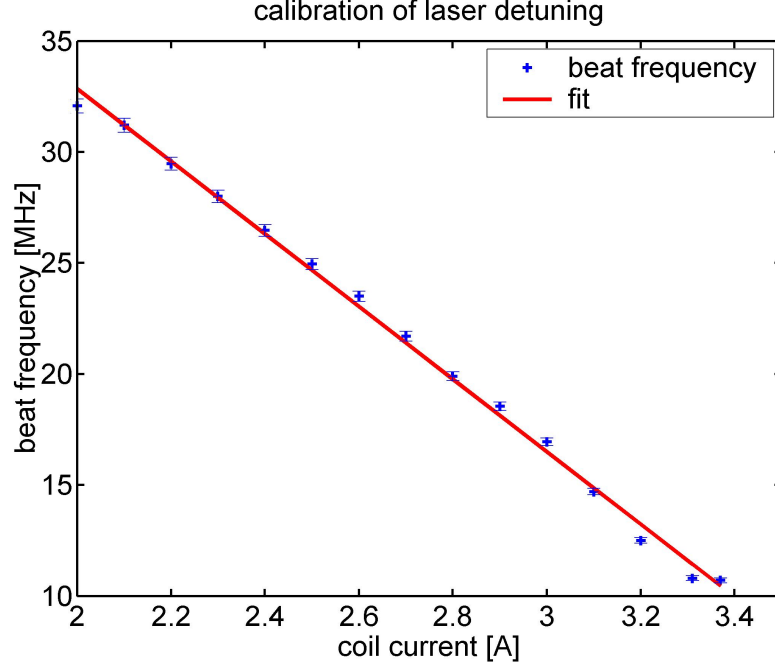


Figure 4.9: Coil current versus detuning: the signal is obtained in the same manner as figure 4.6. Two lasers (the cooler and the repump laser) are overlapped and the beat note is recorded with a fast photo diode and analyzed with a spectrum analyzer. Then the cooler is detuned with the Zeeman shift as described. Due to this, the beat note changes its frequency.

4.1.2 The double MOT apparatus

The vacuum system, like the laser system, has to fulfill a couple of demands, like a good pressure ($< 10^{-11}$ mbar) and a good optical access to the trapped atoms. Figure 4.10 shows the complete setup. In [96, 97] one can find a good description of the used setup. Therefore we will just summarize the main aspects.

As already mentioned, our choice is a two vessel vertical chamber with a transfer chamber in between (see figure 4.10). The lower part (which harbors the lower magneto-optical trap) consists of a six way cross of CF40 ports¹⁴ with anti reflection coated windows. In addition, there are six CF16 ports. We have three anti reflex coated windows on these ports, two for monitoring and measuring the magneto-optical trap and one to let the push beam in

¹⁴CF denotes an industrial standard for vacuum parts, the number is the inner diameter of the tube

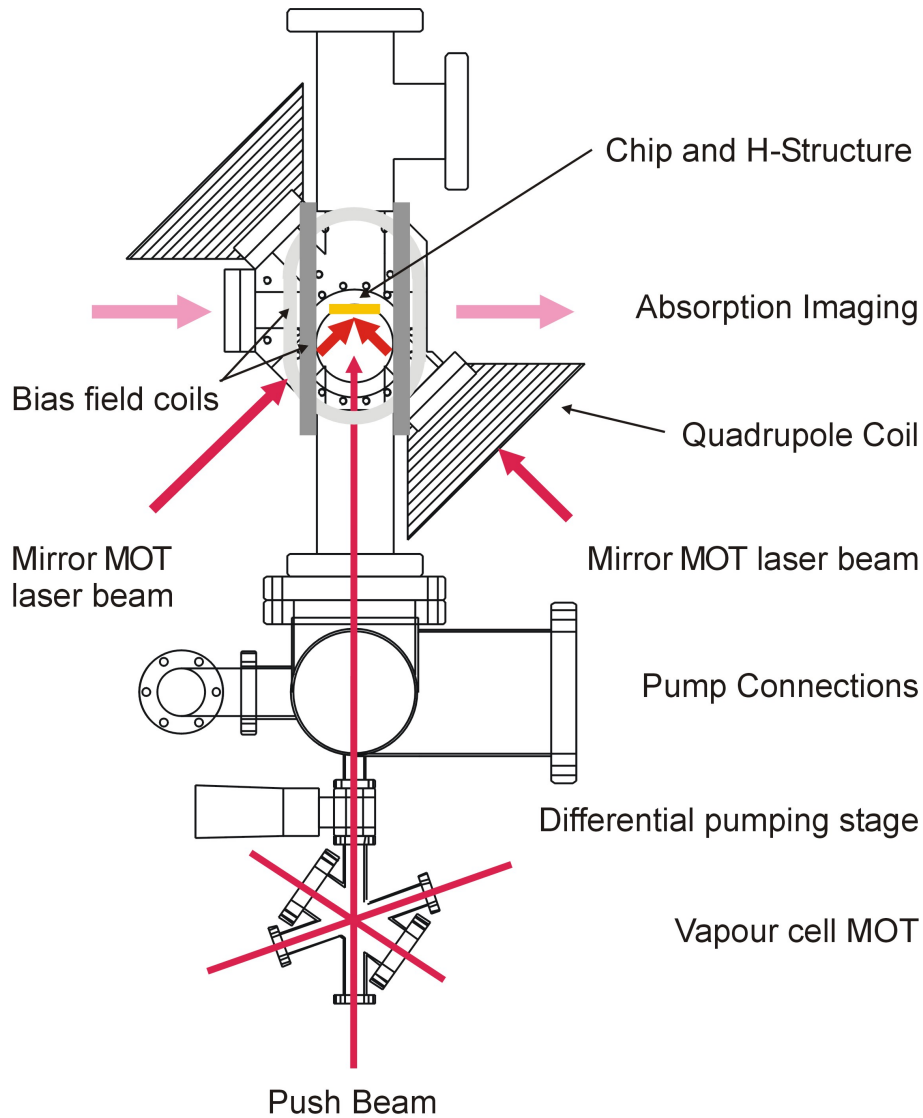


Figure 4.10: The double MOT apparatus: the main parts are the lower vacuum chamber for the lower MOT and the ultra high vacuum chamber, also called science chamber or upper MOT. Here the experimental cycle which leads to the Bose-Einstein condensate is performed. Note the good optical access as well as the compactness.

(see section 4.1.6). In addition, one port houses the Rubidium oven which is built from so called 'alkali metal dispensers' (in our case Rb). By running a current through these dispensers, Rb vapor is released¹⁵. An extra port is used to connect a 20l/s ion-getter pump, which brings us down to a pressure of $< 10^{-8}$ mbar. One more CF16 port connects the lower vessel to the transfer chamber. The gaskets in this case are not the normal oxygen free copper rings, but they look like a top-hat. The brim is the gasket and the rest is a tube¹⁶. The reason for the tube is, to ensure good differential pumping between the chambers. A 300l/s ion-getter pump with an additional titanium sublimation pump is attached to the transfer chamber. This assures a pressure $< 10^{-11}$ mbar. On top of the transfer chamber the science chamber is connected via a CF64 port. This chamber is made according to our demands. From the top, the atom chip holder with the wire traps can be inserted (see 4.1.3). Good optical access is achieved by the pan chake shape of the chamber, and by using special gaskets¹⁷. These gaskets allow the use of good optical windows. The windows are pressed directly onto the metal of the gaskets. Due to this they use less space and therefore smaller distances to the atoms can be realized. These gaskets are used for the two big windows and for the imaging axis. Here this is of special importance, because the quality of the windows affects the spatial quality of the absorption beam. One additional window under 45° is also sealed with this method, but for now it is not of special use. For a technical drawing of the science chamber please see the Appendix B.

4.1.3 The atom chip holder

In section 4.1.2 we described the vacuum vessel. In this apparatus the atom chip holder is inserted from above into the science chamber. It is the part which contains the wires. These wires (in conjunction with external fields) are used to provide magnetic fields to cool and magnetically trap the atoms. The considerations in 3.2 motivate the complex structure of the atom chip holder.

A wire bent into a U and Z enables to generate quadrupole and Ioffe-Pritchard type traps. In addition we want to realize more complex structures for magnetic guiding and manipulating atoms. From the scaling laws of equation 3.9, we saw that smaller structures enable more extreme trap configurations, but at the cost of trapping volume. To combine large trapping volumes, in order to trap a lot of atoms, but still have the advantages

¹⁵Company SAES

¹⁶These gaskets consist of one piece

¹⁷Helicoflex gaskets, Garloc

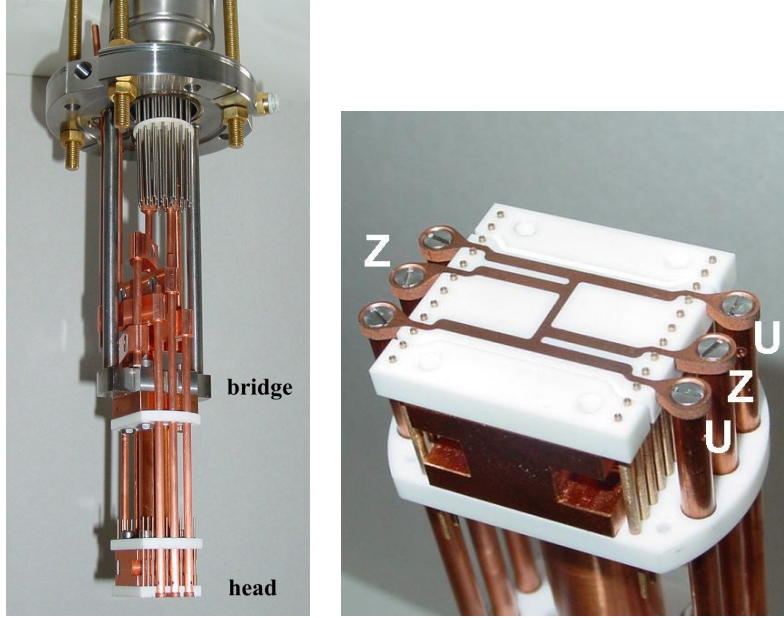


Figure 4.11: The atom chip holder: Left: the complete setup. The water cooled steel bridge and the connections to the H structure are visible. Right: the head of the atom chip holder. The H structure, embedded in the Macor piece, with the high current connections (on this picture, the atom chip is not mounted). The pins along the side are the copper Berillium pins. Later the atom chip pads are wire bonded to these pins. Connecting different ports allows different trap geometries (see section 4.3.1).

of miniaturized wire traps, we developed a two layer structure. One layer, the base, that enables U and Z wires to trap a large fraction of atoms and another layer, the actual atom chip, with more complex structures for advanced physics. This assembly is mounted on a copper and (stainless) steel column. The whole assembly is called the atom chip holder.

Figure 4.11 (left) gives an overview of the complete atom chip holder. We realized the base layer with a copper H structure (see Appendix C for a technical drawing). By addressing different ports, diverse U and Z wire traps can be realized. In order to attain sufficient trap depths and trap frequencies (see 3), we run currents of up to 60 A through this structure. To avoid heating, and as a result degrading the vacuum¹⁸, we kept the contact resistance as low as possible by bolting the H structure to massive copper rods of $\varnothing = 5$ mm. Four of the six rods are connected to high current feed

¹⁸due to evaporation of dirt from the structure

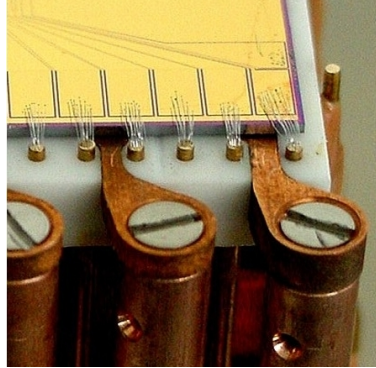


Figure 4.12: The atom chip bonded to the copper beryllium pins. We used $25\ \mu\text{m}$ aluminum wires to make the bonds. Due to the small size of the wires, it was possible have more bonds then necessary (the limit would be the maximum current of the connected wire). In this way we avoid that the wires act like fuses.

throughs (max. 60 A). The two remaining rods are fed through a 35 pin feed through, using 3 pins per rod (the maximum current is 10 A per pin).

To hold the structure in place it is embedded in a piece of Macor¹⁹. The atom chip (see section 4.1.4) is glued onto this Macor piece using a UHV compatible glue²⁰. One of the main difficulties was to contact the fragile wire structures on the atom chip to the 35 pin feed through. We overcome this problem by bonding $25\ \mu\text{m}$ aluminum wires from the atom chip to copper beryllium pins. The pins are held in the Macor piece. Up to 15 bonds per contact were made to ensure low contact resistance. Figure 4.12 shows typical bonding connections. The copper beryllium pins are then connected to copper wires insulated with Kapton²¹ and these in turn are connected to the 35 pin feed trough.

This assembly, the atom chip head, is bolted to a copper post. This post is then attached to a steel bridge, which can be water cooled from the outside. Current connections are welded in the CF 63 flange.

The water cooling was motivated to have the possibility to cool the atom chip. As it turned out, it was not necessary. Note here that in principle the used water cooling would not be of much help, because Macor has a heat conductivity of only $1.5\ \text{W/Km}$ ²². This should be improved with a next design of the atom chip holder.

¹⁹Macor is an easy to machine, UHV compatible ceramic

²⁰Epotec 920, Polytech GmbH.

²¹Kapton is a vacuum compatible polymere

²²in comparison, copper has a heat conductivity of $401\ \text{W/Km}$

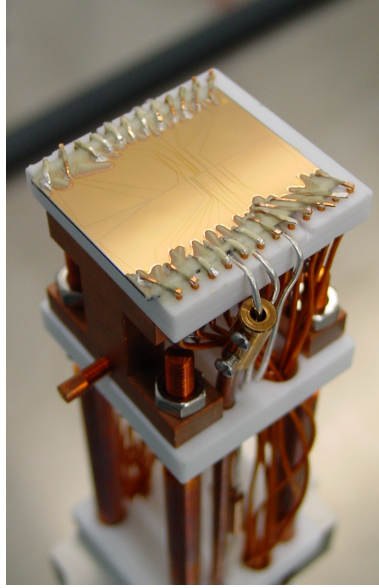


Figure 4.13: The old mounting: one can see the atom chip, which is glued to the head of the mounting, using small copper pieces (compare with figure 4.12). Here silver wires were used to generate quadrupole fields (U-wire) and Ioffe-Pritchard traps (Z-wires).

The whole configuration is inserted from the top using a CF 63 flange. First it has to go through a tube of $\varnothing = 63 \times 249 \text{ mm}$. When it enters the main body of the science chamber, the available space is $\varnothing = 50 \times 160 \text{ mm}$. The small outer dimensions put strong constraints to the construction. The length measured from the inside of the CF 63 flange to the atom chip surface is $247.5 \pm 0.5 \text{ mm}$. This brings the chip surface into such a position, that the laser beams for the mirror MOT (see section 4.1.5) can shine onto its surface at a 45° angle.

The described atom chip holder is based on an earlier construction. Figure 4.13 shows this setup. From a water cooled steel bridge four free standing poles held the atom chip head of the double layer structure, in this case the U and Z wires were independent and out of a silver wire with $\varnothing = 1 \text{ mm}$. The silver wire was pressed into grooves in the Macor. Two opposing U wires and one Z wire were realized in this way. The wires were connected to a 35 pin feed through. In the case of the U wires we found out, that the maximum current through this construction was 30 A, then the vacuum started to degrade, due to evaporating silver. The Z silver wire was connected to copper rods $\varnothing = 3 \text{ mm}$ shortly after the Macor. In this assembly the connections

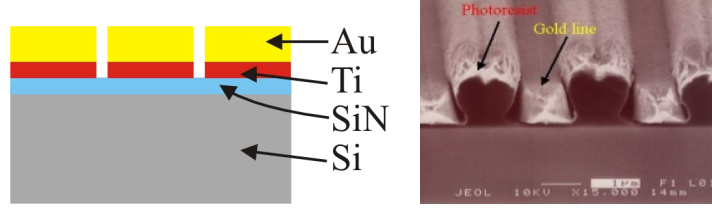


Figure 4.14: Left: the atom chip structure. It consists of a $700\text{ }\mu\text{m}$ thick silicon wafer. Different layers are then evaporated onto it and they form the actual atom chip pattern (silicon nitride 40 nm , titanium 40 nm). The last layer is gold, in our case $2.2\text{ }\mu\text{m}$ thickness, where the wires are etched into it. Right: a cut through a chip, where the photo resist, which is needed for the fabrication process, is still on the surface. In this design $1\text{ }\mu\text{m}$ wires are separated by $1\text{ }\mu\text{m}$ trenches.

to the atom chip where glued, using small copper pieces and a conducting glue. To ensure isolation, a non conducting glue was used in between the connections. It turned out that this method was not reliable (the connections broke), and the contact resistance was high. Furthermore, the large glue drops obstructed the optical access.

In the present setup, before the bonding technique was developed, a clamping technique was used to make the connections to the atom chip. For this we first stuck the copper wires through the Macor piece, and then formed a hook. The wire was pulled down until the hook made contact to the chip. The problem with this method was, that while baking the vacuum the wires got loose, and the connections failed.

4.1.4 The atom chip - basic concepts

The atom chip carries more complex wire structures than the copper structure. It is fabricated at the Weizman Institute of Science, Israel. The current design on the atom chip was made by R. Folman and P. Krüger.

The atom chip is a multi layer structure. The different layers are evaporated onto a silicon wafer of $25 \times 30\text{ mm}^2$. On top of this a silicon nitride layer of 40 nm is evaporated. It ensures isolation between the wires and the silicon wafer. Then a 40 nm titanium adhesion layer is applied. The final layer is the gold, where the wire structures are imprinted. The used atom chip has a $2.2\text{ }\mu\text{m}$ thick layer. Figure 4.14 shows a cut through a chip.

The wire sizes vary between $10\text{ }\mu\text{m}$ and $200\text{ }\mu\text{m}$. The resolution of the structures is 100 nm , and the distance between two wires is $10\text{ }\mu\text{m}$. The wires itself can be sculptured arbitrarily, depending on the physics that we want to study. In the present work only the Z wire in the middle was used

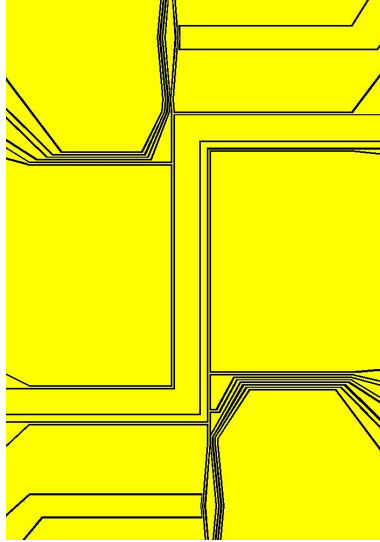


Figure 4.15: Detail of an atom chip: the displayed chip was designed and produced within the scope of this thesis. It shows Z structures (similar to the structure used for the chip experiment described in 5), and guides. Yellow indicates the gold surface, and the black lines are the trenches, which separate the wires.

(see section 5.2). Newer generations of chips reach gold layer thicknesses of up to $5\ \mu\text{m}$ and wire widths down to $1\ \mu\text{m}$ are possible.

Within the scope of this thesis, an atom chip was designed and later on built (by S. Groth). Figure 4.15 shows the central part with Z structures of different sizes. Long guides, up to $10\ \text{mm}$, are also realized in this design. The chip has not yet been built in.

4.1.5 The mirror MOT

In section 2.2, we discussed the working principle of an ordinary six beam magneto-optical trap (MOT). Here we characterize a special type of a MOT, the so called mirror MOT.

Normally a MOT is formed by six laser beams, either independent or retro-reflected. In the special case of a mirror MOT, only four independent beams are necessary. Two incoming beams, σ^+ and σ^- polarized, are reflected under 45° from a mirror surface [23, 98], in our case the atom chip. Due to the reflection under 45° from a metallic surface, a phase shift of π between the polarization components (parallel and orthogonal to the surface) is picked up. As a result, the circular polarization is changed from σ^+ to σ^- and the other way around. Two more laser beams, parallel to the atom chip

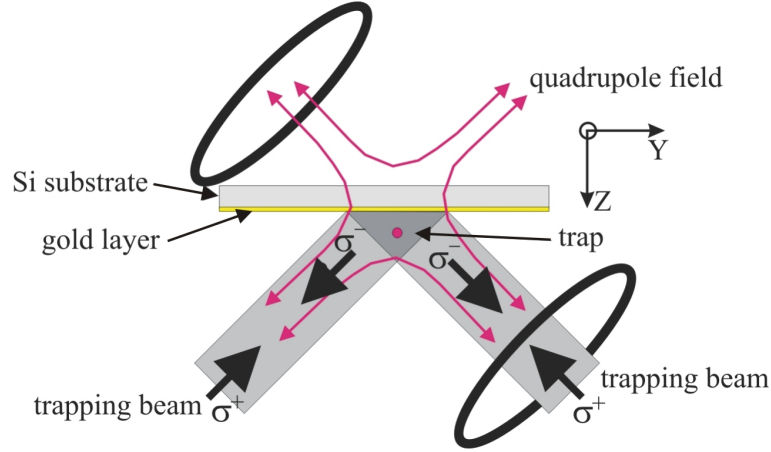


Figure 4.16: The mirror MOT: the laser beam configuration is quite different from the standard six beam MOT. Two circular polarized beams are reflected from the atom chip surface, changing the polarization upon reflection. Two more beams, parallel to the surface and perpendicular to the plane of the paper complete the laser beam configuration. Note here, that due to symmetry reasons/arguments, the quadrupole field has to be rotated by 45° to the chip plane.

surface, make the right constellation for a MOT. Considering symmetry of the laser beams and its polarizations, the necessary quadrupole field must be tilted by 45° . Figure 4.16 shows the operation principle of a mirror MOT.

The quadrupole field can be generated in two ways, with external coils and with a U shaped wire (see section 3.2.2). Here we discuss the used external coils. This MOT we will call the Q-mirror-MOT. The coils are of conical shape and they are water cooled. The shape of the coils allows good optical access to the atoms, as the image axis passes near by (see figure 4.10). The coil itself is mounted on an aluminum tube ($\varnothing = 80$ mm and 60 mm long), fitted with an end plate. A copper tube of $\varnothing = 3$ mm is 20 times wound around the tube. To increase the cooling, the copper tube is spiraling 4 turns on the end plate. The used isolated copper wire for the coil itself, is $\varnothing = 3$ mm. The smallest diameter of the cone is $\varnothing_s = 86$ mm, the biggest $\varnothing_b = 190$ mm. The coils have 204 and 206 windings respectively. To increase the thermal conductivity between the cooling tube and the wire, a thermal conducting epoxy is used²³. The distance between the coils is 220 mm. The coils are operated with a current of 32A. At this current the field gradients are 14 Gauss/cm on the 45° axis and 7 Gauss/cm on the radial axis²⁴. To

²³Stycast 2850 GT with curing agent Catalyst 17, Emmerson & Cuming

²⁴the coils were measured previously in free space

ensure good alignment the coils are attached to the diagonal CF40 ports of the science chamber.

4.1.6 The atom transfer

One of the difficulties to overcome, when using a double chamber system, is the atom transfer from one chamber/MOT to the other. In our case we transfer the atoms vertically with a continuous push beam [99] from a MOT in the lower chamber (lower MOT), to the mirror MOT (see section 4.1.5) in the upper chamber. The atoms are first pre-cooled in the lower MOT. This standard six beam MOT (with retro reflected beams) is penetrated from below with a continuous beam, the so called push beam. The push beam has a power of $< 1 \text{ mW}$ at the same detuning of the cooling beams. It is focused onto the lower MOT with a 200 mm lens (spot size of $\sim 10 \mu\text{m}$). It then propagates through the differential pumping stage and ends in the science chamber (the beam path can be seen in figure 4.10). As it is not retro reflected (the push beam hits the atom chip surface under an small angle), the momentum transfer to the atoms is just in vertical direction. With this method we can extract a cold atom beam from the lower MOT.

To measure the longitudinal velocity distribution we pulse the push beam using an AOM. We monitor simultaneously with a photo diode the fluorescence of the atoms in the lower and the mirror MOT (see section 4.2). The push beam is switched on for 20 msec, and a bunch of atoms escapes from the lower MOT. The atoms travel over a distance of $D \sim 50 \text{ cm}$ (distance from the lower MOT to the mirror MOT), and are recaptured in the mirror MOT. Figure 4.17 shows the recorded photo diode signal of the mirror MOT. The time delay T between the push beam pulse and the loading rate response gives the mean longitudinal velocity $\bar{v} = D/T$, and the time width Δt of the response gives the longitudinal velocity dispersion δv .

Integration of the assumed Gaussian velocity distribution $V(v)$

$$V(v) = V_0 \exp \left[\frac{-(v - \bar{v})^2}{2\delta v^2} \right]. \quad (4.4)$$

gives

$$V(v) = \delta v \sqrt{\frac{\pi}{2}} V_0 \text{Erf} \left[\frac{-\bar{v} + v}{\sqrt{2}\delta v} \right]. \quad (4.5)$$

Fitting this function to the data points in figure 4.17 allows to estimate \bar{v} and

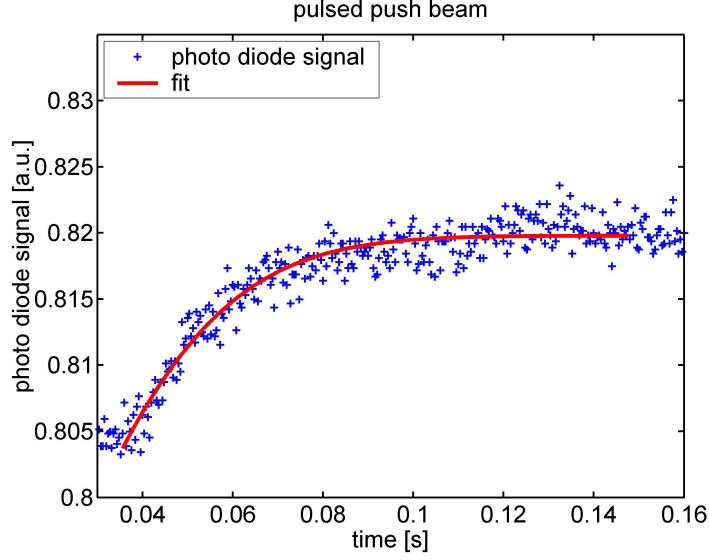


Figure 4.17: Loading behavior of the Mirror-MOT: the push beam is on for 20 msec, and extracts a cold atom beam from the lower MOT. With a photo diode the fluorescence of the Mirror-MOT is monitored. The sudden rise of the photo diode signal marks the arrival of the atoms. Fitting equation 4.5 to the data points gives us a velocity dispersion $\delta v = 20.7 \text{ m/s}$, and a mean velocity $\bar{v} = 28.4 \text{ m/s}$.

δv . The best fit gives for $\delta v = 20.7 \text{ m/s}$ and for $\bar{v} = 28.4 \text{ m/s}$. Estimating the temperature of the beam (in longitudinal direction) from \bar{v} , we get $\sim 50 \text{ K}$.

With this velocity, the two limits, gravity (3.1 m/s) and the potential barrier of the upper quadrupole field (1.1 m/s), can be easily overcome.

In [100] the atom transfer using this conditions was simulated with a Monte Carlo simulation. In this simulation the effect of gradients, arising from the quadrupole field, onto the atomic beam was studied. It was found that they can be neglected.

The obtained results are not a direct measurement of the actual atom beam velocity distribution, because we recapture the atoms in the mirror MOT and therefore the trap properties enter the measurement.

We performed initial tests with a different vacuum setup, in which the science chamber was replaced by a standard six way cross. In this vessel we had an ordinary six beam MOT. There the transfer efficiency was extracted from the loading rate of the lower MOT in comparison with the measured recapture rate [101]. A test on the influence of the detuning of the cooling laser beams (and respectively the push beam) was carried out. Here we

found that the maximum loading rate of the upper MOT was obtained with a detuning $\delta = 18(2) \text{ MHz}$, providing a loading rate of $3.9(9) * 10^8 \text{ atoms/s}$. The loading rate of the lower MOT was $2.9(6) * 10^9 \text{ atoms/s}$, giving a transfer efficiency of 13.4%.

With the present setup we found similar values, but slightly smaller. This could be the effect of the reduced capture volume of the mirror-MOT compared to a regular six beam MOT.

4.2 Measuring atom numbers and temperature

Knowing the atom number and the spatial distribution is essential in our experiments. All physical properties, like for example the temperature or the phase space density, can be deduced from these quantities.

One approach to obtain this information, is using resonant or near resonant light. The light interacts with the atomic sample, and either the scattered light (fluorescence light) or the 'missing' light (absorbed light) can be measured. In our experiment we used both approaches, the fluorescence and the absorption method.

4.2.1 The fluorescence method

With the fluorescence method, we can measure the number of atoms, using a calibrated photo diode (no spatial distribution information), or we can detect the light with a charge-coupled device camera (CCD camera) [102] (spatial information). The method is based on the fact that atoms, illuminated with resonant (or near resonant) light, will spontaneously scatter photons.

The number of atoms can be detected with a photo diode. We collect the scattered light with a lens, covering a solid angle of $\Omega/4\pi = 2.4(5) \times 10^{-4}$, and image it onto the detector. The photo diode current (I_{PD}) is given by:

$$I_{PD} = \Omega R P N_{Atom} , \quad (4.6)$$

where R is the photo diode efficiency ($R = 0.51 \text{ A/W}$ for $\lambda = 780 \text{ nm}$), P the emitted power per atom ($P = h\nu\sigma_{scat}$, σ_{scat} is the scattering rate) and N_{atom} is the number of atoms in the cloud. The scattering rate σ_{scat} is given by,

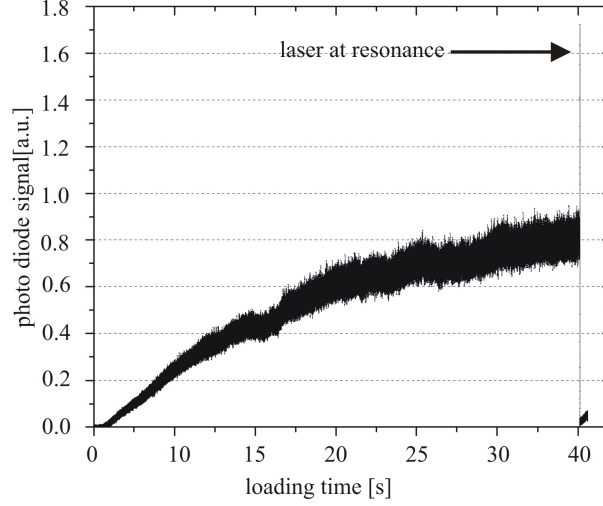


Figure 4.18: Loading of the mirror MOT: for the loading, the laser is kept at a fixed detuning. The photo diode signal rises, as more atoms are trapped in the MOT. Then, in this case after 40 sec, the detuning is brought to zero ($\delta=0$). The photo diode signal shoots up, as now the scattering rate is maximized. From the height of the peak, the atom number is calculated with equation 4.6.

$$\sigma_{scat} = \frac{\Gamma}{2} \frac{s}{1 + s + (2\delta/\Gamma)^2}, \quad (4.7)$$

where δ is the laser detuning and s the saturation parameter,

$$s = \frac{I}{I_s}, \quad I_s = 1.66 mW/cm^2. \quad (4.8)$$

The maximum scattering rate is obtained at $\delta = 0$ and $I > I_s$. Figure 4.18 shows a measurement with the fluorescence method. The atoms are first trapped in a MOT, then the laser is swept in 2 ms over resonance. From the peak at $\delta = 0$ one can calculate the number of atoms with equation 4.6. In the experiment we do not saturate the atoms ($I < 7 mW/cm^2$), and we therefore underestimate the number.

It is also possible to image the fluorescence light onto a CCD camera²⁵,

²⁵Pulnix, TM-6AS

and get the spatial distribution of the atoms. Because the sensitivity of the CCD chips is usually low, the exposure time has to be on the order of $\sim \mu s$. These long exposure times cause a significant momentum transfer to the atoms, leading to a heating of the cloud [103], and as a result, the measured distribution is broadened.

4.2.2 The absorption method

With the absorption method, it is possible to image small numbers of atoms. The used light is resonant with the $F = 2 \rightarrow F = 3$ transition, and it is mode cleaned with a fiber in order to get a good Gaussian beam shape. In the experiment the beam is expanded to 1 inch. The maximum intensity is $330 \mu W/cm^2$ ($\sim 1/10$ of the saturation intensity), to avoid saturation effects [104]. This beam will be noted as absorption beam.

An atomic sample, with a density distribution $n(x, y, z)$, will cause an attenuation, resulting in a shadow in the absorption beam (propagating in the Y direction). The absorption is

$$I(x, z) = I_0(x, z)e^{-\sigma_{abs} \int n(x, y, z) dy}, \quad (4.9)$$

with σ_{abs} the scattering cross section for the absorption of polarized light [105]:

$$\sigma_{abs}(I, \delta) = \frac{\alpha \sigma_{abs}^0}{1 + \alpha I/I_0 + 4\delta^2/\Gamma^2}. \quad (4.10)$$

Here σ_{abs}^0 denotes the resonant cross section of a two level atom ($\sigma_{abs}^0 = 3\lambda^2/2\pi$ and λ the wave length). α is a correction factor, which accounts for the case of a multi level atom. If the atoms are spin polarized in respect to the imaging axis (using a homogeneous field for example), circular polarized light can be used for absorption, and α is one. In our case the atomic sample is not spin polarized and the atoms are spread over all Zeeman levels. In this case, we have to average over all possible transitions using the Clebsch-Gordon coefficients. This results in $\alpha = 7/15$. In the following we put for simplicity α to one. Calculating the optical density then gives

$$D(x, z, I, \delta) = \sigma_{abs}(I, \delta) \int n(x, y, z) dy = -\ln \frac{I(x, z)}{I_0(x, z)}. \quad (4.11)$$

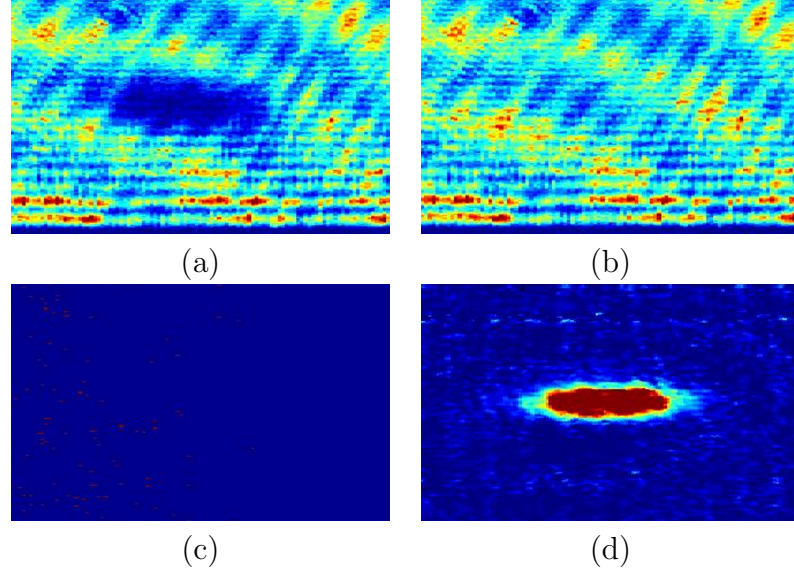


Figure 4.19: Absorption imaging: in one experimental cycle three pictures are taken. (a) is the absorption beam with the atoms (the shadow is clearly visible), (b) is the profile of the absorption beam (no atoms are present), (c) is the background image (complete darkness) and finally (d) is the picture after image processing (equation 4.11).

In the experiment, this means that we take a picture with the atoms ($I(x,z)$), and a picture from the unperturbed absorption beam ($I_0(x,z)$). To be correct we take a third picture with no absorption beam ($I_{dark}(x,z)$), and subtract this picture from the perturbed and unperturbed ones, in order to get rid of dead pixels and stray light. Figure 4.19 shows these three pictures and the resulting image.

With the optical density we have direct information of the spatial distribution of our atoms. The integral

$$\tilde{n}(x, z) = \int n(x, y, z) dy, \quad (4.12)$$

is the so called column density. When we assume $I/I_s \ll 1$, and put this into equation 4.11 and 4.12, we get for $\tilde{n}(x, z)$

$$\tilde{n}(x, z) = \frac{1}{\sigma_{abs}^0} \left(1 + \frac{4\delta^2}{\Gamma^2} \right) \ln \frac{I(x, z)}{I_0(x, z)}. \quad (4.13)$$

To calculate now the number of atoms, we simply have to integrate $\tilde{n}(x, z)$ and end up with

$$N_0 = \frac{1}{\sigma_{abs}^0} \left(1 + \frac{4\delta^2}{\Gamma^2} \right) \int \int \ln \frac{I(x, z)}{I_0(x, z)} dx dz. \quad (4.14)$$

In the experiment we usually have $\delta = 0$. When we now correct σ_{abs}^0 with $\alpha = 7/15$ we end up with the correct atom number.

4.2.3 Temperature measurement

With equation 4.11 we have direct information of the spatial distribution of the atoms. To measure the temperature of atoms in a MOT or in a magnetic trap, we use the so called time of flight method (TOF) [22]. The atoms are trapped, then we release them and take a picture after some time t . According to their velocity distribution \bar{V} , the atoms will fly apart. From the speed of the expansion one can calculate $\langle v^2 \rangle$, the mean velocity. The size of the cloud after the time t is determined by its initial velocity \bar{V} and spatial distribution \bar{X} . The spatial distribution after some time t is then the integral over all atoms of the initial distribution, which evolved during the time t to the position \vec{r}

$$\overline{X_{exp}}(\vec{r}, t) = \int \overline{X}(\vec{r} - \vec{v}t, t=0) \overline{V}(\vec{v}) d\vec{v}. \quad (4.15)$$

Here we switched off the trap at $t = 0$, and $\vec{v}t$ gives the distance the atom traveled in time t . We can assume the spatial and velocity distribution as Gaussian [4], and equal in all directions. Under these conditions we can separate all directions in space in equation 4.15, and we can write

$$\overline{X_{exp}}(x, t) \propto \int e^{-\frac{(x-v_x)^2}{2\sigma_x^2}} e^{-\frac{v_x^2}{2\sigma_{vx}^2}} dv_x, \quad (4.16)$$

where σ_x and σ_{vx} are the Gaussian widths of the spatial and the velocity distribution in x direction. The result of 4.16 is

$$\overline{X_{exp}}(x, t) = \frac{1}{\sqrt{2\pi}\sigma_x^2(t)} e^{-\frac{x^2}{2\sigma_x^2(t)}}, \quad (4.17)$$

with

$$\sigma_x(t) = \sqrt{\sigma_x^2(t=0) + (\sigma_{vx}t)^2}. \quad (4.18)$$

We can now define the temperature of a thermal gas as

$$m\sigma_{vx}^2 = k_B T, \quad (4.19)$$

where k_B the Boltzmann constant and T the temperature. Putting this into equation 4.18 we end up with

$$T = \frac{m[\sigma_x^2(t) - \sigma_x^2(t=0)]}{t^2 k_B}, \quad (4.20)$$

with t the expansion time. The quantity $\sigma_x^2(t)$ can be measured and $\sigma_x^2(t=0)$ can be either measured, or we can get it from a fit.

4.2.4 The imaging system

The method discussed in section 4.2 suggests already that we need an imaging system, respectively a CCD camera with optics. As we want to image small samples, we need a high resolution. In addition it should be flexible, meaning that it should image from large scales $\sim 1 \text{ mm}$ down to $\sim 100 \text{ }\mu\text{m}$ and below. For this we developed in a diploma thesis [106] a setup, which fulfills these conditions. In this section we restrict ourselves to the absorption method.

Figure 4.20 shows the developed setup. We first mode-clean the absorption laser beam with a fiber, and then expand it to 1 inch. The beam passes through a non polarizing beam splitter and through a quarter wave plate. The non polarizing beam splitter and the quarter wave plate are used to couple in the optical pump beam and to ensure its right polarization (see section 4.3.4). This beam is off when we take a picture. The beams enter the chamber through a CF40 anti reflection coated view port, and subsequently pass the atomic sample. The beams exit the chamber through a high quality window sealed with Helicoflex gaskets.

The lens system for the imaging consists of achromate lenses, which are corrected for chromatic aberration, spherical aberration and coma. The system ensures a diffraction limited resolution. The first lens is an achromate lens with $f=100 \text{ mm}$ and $\varnothing=30 \text{ mm}$ giving an f-number of $f/\varnothing=3.3$.

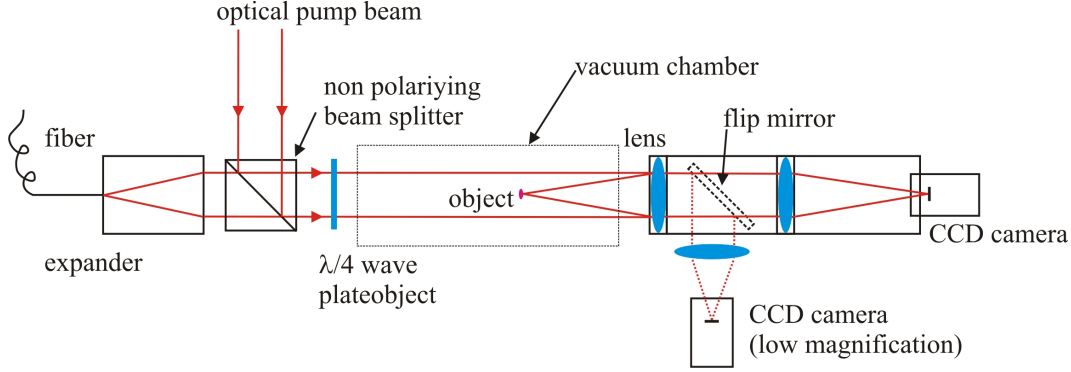


Figure 4.20: The imaging system: the flip mirror allows to change from a low (2:1), to a high magnification (1:3) with no further adjustment. The lenses for the high magnification give a diffraction limited picture at a resolution of $\sim 4 \mu m$.

As can be seen from the setup (see figure 4.20), we are able to switch between two image paths with a flip mirror. Both paths share the same first lens²⁶. When the flip mirror is in the beam path, we have a low resolution and magnification. In this case, the second lens is a commercially available camera lens²⁷, giving an image area of 20 mm^2 (we have a magnification of $1/2$). The used camera is an 8 bit, half frame camera²⁸ (half frame camera means that two rows are added, and therefore the pixel size is virtually enlarging to $16.6 \mu m$ for one side). This view is used for large atomic samples in the beginning of experimental cycle (see section 4.3.4).

When we want to image small atomic samples, for example a Bose-Einstein condensate, we flip back the mirror and use the 'direct' axis for imaging. With the second lens we can adjust the magnification. For most of the pictures in this work we used a lens configuration of $f=100 \text{ mm}/f=300 \text{ mm}$ giving a field of view of 4 mm^2 . With an f-number of 4 we would theoretically obtain a diffraction limit of $3.8 \mu m$. The system was tested separately and this value could be verified [106].

In the experiment we take three pictures with these cameras (see figure 4.19). One with the absorption beam and atoms ($I(x, z)$), one with just the absorption beam ($I_0(x, z)$) and one with no light at all ($I_{dark}(x, z)$). The $I_{dark}(x, z)$ is subtracted from the other two pictures and according to equation 4.11 and 4.14 the spatial distribution and the number of atoms can be calculated.

²⁶Melles Griot, 06LAI011, $f=100 \text{ mm}$, $\varnothing=30 \text{ mm}$

²⁷Nikon, $f=50 \text{ mm}$

²⁸Pulnix TM6AS, pixel size $8.6 \times 8.3 \mu m^2$, quantum efficiency $\sim 10\%$ at 780 nm

An 8 bit camera in some cases is not sufficient, because of the bad electronic resolution and the low quantum efficiency, as well as its large noise. We therefore installed a new camera with 16 bit resolution²⁹ with a pixel size of $20.5 \times 20.5 \mu m^2$. The back illuminated CCD chip is cooled down to a temperature of $-50^\circ C$ and has a very low noise figure, and a quantum efficiency of $\sim 40\%$. To get to the same resolution as we had, we use a lens configuration of $f=100 \text{ mm}/f=700 \text{ mm}$ (magnification 7). This camera has, beside the better quantum efficiency, the possibility of a frame transfer mode. This mode allows to move parts of the CCD chip electronically. We now cover half of the CCD chip with a mask, the rest is exposed to the absorption beam and so takes the actual picture (absorption beam and atoms, $I(x, z)$). This picture is moved electronically under the mask, so it can not be exposed again. Subsequently a second picture is taken (just the absorption beam, $I_0(x, z)$). After this, the whole CCD chip is read out. The image we obtain in this way contains both pictures. In a separate cycle, a dark picture can be made. The huge advantage of this frame transfer mode is that the delays between two pictures can be short ($\sim 30 \text{ ms}$). On this special feature, a diploma thesis is currently on its way [107].

4.2.5 Interpretation of the pictures

In section 4.2.3, we found the relation between the temperature T and the Gaussian width of the spatial distribution after some time t of free expansion. Figure 4.21 shows an expansion series recorded with the absorption technique.

We release the atoms at time $t = 0 \text{ ms}$, and let them expand for some time. We then switch on the absorption beam for $\sim 100 \mu s$, and simultaneously take a picture ($I(x, z)$). After a certain delay (in the case of the Pulnix camera, 300 ms, in the case of the Roper Scientific camera 50 ms), we take the second picture ($I_0(x, z)$). The dark picture ($I_{dark}(x, z)$) is taken afterwards. We can now calculate the optical density with equation 4.11, but now modified with the dark picture

$$D(x, z, I, \delta) = \sigma_{abs}(I, \delta) \int n(x, y, z) dy = -\ln \frac{I(x, z) - I_{dark}(x, z)}{I_0(x, z) - I_{dark}(x, z)}. \quad (4.21)$$

The pictures in figure 4.21 show the result of equation 4.21. When we now want to calculate the number of atoms, we take equation 4.14 and carry out the integration

²⁹Roper Scientific, TE/CCD-1152-EM/1,UV

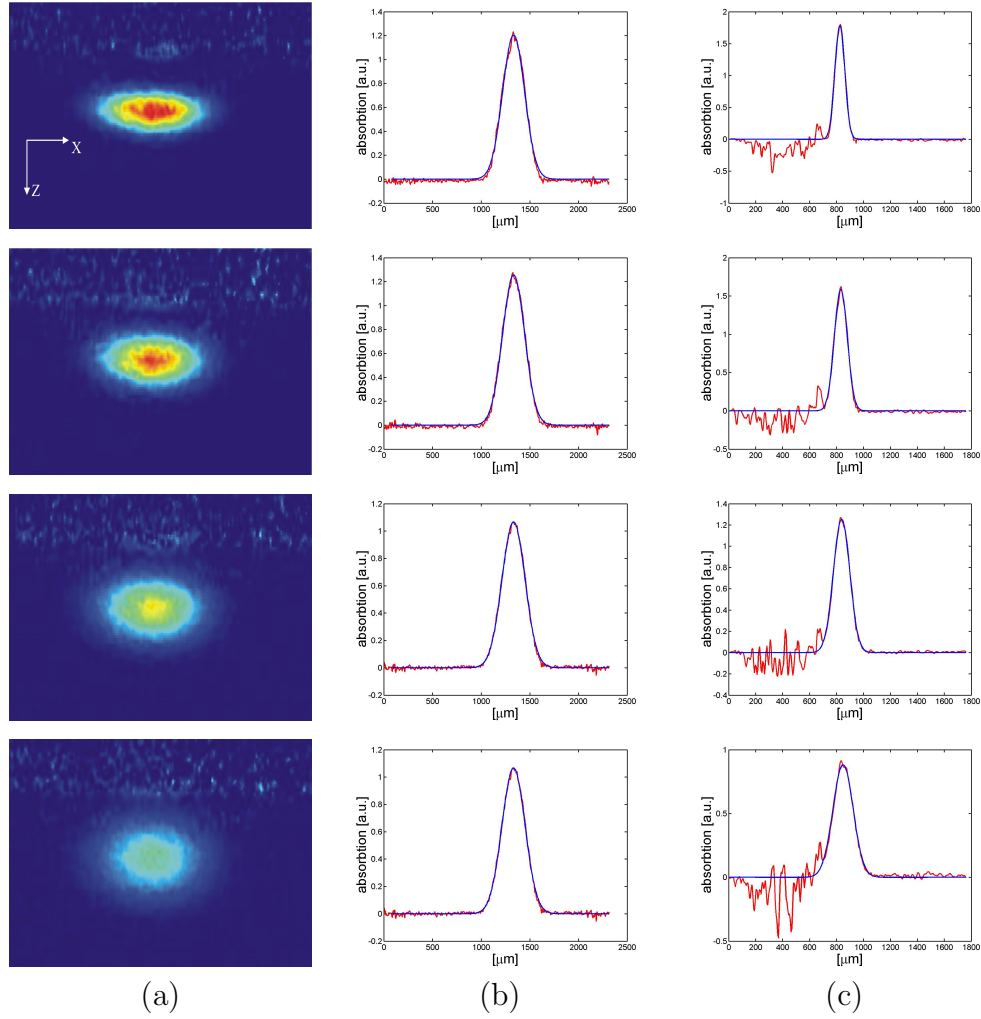


Figure 4.21: Time of flight: with this measurement we can determine the the temperature of the atoms. The atoms are first trapped in the magnetic trap, then the trap is switched off and the atoms expand. Column (a) shows the absorption pictures after 3, 4, 5 and 6 ms. Columns (b) and (c) show a cut through the X and Z axis with a Gaussian fit. The fit is done with a MATLAB routine.

$$N = \frac{1}{\sigma_{abs}} \sum_n \sum_m \ln \frac{I(x_n, z_m) - I_{dark}(x_n, z_m)}{I_0(x_n, z_m) - I_{dark}(x_n, z_m)} \Delta x \Delta z, \quad (4.22)$$

where Δx and Δz is the width and the height of the picture point (pixel size times magnification). This calculation is done with a home made software in MATLAB³⁰. Then we search for the maximum of the cloud. As the program allows us to treat the picture like a matrix, we can make a cut in X and Z direction and sum over 10 rows/columns around the maximum, in order to get a better signal to noise ratio. Then we fit a Gauss curve to the data. The program derives all relevant parameters of the Gauss fit. Our main interest are the Gaussian widths, σ_x and σ_z . With this we can derive the temperature according to equation 4.20. Figure 4.22 shows a temperature analysis. To make the fitting easier, we square equation 4.18 and plot the time squared against the width squared. Doing this we can make a linear fit to the data points and obtain from the slope K the temperature $T = \frac{Km}{k_B}$, where m is the mass of the atom.

In the case of a Bose-Einstein condensate the situation is slightly different. As we saw in chapter 1, the spatial distribution of a condensate is not Gaussian, but it is a inverted parabola. For this we simply have to modify the fit routine, to perform a bimodal fit.

4.3 Creating a Bose-Einstein condensate

The main purpose of the presented work was to create a sizable (atom numbers $>10^5$) Bose-Einstein condensate with magnetic wire traps. The condensation itself is done in these traps. In this section we report about the different steps of the experiment.

We start with a description how we implement the magnetic wire traps and the necessary bias fields in the experiment. The experimental cycle starts with the Q-mirror MOT (laser detuning $\delta \sim 12 \text{ MHz}$), where we collect and pre cool the atoms (see section 4.1.5). We then transfer the atoms in the so called U-mirror MOT, where, for the first time in the experiment, we use magnetic fields generated by wires (see section 4.3.2). This phase is followed by an optical cooling step, the Molasses phase (section 4.3.3), then we pump the atoms into the $|F = 2, m_F = 2\rangle$ state, which is a high field seeking state. Then we come to the most critical point in the experiment, where we load the magnetic trap, the so called Z-trap. The number of atoms we can load into

³⁰MATLAB is a programming language, specially designed for technical/physical use

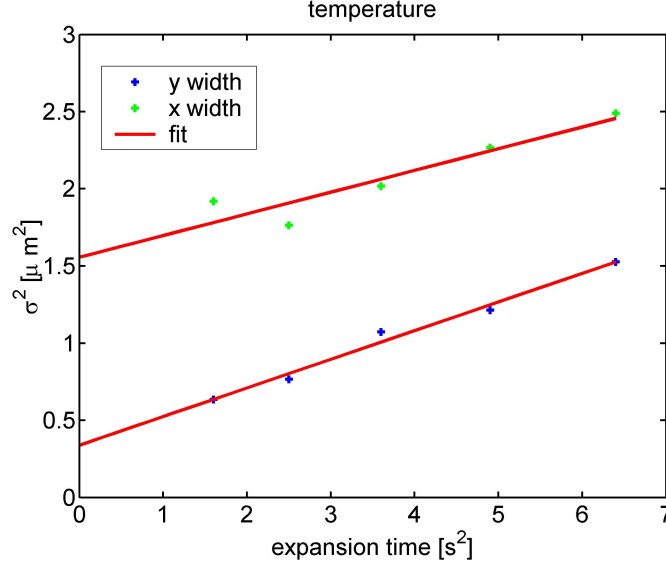


Figure 4.22: Temperature calculation: we let the sample expand and take absorption pictures after some time. From the width of the expanded sample we can calculate the temperature (see section 4.2.3). We square equation 4.18, and from the slope of the fit the temperature is obtained. In this case the temperatures are: $T_X = 1.4 \mu K (\pm 0.28 \mu K)$, $T_Y = 1.9 \mu K (\pm 0.28 \mu K)$.

the magnetic trap determines the success of the experiment. After this we compress and cool the atoms, using the evaporation technique, which results in a Bose-Einstein condensate of typically $3 * 10^5$ atoms.

4.3.1 Generating the magnetic fields

In principle we simply need a wire and a homogeneous bias field (see chapter 3). The wire is realized in our case with a massive copper H-structure, which is implemented in the atom chip holder (section 4.1.3). Most of the experiments presented in this work use this structure. The H-shape makes it extremely flexible, because it allows the combination of different ports and, as a result, different traps. It can also generate bias fields (see chapter 5). Figure 4.11 shows the H structure in the atom chip holder with the two most commonly used configurations indicated.

The necessary bias fields are generated in our case by coils in a Helmholtz configuration, outside the science chamber. We have three pairs for the three spatial directions. In addition to these bias fields, static fields in all directions are needed to compensate residual magnetic fields (for example

the earth magnetic field). The values for the coils are:

type	windings	\varnothing	dim. (H \times W [mm])	res. [Ω]	ind. [μ H]
X-bias field	32	2.1	120 \times 200	0.3	400
Y-bias field	32	2.1	120 \times 170	0.45	200
Z-bias field	18	1	370 \times 270	1.2	200
X-compensation	20	0.75	140 \times 220	2.4	*
Y-compensation	20	0.75	120 \times 170	2.4	*
Z-compensation	150	1.0	500 \times 330	8.0	*

When we constructed the science chamber we took special care of the outer dimensions. As a result the Y-bias coils are 65 mm, the X-bias coils are 45 mm apart. This allows us to have relatively small coils, resistances and inductances. The small inductance allows to switch off the fields on a μ s scale³¹. The Z-bias coils are 240 mm apart, but in the presented experiments they are of minor importance.

The compensation coils are of special importance, as their stability ensures, that once the magnetic stray fields are compensated, work under defined conditions is possible. To ensure the stability, special noise free power supplies³² and a low pass filters (cut off frequency <10 Hz) are used.

The bias fields are operated dynamically (we ramp the bias fields on a time scale of < 10 ms) in the experiment. Therefore the used power supplies³³ have to be noise free as well to avoid heating of the atoms (see section 3.2.4). A low pass filter is not possible in this case.

One important aspect is the strength of the used fields, as they form the trap. We measured the strength in two independent ways, one using a Hall probe, the other one using the atoms in the magnetic trap. As we saw in section 3.2.2, the position of the atoms in a magnetic wire trap is defined exact. The current through the wire, as well as the position of the atomic sample can be measured with great accuracy. From this information the bias field can be calculated. We compared the two results and found a good agreement (see figure 4.23).

When we switched off the magnetic Z-trap the atoms experience a homogeneous field, caused by eddy currents in the chamber and the Helicoflex gaskets. When measuring the atoms in the trap, or slightly after switching off the trapping fields, we observe lower atom numbers. This is due to the Zeeman shift of the atomic energy levels. The absorption beam (light at the

³¹we can switch of a coil of $\sim 100 \mu$ H with 1.5 A/s

³²HP 66312A, 0-20 V, 0-2 A

³³Z wire: Agilent 6551A, X/Y-bias: Agilent 6641A

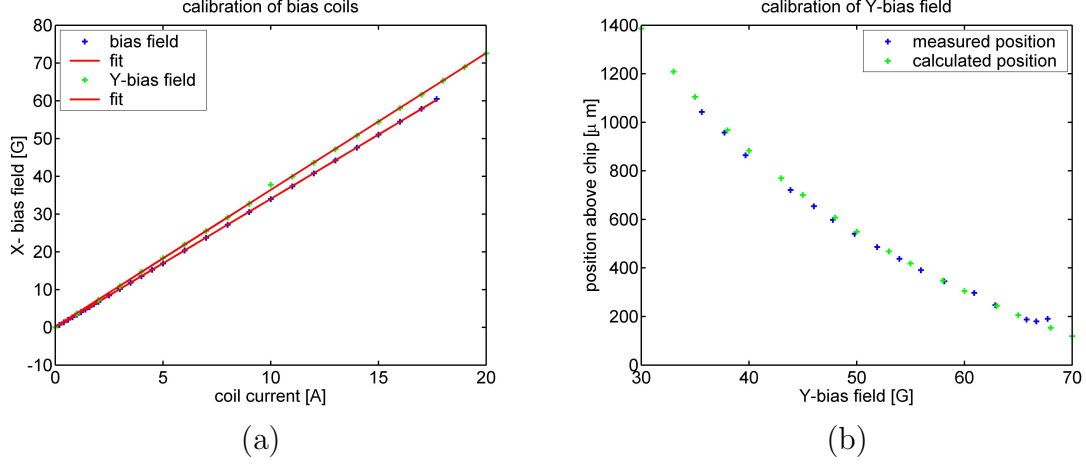


Figure 4.23: Calibration of the bias fields: the magnitude of the bias fields determines the trap parameters. a) the X- and Y-bias fields are measured with a Hall probe (we find for the X -bias field 3.40 G/A, for the Y-bias field 3.62 G/A). b) the position of the magnetically trapped atoms, depending on the Y-bias field, is measured ($I_Z = 49.6$ A).

$F = 2 \rightarrow F' = 3$ transition) is detuned relative to the shifted transition, and thus the atomic sample absorbs less light (see equation 4.14). Figure 4.24 illustrates this phenomenon. To overcome this, we always measured after 3 ms of expansion, to ensure a correct value for the atom number.

4.3.2 The U mirror MOT

After we collected atoms in the Q-mirror MOT (section 4.1.5), we transfer the atoms to the so called U-mirror MOT. The quadrupole field in this case is generated with a U shaped wire and a bias field (section 3.2.2). The advantage to have the atoms in the U-mirror MOT is, that we can switch off the fields on a $\sim \mu\text{s}$ scale and that the atoms are closer to the trapping region of the magnetic Z-trap.

In our setup the U wire is realized with the copper H structure, which is integrated in the atom chip holder (see figure 4.11). The bias field is provided by the coils around the science chamber (in Y direction). The transfer from the Q-mirror MOT is done by ramping up the U current, the Y-bias field and the Z-bias field in 220 ms to their final value. The Z-bias field causes the a tilt of the field (this improves the quadrupole field) and in addition it brings the trap center atop of the structure (this improves the spatial overlap with the magnetic Z-trap). The external quadrupole field is ramped down

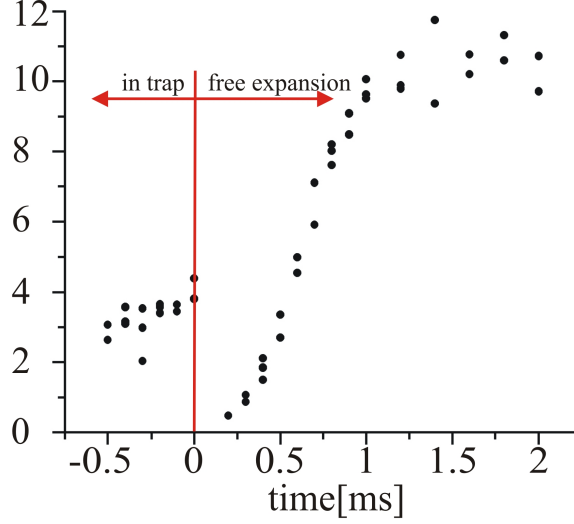


Figure 4.24: Atom number after we switched off the magnetic trap: the atom number in the magnetic trap is lower, due to a Zeeman shift. This Zeeman shift depends on B_{IP} , and therefore on the trap configuration. After the we switch off the magnetic trap, the atom number drops even further, and then rises to a value, and stays constant. This shift can be explained with an eddy current, induced into the steel chamber and the gaskets. The red line indicates the switch off of the magnetic trap.

in 150 ms with a 50 ms offset to the U-current (see the control chart in the Appendix F). Figure 4.25 shows the U current and bias field dependence. We normally operate the U-mirror MOT with $I_U = 29$ A, a bias field of $B_Y = 6.5$ G and $B_Z = 6$ G. The cloud is then 6 mm away from the atom chip. The distance to the atom chip can be varied by changing the bias fields or the U current (see figure 4.25).

Note here that the U-mirror-MOT can not be loaded directly, because the range where the quadrupole field is suitable for a MOT is too small. This can be improved, as mentioned, by tilting the bias field [67]. The tilt is achieved by using the Z-bias field.

Under typical experimental conditions we collect $\sim 10^9$ atoms in the Q-mirror MOT. The transfer to the U-mirror MOT is done with near unity efficiency. The relatively high gradients in comparison with the Q-mirror MOT lead to a compression. The loading process of the Q-mirror MOT and the transfer to the U-mirror MOT can be seen in figure 4.26 (the fluorescence light is recorded with a photo diode signal). The amplitude jump is a result

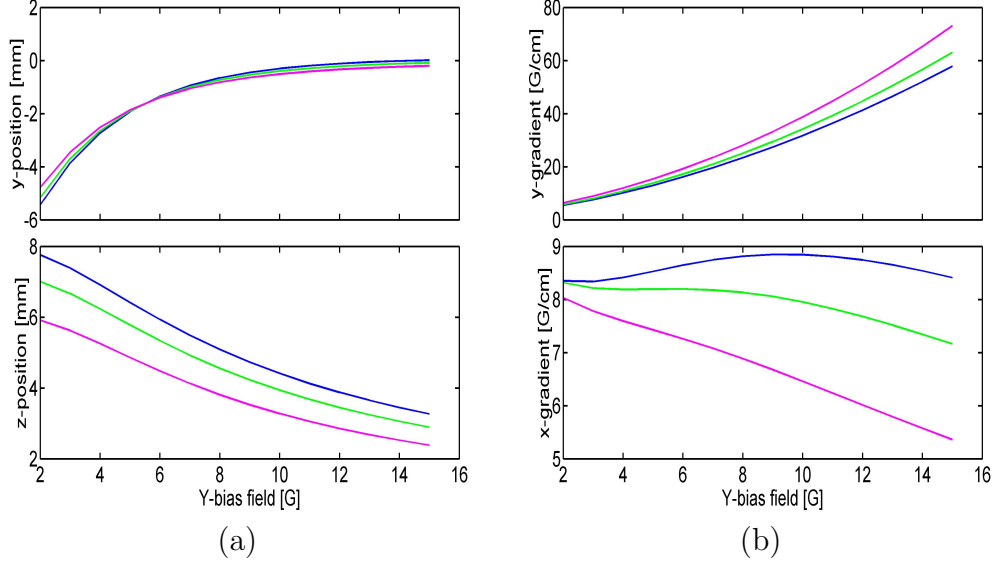


Figure 4.25: I_U dependencies: a) the Y-bias field is changed and the position of the minimum is calculated with our model. b) the change of the gradients in the Y and X direction. The colors in the different plots correspond to a I_U current of: 29 A (blue), 25 A (green) and 20 A (magenta). Note here that for the Y direction the minus means that the minima is not above the U-wire (see figure 3.2).

that the Q-mirror MOT and the U-mirror MOT are not at the same position. The fast decay of the trap is due to the poor quadrupole field. This decay would be normally not acceptable, but the time we keep the atoms in the U-mirror MOT is just 5 ms, until we switch off the fields to perform the Molasses phase.

In the previous test setup with the silver U wires we performed exact measurements of the transfer efficiency from the Q-mirror MOT to the U-mirror MOT. Figure 4.27 shows the results we obtained with different ramping times. We found the best results with ramping times of ~ 100 ms.

4.3.3 The Molasses phase

After the U-mirror MOT, we switch off the U-current and the bias fields and start the polarization gradient cooling, the so called Molasses phase (see section 2.3). As discussed in chapter 2 the limit for Doppler cooling in the case of ^{87}Rb is $T_{\text{Dopp}} = 145.5 \mu\text{K}$. This temperature depends just on Γ , the natural linewidth of the atoms. The additional process, the polarization gradient cooling, depends on δ , the laser detuning, and on Ω , the Rabi frequency. The

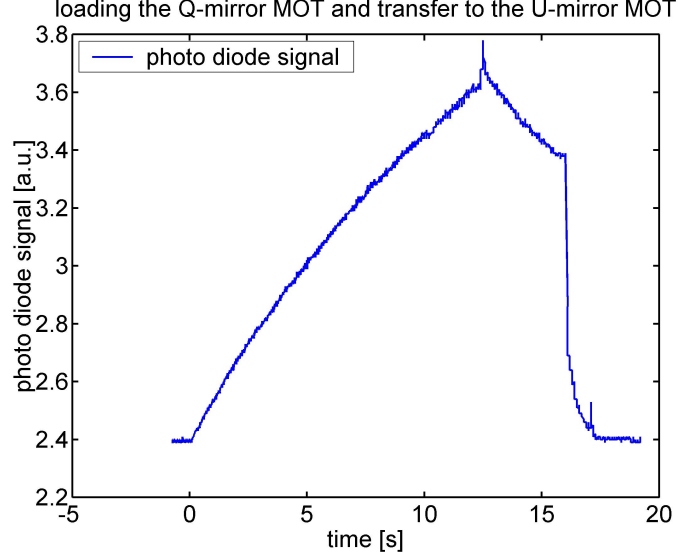


Figure 4.26: Loading of the Q-mirror MOT: a photo diode monitors the fluorescence of the atoms while they are collected in the Q-mirror MOT. Then the external quadrupole field is ramped down and simultaneously the current in the U wire and the bias field is ramped up. The jump in the photo diode signal indicates the transfer. Note the short lifetime due to the poor U quadrupole field.

Rabi frequency depends on the intensity of the laser beams. As mentioned in section 4.1.1, the laser detuning δ can be easily changed in our setup. We implement this into the experimental cycle in such a way, that we detune the laser further to the red in 15 ms, by keeping the intensity constant, and then the light is switched off. The detuning is done by simply changing the current through the detuning coil of the spectroscopy cell (see section 4.1.1). Figure 4.28 shows the temperature versus the detuning of the laser. We get a minimum of the temperature of $T \approx 30 - 80 \mu K$ with a detuning of $\sim 30 MHz$. Figure 4.30 shows a absorption picture of an atomic cloud after Molasses cooling.

The temperature is higher than expected. The reason for this could be that the atomic sample is too dense, and the cooling process breaks down. Another explanation could be that the necessary polarization is not good enough, as the atom chip has micro structures, and due to this, the reflection locally is not perfect. Frequency shifts in 5 ms are also possible and have the advantage that the cloud does not expand so much in this time. The Molasses phase is not only practical to reduce the temperature, but also to zero the magnetic fields. Residual magnetic fields cause an additional force

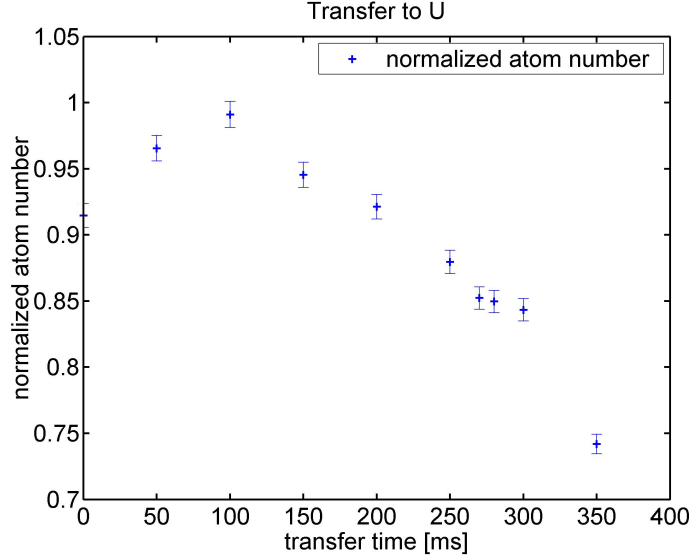


Figure 4.27: Transfer to the U-mirror MOT: the atoms are collected in the Q-mirror MOT. Then we transfer the atoms to the U-mirror MOT by ramping down the external quadrupole field and simultaneously ramping up the current in the U wire and the Y-bias field. This ramping time is varied. The graph shows the normalized atom number. Best transfer efficiencies are obtained at ~ 100 ms.

due to a Zeeman shift of the magnetic sublevels. As a result, the cooling forces are not balanced and the atoms are accelerated in some direction. By applying external compensation fields in the X, Y and Z direction this can be compensated.

When zeroing the magnetic field with this method, it is essential that the light intensities are perfectly balanced. Unbalanced intensities would also accelerate the atoms and as a result the magnetic field would not be zeroed correctly. We observe in the Molasses phase a shift of the cloud to the atom chip. This can be explained, by the reflection from the atom chip surface not being perfect. After the Molasses phase, the cooling light is switched off and we are left with atoms in all possible magnetic sub states. As we are only interested in atoms in the $|F=2, m_F=2\rangle$ state (we want to get a Bose-Einstein condensate in this state), only a small fraction ($1/5$ of the atoms) would be transferred to the magnetic trap. Therefore we optically pump the atoms into the desired state. A small guiding field along the Y axis is applied (by the Y-bias field coils, which we will use later for the Z-magnetic trap) to have a quantization axis for the atoms. We then shine in a σ^+ polarized laser pulse ($100 - 200 \mu s$ duration, depending on the laser power), which is

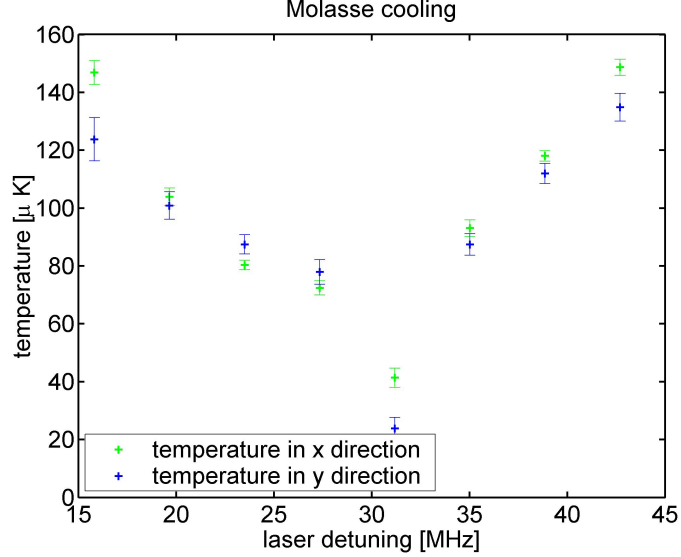


Figure 4.28: The Molasses phase: in order to cool the atoms, the laser is detuned (keeping the intensity constant). Green is the temperature in X direction, blue in Y direction. The graph shows how the temperature drops with detuning and then rises again. The temperature is not following perfectly the theory. The reason for this could be that the polarization, necessary for polarization gradient cooling, is not perfect after a reflection from the atom chip.

tuned to the $F = 2 \rightarrow F' = 2$ transition. Due to the present magnetic field and the polarized light, we can pump the atoms from all different magnetic sublevels into the $|F = 2, m_F = 2\rangle$ state (see figure 4.29 and figure A.1). This state can not interact with the light and is therefore a so called dark state. While we do this we keep the repump light on, to ensure that atoms in the lower hyperfine state are pumped back into the optical pump cycle. After the optical pump pulse, all light is switched off. With this method we can increase the number of atoms in the magnetic trap by a factor of 2-4. Figure 4.29 shows the dependence of the polarization. A quarter wave plate, determining the polarization of the optical pump beam, is rotated and the atom number in the magnetic Z trap is measured with the absorption technique.

4.3.4 Loading the magnetic trap

The magnetic Z-trap is realized with the copper H structure, using two opposing ports of the device (see figure 4.11). Here we have two possible sizes

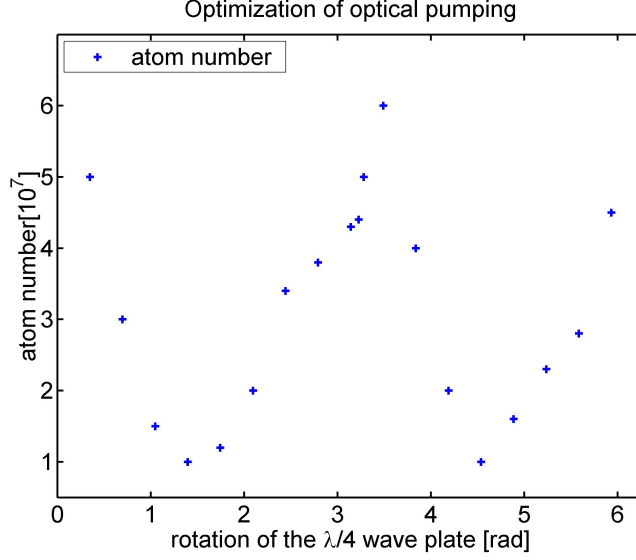


Figure 4.29: Optical pumping: a $\lambda/4$ wave plate in the optical pump beam is turned in order to optimize the optical pumping process. The atom number in the magnetic trap is monitored. When the polarization is exactly σ^+ , the atom number rises, due to the fact that most of the atoms are now in the high field seeking state.

for the center wire of the Z, the large one with 12.75 mm and the small Z with 7.25 mm. In this work we used the small Z. It will be noted as the Z wire. The bias fields are generated, as mentioned, by external coils.

In the Molasses phase, we prepared an atomic sample of $\sim 30\text{--}80\ \mu\text{K}$. Due to the relative long detuning time ($\sim 15\text{ ms}$), the cloud expands to a size of $\sim 5\text{ mm}$. We start the loading process by ramping up the Y-bias field and, $500\ \mu\text{s}$ later, we ramp up the current in the Z wire in $\sim 2\text{ ms}$. As described in section 4.3.3, we apply the optical pump pulse in the first $\sim 100\ \mu\text{s}$, when the Y-bias field rises. After this, all light (the repump was still on for the optical pumping) is switched off. The initial magnetic Z trap is operated with 50 A and a Y-bias field of 25 G. The trap frequencies are then $\omega_X = 2\pi 15.2\text{ Hz}$ and $\omega_Y = 2\pi 55\text{ Hz}$ and a trap depth of $\sim 500\ \mu\text{K}$, which is sufficiently deep for our temperature. Figure 4.30 shows the currents in the Z wire and the Y-bias field.

The critical parameter during the transfer is the phase-space density (PSD) $n\lambda_{dB}^3$ (n is the density and λ_{dB} is the deBroglie wave length of the atoms), which should be conserved. When we transfer a spatially symmetric cloud (in our case the Molasses cooled atoms) into a harmonic trap, the

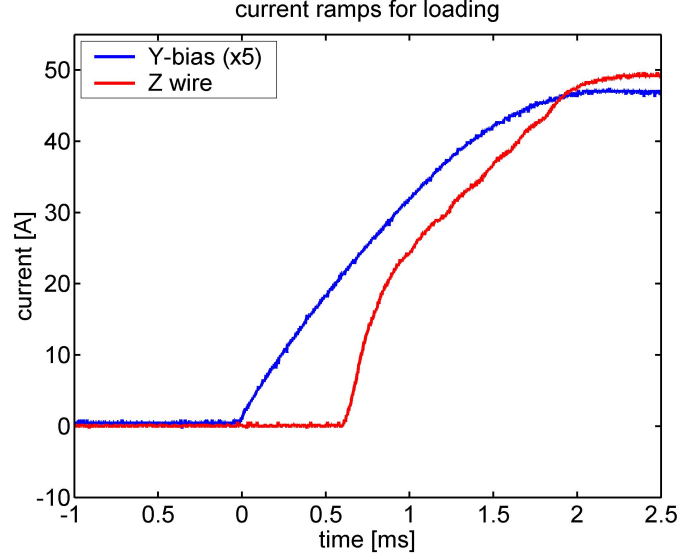


Figure 4.30: Loading of the magnetic Z trap: the current in the Z wire (red) and the Y-bias field (blue) are ramped up. The complete ramping time is 2 ms. The Y-bias field is ramped up in advanced. Right after the rise of it, we use the Y-bias field for providing us the guiding field we need for optical pumping.

PSD is conserved when we have

$$U(r) = \frac{1}{2}\kappa r^2, \quad \kappa = \kappa_0 = \frac{k_B T}{r_0^2}, \quad (4.23)$$

where κ is the stiffness of the trapping potential, r_0 is the size of the initial cloud and T is its temperature [104]. If now $\kappa \neq \kappa_0$ we get for the PSD

$$\frac{PSD}{PSD_0} = \frac{8(\frac{\kappa}{\kappa_0})^{3/2}}{(1 + \frac{\kappa}{\kappa_0})^3}. \quad (4.24)$$

If the magnetic trap is now too stiff, the atoms will heat up. If the trap is too shallow, the atom cloud will expand, and this expansion will not be adiabatic. In both cases the PSD will be reduced.

When we assume now a fixed temperature of 100 μK , the mode match criterium is fulfilled in a good approximation along the axial direction of the wire, but the trap is too small in radial direction. Therefore we observe

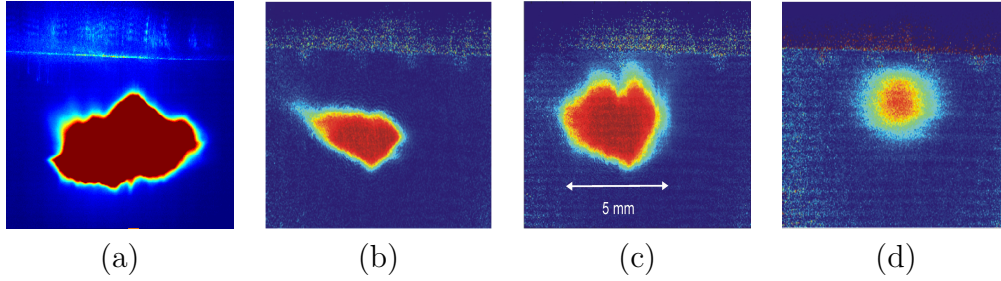


Figure 4.31: Loading of the magnetic trap: the steps to load the magnetic Z trap. a) the Q-mirror MOT after finishing the loading process with the push beam, b) shows the U-mirror MOT just after the atoms were transferred from the Q-mirror MOT. c) shows the atoms after the Molasses phase. The atoms are now cold ($\sim 30 - 80 \mu K$), but the cloud is 5 mm. d) the atoms in the magnetic Z trap. As we saw in section 4.3.4, the fraction of trapped atoms can be increased with optical pumping. All pictures were taken with the absorption technique.

heating when we transfer the atoms into the Z trap. In principle we could relax the trap, but then the trap is too shallow to hold the atoms against gravity.

We optimize the loading by improving the spatial overlap. We move the Molasses by slightly unbalanced light intensities in the laser beams (see section 4.3.3). The trade off here is, that we buy the position improvement with a less good Molasses phase and therefore slightly higher temperatures. The intensities in the counter propagating beam pairs are controlled via a $\lambda/2$ wave plate and a polarizing beam splitter. Here a turn of one degree results in an intensity change of 15% (we tilt the $\lambda/2$ wave plate on a sub degree scale). Under normal conditions we are able to load $\sim 10^8$ atoms at a temperature of $\sim 200 \mu K$ in the initial trap.

Figure 4.31 shows a series of the complete loading cycle, starting with the Q-mirror MOT.

4.3.5 Obtaining a Bose-Einstein condensate

The basic condition for obtaining a Bose-Einstein condensate is to have a phase-space density of $n\lambda_{dB}^3 \simeq 2.612$ (see section 1.2). When this value is reached condensation sets in. To get to this point with our apparatus, we have to have a large number of trapped atoms, a long life time and a high elastic collision rate in order to have good evaporative cooling. As mentioned above in section 4.3.4, we can trap $\sim 10^8$ atoms in our initial magnetic trap. A high collision rate for fast rethermalization is obtained by compressing the

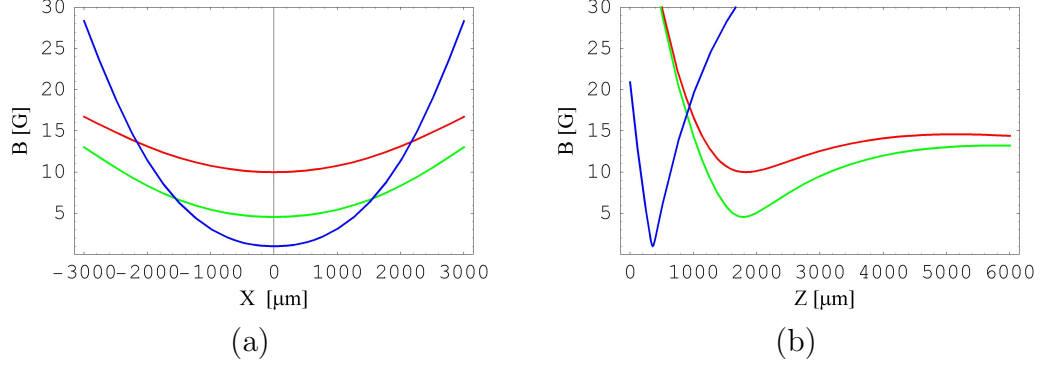


Figure 4.32: Z magnetic trap: time evolution of the trapping potentials. a) shows the potential in the longitudinal direction, b) in the radial direction. The dotted line is the starting trap ($I_Z = 50$ A, $B_Y = 25$ G), the dashed line is after the first compression stage ($I_Z = 50$ A, $B_Y = 25$ G, $B_X = 5.5$ G) and the solid line is the final trap where we condense the atoms ($I_Z = 50$ A, $B_Y = 58$ G, $B_X = 5.5$ G).

trap. The used setup is especially able, due to the nature of the wire traps, to provide such high field gradients and as a consequence a high compression.

Life time, heating and adiabatic compression

The initial Z trap has trap frequencies of $\omega_Y = 2\pi 55$ Hz and $\omega_X = 2\pi 15.2$ Hz ($I_Z = 50$ A, $B_Y = 25$ G). The trap floor is at $B_{IP} = 8$ G, and the achieved field gradient is 75 G/cm. The elastic collision rate in the beginning is one per second. As mentioned, the life time is an important property of a magnetic trap, because it determines how fast one has to cool and how long a Bose-Einstein condensate can be held in the trap. The biggest loss rate at densities lower than $10^{13}/\text{cm}^3$ are collisions with the background gas. The pressure in the science chamber is $< 10^{-11}$ mbar, and therefore long life times can be expected.

To increase the elastic collision rate we ramp up the gradient by ramping up the Y-bias field. In conventional traps this is done on a second time scale. In our case we can not compress the trap, and then start the evaporation, because the compression moves the cloud, which is initially 1.4 mm away from the chip surface, closer to the surface ($\sim 300 - 600 \mu\text{m}$ for the final values of the compression). At these distances, atom losses due to a contact with the chip surface reduce the atom number in the Z trap. Figure 4.32 shows the different trapping potentials used in the experiment.

The final trap, with trap frequencies of $\omega_Y = 2\pi 750$ Hz and $\omega_X = 2\pi 21.8$ Hz and a gradient of 430 G/cm shows the problem. The minimum

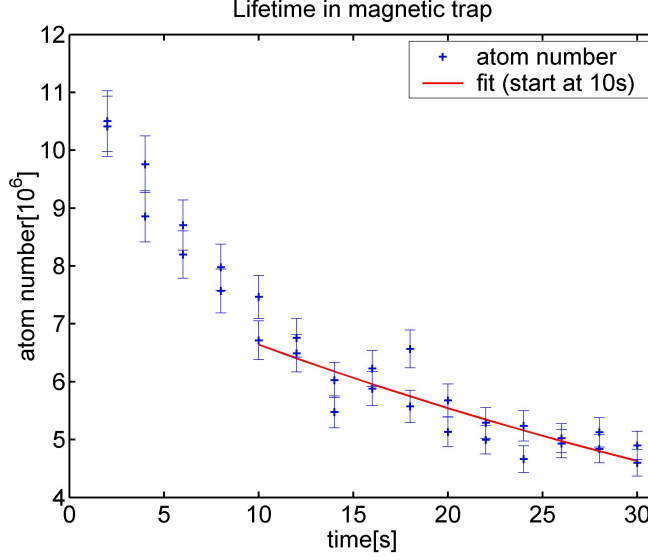


Figure 4.33: Life time of the magnetic trap: the atoms are loaded into the Z magnetic trap and the number of atoms is measured at different trap times. The fast decay in the beginning is due to an atom loss to the surface. This is confirmed by the fact, that the temperature decreases (the hot atoms are lost to the surface). The trap properties are: $I_Z = 43.7$ A, $B_Y = 43$ G. The trap frequencies are $\omega_Y = 2\pi 162$ Hz and $\omega_X = 2\pi 20$ Hz, the distance was 600 μm .

is ~ 300 μm away from the chip surface and the magnetic barrier is just ~ 15 G high, which allows hot atoms to overcome the potential wall and hit the surface. In the experiment we therefore compress the trap linearly over 19 s and simultaneously perform evaporation cooling (see next paragraph). With this approach we can avoid surface losses and still maintain good trapping conditions. Figure 4.33 shows the lifetime of our magnetic trap (no evaporation is applied).

First the atoms were loaded into the initial Z trap then the trap is compressed. The final trap frequencies are $\omega_Y = 2\pi 162$ Hz and $\omega_X = 2\pi 20$ Hz at a distance to the chip of 600 μm (the current was $I_Z = 43.7$ A and the Y-bias field was $B_y = 43$ G). The temperature in the initial trap was 250 μK . In the first ~ 10 s we observe a strong loss. The temperature after ~ 10 s was 140 μK . This indicates that we lost the hottest atoms onto the surface of the atom chip. The decay after ~ 10 s represents the real life time. When an exponential decay ($e^{-t/\tau}$) is fitted to these data points, we find $\tau=55$ s, which is adequate for the experiment.

Further on we determined the heating rate in the magnetic trap. We

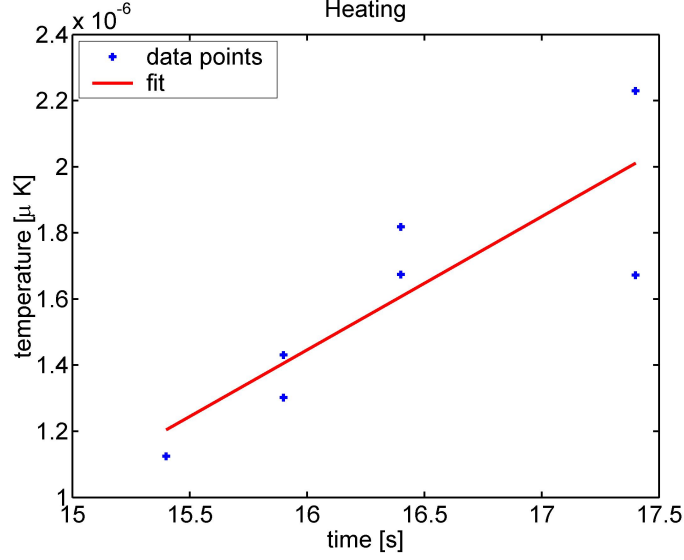


Figure 4.34: Heating in the copper Z trap: we prepare a sample of ultra cold atoms by evaporation (see section 4.3.5). Then we switch off the radio frequency and measure the temperature increase at different trap times (blue crosses). The red curve is a linear fit to the data points. We measure a heating rate of $\sim 400 \text{ nK/s}$ ($\pm 104 \text{ nK/s}$).

prepare a sample of ultra cold atoms in the range of $\sim 1 \text{ } \mu\text{K}$ by evaporating cooling (see section 4.3.5). Then we switch off the radio frequency (when we leave it on, the radio frequency would cut off the hot atoms and we would not observe a heating). We measure the temperature at different times in the magnetic trap. Figure 4.34 shows the temperature at different trapping times. The red curve is a linear fit to the rising temperatures. We get a heating rate of $\sim 400 \text{ nK/s}$ ($\pm 104 \text{ nK/s}$). This rate is low enough that we can cool against it with the evaporation technique. With evaporation we can achieve a cooling rate of $\sim 20 \text{ } \mu\text{K/s}$.

One crucial point is the adiabatic compression. Adiabatic compression means, that the atom number N and the phase-space density PSD is conserved. Assuming a power law potential of the form $U(r) \propto r^{d/\delta}$ (d is the dimension and $\delta=3/2$ for a 3 D harmonic potential), the volume of a cloud with a temperature T scales with $V \propto T^\delta$, and the elastic collision rate is

$$\Gamma_{el} = n \sigma v \propto D^{\frac{\delta-1/2}{\delta+3/2}} N^{\frac{2}{\delta+3/2}} \quad (4.25)$$

with σ the collision cross-section and v the velocity. When the trap is adiabatically compressed by a factor α , the temperature will rise by a factor of $\alpha^{2\delta/(2\delta+3)}$ and the density rises with $\alpha^{3\delta/(2\delta+3)}$. When the compression is adiabatic, the phase-space density is conserved, but the elastic collision rate will rise by a factor of $\alpha^{4\delta/(2\delta+3)}$ (all assuming that σ stays constant) [104]. A high elastic collision rate is necessary for good evaporative cooling. To achieve the adiabatic condition, changes have to be done with

$$\frac{d\omega_{trap}}{dt} \ll \omega_{trap}^2, \quad (4.26)$$

which simply means, that changes have to be sufficiently slow compared to the slowest trap frequency. This is at its best fulfilled when we ramp up the Y-bias field in 19 s.

In order to compress the trap even further, an X-bias field is added, which subtracts the original Ioffe-Pritchard field (see section 3.2.2) and further compresses the trap (see figure 4.32, dashed line). The field is ramped up in 100 ms, which fulfils the adiabatic condition. The different traps (figure 4.32) are all reached under the adiabatic condition.

Evaporative cooling

The cooling technique we use in our Z trap is the evaporative cooling, outlined in section 3.3. As mentioned, we linearly compress the magnetic Z trap. Simultaneously we shine in a radio frequency. The frequency generator³⁴ is programmed with an arbitrary frequency ramp via an GBIP connection. This allows us to optimize the cut-off parameter η to get optimal cooling. The radio frequency is amplified³⁵ and then coupled out with an antenna, which is impedance matched, i.e. its emission profile is flat throughout the used frequency. In general we start at a frequency of 18 MHz and end at ~ 500 kHz (depending on the trap floor B_{IP}).

The first indication, that the radio frequency has an effect on the atoms, is an atom loss. Measuring the temperature confirms then if the evaporation process really reduces the temperature. Figure 4.35 shows the evolution of the atom number and temperature during the 19 s evaporation cycle.

From these two quantities we can derive the atomic density (we know from the temperature measurements the Gaussian widths) and the phase space density ($n\lambda_{dB}^3$, where n is the density and λ_{dB} is the de Broglie wave length).

³⁴Stanford Research Systems, DS345

³⁵Minicircuits, ZHL-32A, 0.05-130MHz, gain 25 dB

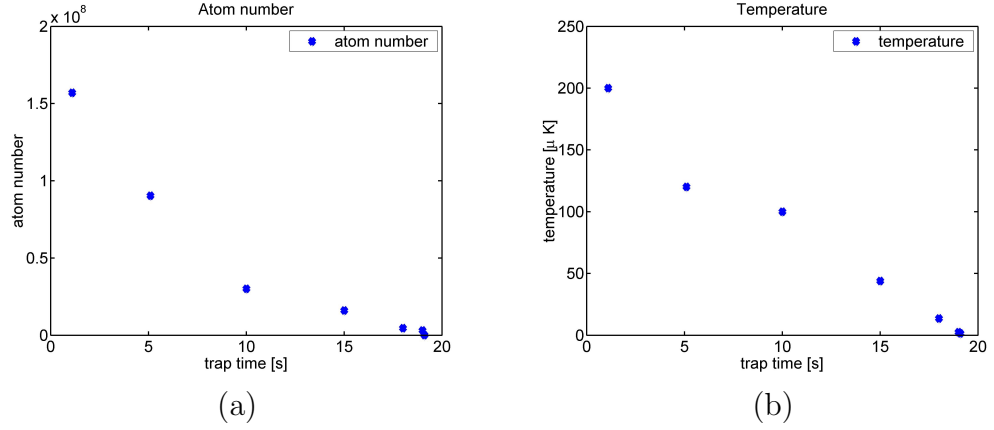


Figure 4.35: Time evolution of the atom number and temperature: the radio frequency starts at 18 MHz and is ramped down in 10 s to 6 MHz and from there in another 10 s to its final value of 539 kHz. The atom number a) as well as the temperature b) drops.

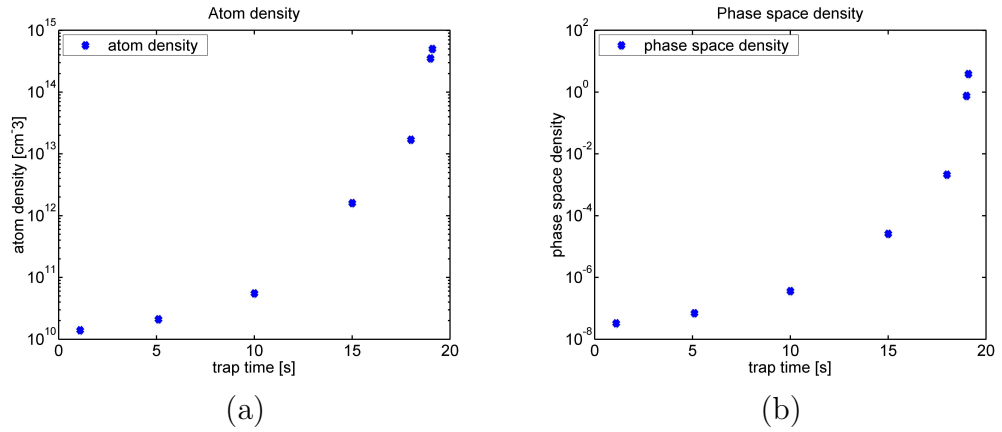


Figure 4.36: The density a) increases during evaporation. Maybe the most important quantity, the phase space density b) increases as well. From the theory we know, that condensation sets in at $n\lambda_{dB}^3 \approx 1$.

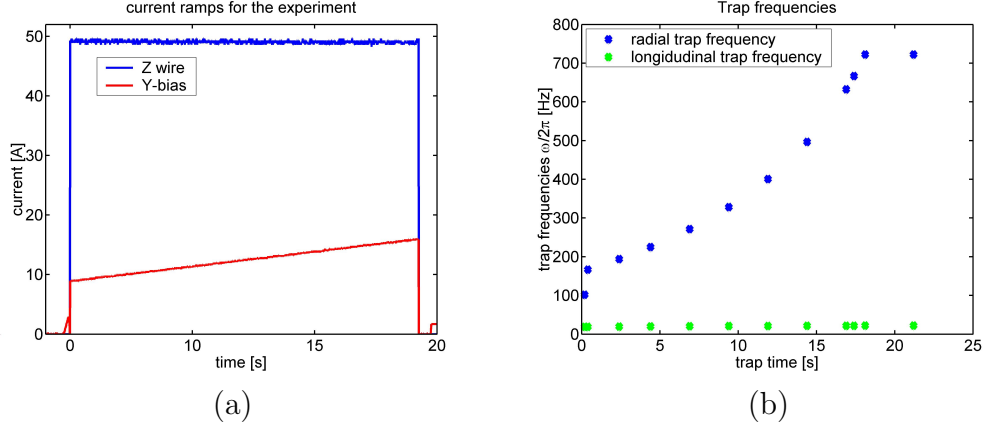


Figure 4.37: Trap development over time: a) Current ramps for the magnetic Z trap: the current in the Z wire (blue) stays constant (except of a drop of 300 mA due to heating). The current in the Y-bias coil (red) is ramped up over the experimental cycle. The final values are $I_Z=50$ A and $I_{Y-bias}=16.1$ A. Note here that the Y-bias field is also ramped up for the U-mirror MOT. The switching off between the U-mirror MOT and the Z magnetic trap can not be seen here. b) shows the trap frequencies over time.

The evolution of the trap frequencies can be seen in figure 4.37. From figure 4.35 one can see, that in the first 10 s the phase space density stays almost constant. The reason for this is that the trap is not stiff enough for good evaporative cooling. This problem cannot be overcome in this setup, because a faster compression would lead, as mentioned, to a too big loss of atoms to the surface. Nevertheless with the used setup it is possible to reach good cooling rates in the order of $\sim 20 \mu\text{K/s}$ for later times.

Bose-Einstein condensation

To achieve a Bose-Einstein condensate, we further reduce the radio frequency and compress the trap by ramping up the Y-bias field. Subtracting the Ioffe-Pritchard field (B_{IP}) with the X-bias field is essential in this phase. In this case, as the B_{IP} is reduced, the trap gets sensitive to field fluctuations, as the trap floor can be overcompensated and a magnetic zero can occur. If this is the case, we observed atom losses due to Majorana spin flips [63] (see equation 3.22).

A typical current ramp (measured with the current probe in the switches) is shown in figure 4.37. With this configuration we obtain the trapping potentials shown in figure 4.32 .

We monitor the state, in which the atoms are, by letting the sample expand, because the high optical density ($D \sim 100$) would disturb the obtained pictures. When we let the atomic sample expand, we reduce the optical density and in addition avoid a Zeeman shift due to the B_{IP} field.

For the switching of the trap the adiabatic condition 4.26 has to be fulfilled. This means, we have to switch off the trap faster than the fastest trap frequency, in our case this would mean that we have to switch faster than $\sim 100 \mu s$, which is fulfilled in our setup.

As mentioned in section 1.5.1, the clear signature of a condensate is its unique expansion characteristic. The Z magnetic trap is switched off, and absorption picture are taken after some expansion time. The image laser is at resonance ($\delta=0$, light at the $F = 2 \rightarrow F' = 3$ transition) and has an intensity of $I/I_S \approx 0.1$. Figure 4.38 shows a typical picture series for three different final radio frequencies.

The first line in figure 4.38 shows the usual thermal cloud pictures (radio frequency is at 800 kHz), as we would obtain it by measuring the temperature. For the second line we lowered the radio frequency to 650 kHz. A sharp density peak in the middle of a thermal cloud is already visible - condensation sets in. By further reducing the radio frequency to 630 kHz we obtain an almost pure condensate. The series shows the unique expansion behavior of the Bose-Einstein condensate. Not only that the cloud size stays approximately the same, but the aspect ratio is inverted as expected from theory [40]. This gives us the clear indication that we produced a macroscopic, coherent matter wave - a Bose-Einstein condensate.

To characterize the main aspects of a Bose-Einstein condensate, we have to interpret the pictures in the right way. When condensation sets in, there will be a bimodal structure of the cloud. One part of the atoms is already condensed, the others will be still thermal. From this thermal cloud around the condensate we can derive important quantities.

In section 4.2.2 we discussed the absorption method. From the spatial distribution of the optical density (equation 4.13), we get the two dimensional column density

$$\tilde{n}(y, x) = \frac{D}{\sigma_{abs}(I, \delta)}, \quad (4.27)$$

where D is the optical density (obtained from the pictures 4.21), and $\sigma_{abs}(I, \delta)$ is the scattering cross section. In section 4.2.3 we made the assumption, that for hot atoms we can assume a Gaussian spatial distribution. For low temperatures we have to use the quantum statistics, which gives

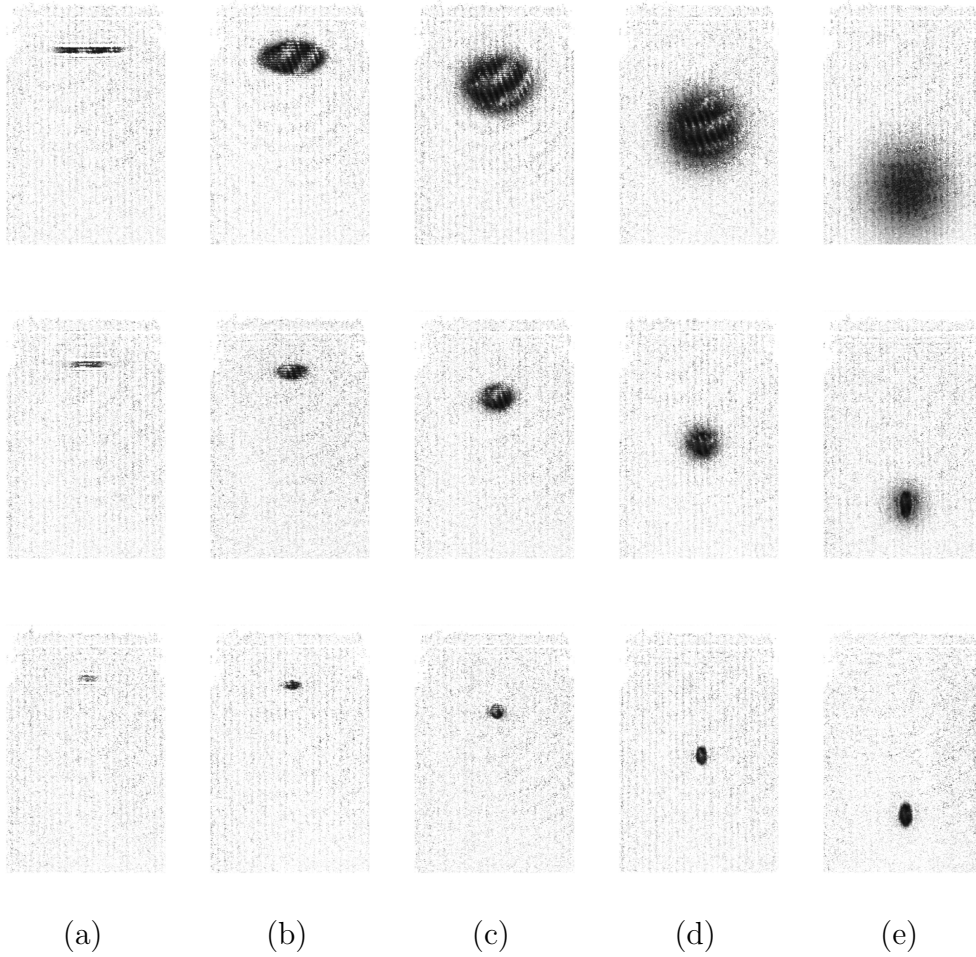


Figure 4.38: Expansion series: the atoms are trapped in the magnetic Z trap for 19 s (with evaporation). Then they are released. The first line shows the expansion of still thermal atoms (radio frequency is at 800 kHz, $T \sim 5 \mu\text{K}$). For the second line the radio frequency was lowered to 650 kHz. Some of the atoms are already in the condensed state. The third line, the radio frequency is now at 630 kHz, show a almost pure Bose-Einstein condensate. The trap parameters were: $\omega_Y = 2\pi 587 \text{ Hz}$, $\omega_X = 2\pi 68 \text{ Hz}$. The expansion times were 0, 4, 8, 12 and 16 ms (a), b) c), d) e)).

$$n_{th}(y, x) = \frac{n_{th}(0, 0)}{g_{3/2}(\tilde{z})} g_{3/2} \left(\tilde{z} \cdot \exp \left(-\frac{y^2}{y_0^2} - \frac{z^2}{z_0^2} \right) \right), \quad (4.28)$$

where $\tilde{z} = \exp(\mu/k_B T)$ is the fugacity. For high temperature, $g_{3/2}(x)$ goes as its argument x , and the distribution is purely Gaussian (as we assumed in section 4.2.3). For low temperature the behavior is different. The density near the center will be higher by a factor of $g_{3/2}(x)/x$. For temperatures lower than the critical temperature T_C , \tilde{z} can be set to 1. From the width of the cloud the temperature can be obtained [104]

$$T = \frac{m}{2k_B} \left(\frac{\omega_Y^2}{1 + \omega_Y^2 t} \right) y_0^2(t), \quad (4.29)$$

where ω_Y is the trap frequency and t the expansion time. Note here, that in this regime we can deduce the temperature from a single picture (this is quite convenient in comparison to section 4.2.3). With the temperature we can derive the chemical potential of the atoms ($T > T_C$)

$$\mu = k_B T \ln(\tilde{z}). \quad (4.30)$$

Up to now we discussed the thermal fraction in the assumption that the trap is harmonic. When there is a condensed fraction of atoms, the density distribution of the condensate fraction will be a inverted parabola

$$n_C(y, z) = n_C(0) \max \left(1 - \frac{y^2}{R_y^2(t)} - \frac{z^2}{R_z^2(t)}, 0 \right)^{3/2}, \quad (4.31)$$

where R is the width of the parabola [40, 108] and t is the expansion time. From the widths after the expansion, we can calculate the size of the condensate in the trap. Knowing the trap frequency and the size in the trap the chemical potential is fixed (the condensed atoms can only fill the trap up to the chemical potential), being

$$\mu = \frac{m\omega_y^2}{2} R_y^2(0) = \frac{m}{2} \left(\frac{\omega_y^2}{1 + \omega_y^2 t^2} \right) R_y^2(t), \quad (4.32)$$

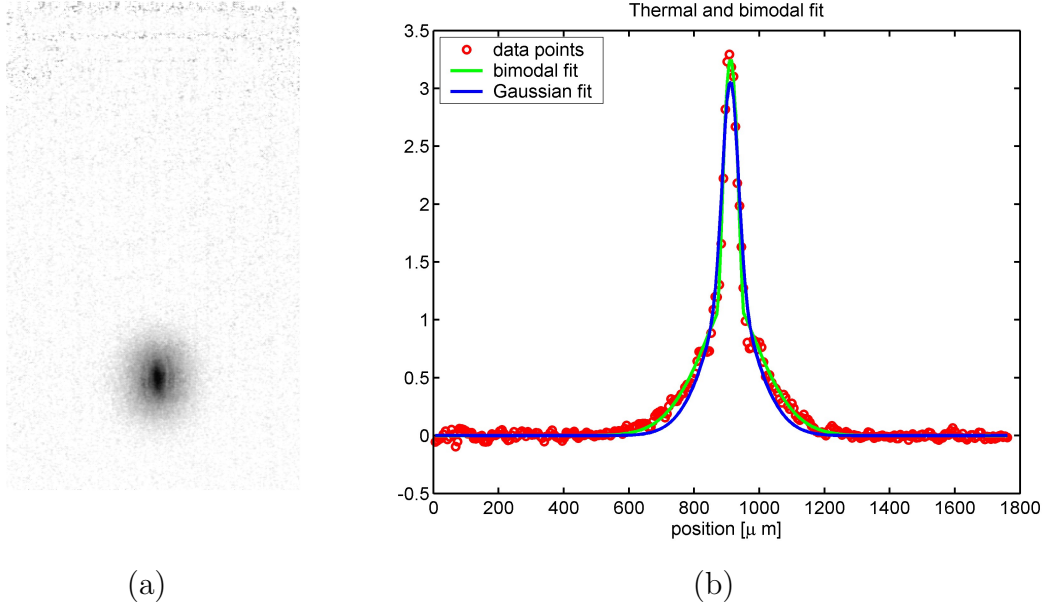


Figure 4.39: Obtaining data from the absorption picture: a) shows a partially condensed cloud (expansion time 16 msec). The trap frequencies were $\omega_Y = 2\pi 610 \text{ Hz}$ and $\omega_X = 2\pi 21.6 \text{ Hz}$. b) shows a cut in X direction through the sample. The blue curve is an ordinary Gaussian fit (equation 4.28). This fit does not satisfy the data points. Only when we employ the combined function $n_{th}(y, z) + n_C(y, z)$ (equations 4.28 and 4.31, red curve), the result is correct. Note here, that there is no finite analytical solution for $g_{3/2}$, so we approximate it with a polynome [103]

where again t is the expansion time.

The derived equations allow us now to calculate the chemical potential for the thermal and condensed fractions. The chemical potential fixes the atom number and we get the next quantity (see chapter 1)

$$N = \left(\frac{2\mu}{\hbar\omega_{ho}} \right)^{5/2} \frac{a_{ho}}{15a} , \quad a_{ho} = \sqrt{\frac{\hbar}{m\omega_i}} , \quad \omega_{ho} = (\omega_x\omega_y\omega_z)^{1/3} , \quad (4.33)$$

Figure 4.39 shows the picture of a partially condensed cloud and a cut through it. From the picture one can see clearly the condensed fraction and the thermal wings around it. The fit shows the bimodal structure of the sample. Here we see that we have to fit $n_{th}(y, z) + n_C(y, z)$ to the distribution to obtain all possible information from it.

We can now study the condensation process itself, and determine the relevant quantities. Figure 4.40 shows how the temperature drops when the radio frequency is lowered relative to the trap bottom B_{IP} . The number in the Bose-Einstein condensate rises. Figure 4.40 is a more detailed continuation of figure 4.35. Figure 4.41 a) shows how the peak density rises when there are condensed atoms. Figure 4.41 b) shows the phase transition to the Bose-Einstein condensate more pronounced .

The pictures from which the data points in figure 4.40 and 4.41 were extracted, were corrected for the fact, that we do not see all atoms, because we have no guiding field for the absorption image (see equation 4.10). We set $\alpha = 7/15$ to account for the error. Furthermore, as the Bose-Einstein condensate falls during the exposure time, the pictures are slightly smeared out. For this we also have to account.

T_C can now be obtained according to the theory from chapter 1. The obtained data points in this case allow us to give a upper limit for $T_C < 1 \mu K$. The theory would give for the obtained atom number $T_C = 930 \text{ nK}$, which is in good agreement to the boundary we were able to give.

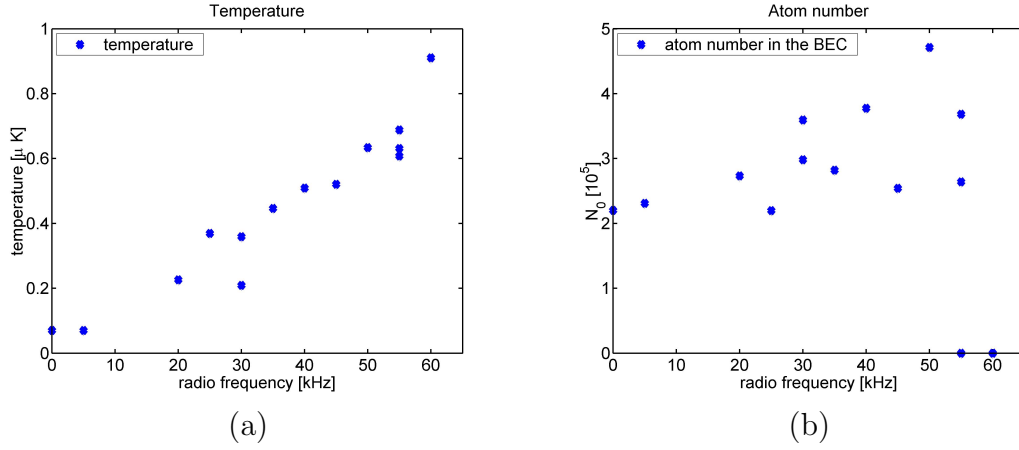


Figure 4.40: Evolution of the atomic sample when the radio frequency is lowered: when the temperature approaches the critical temperature T_C a), the number of atoms in the condensed state rises b). Note that the radio frequency is relative to the trap floor.

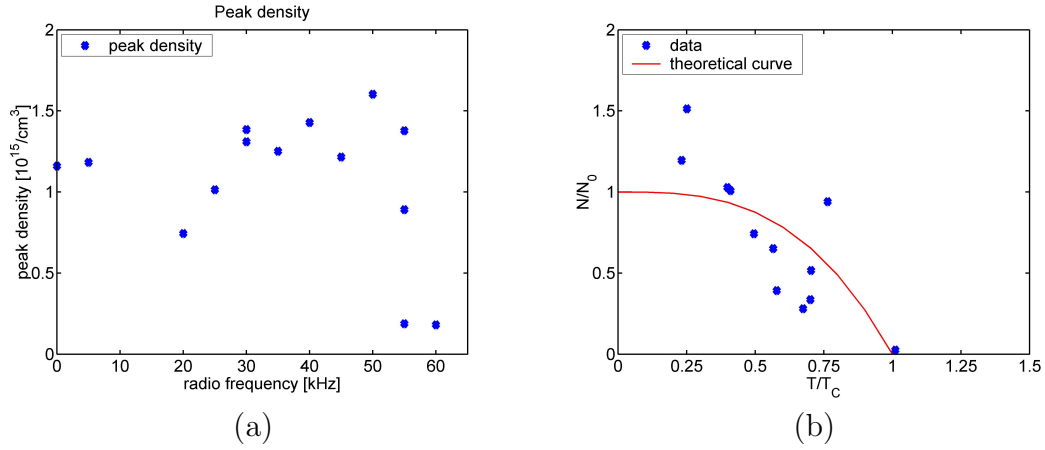


Figure 4.41: The condensation: the radio frequency is lowered, and the peak density rises a). In b), the phase transition is most pronounced. The conditions were: $\omega_Y = 2\pi 610 \text{ Hz}$ and $\omega_X = 2\pi 21.6 \text{ Hz}$. Note that the radio frequency is relative to the trap floor.

Chapter 5

First experiments

In this chapter we describe experiments performed with the Bose-Einstein condensate and ultra cold thermal clouds. As pointed out in section 1.5.1, we study the behavior of a freely expanding Bose-Einstein condensate. Furthermore, we excite collective shape oscillations by changing the trap from a starting trap, where we create the Bose-Einstein condensate, to a final trap (see section 1.5.2). The collective shape oscillations can be studied by holding the Bose-Einstein condensate for adjustable times in the final trap, and then measuring the widths of the expanding sample. When we compute the aspect ratio (for a certain expansion time), we are able to calculate from the oscillating aspect ratio the longitudinal trap frequency to a high accuracy (see solution of equation 1.57 for the regime of $\epsilon \ll 1$). The study of these collective shape oscillations is of special importance, because they reveal that a Bose-Einstein condensate, which is for example guided in a perturbed potential, will be excited to these oscillations. A perturbed potential can be easily generated, when wires are connected to the guide wire, as we discussed in section 3.2.3. Due to the nature of our wire traps, we can excite shape oscillations and center of mass motion in the radial direction simultaneously. Note here that the shape oscillations depend on the longitudinal trap frequency, while the center of mass motion is carried out in the radial direction. The collective shape oscillation of the Bose-Einstein condensate and the center of mass motion can be monitored at the same time, and thus allows us to measure both trap frequencies at the same time.

Further on we study the transport of a cold thermal cloud from the used copper structure to the atom chip (a Z shaped wire on the atom chip is used for the magnetic trap). Heating rates and atom losses during the transport are studied, as well as trap lifetime and heating in the final atom chip trap. The chapter is closed with a demonstration of a coil free magnetic trap. The Z shaped wire for the trap is on the atom chip, while the bias field is

generated by the copper structure behind it.

5.1 Free expansion and collective shape oscillations

As we saw in section 4.3.5 and figure 4.38, the expansion characteristic of a Bose-Einstein condensate is unique and different from the expansion behavior of a thermal cloud.

To let a Bose-Einstein condensate freely expand, meaning that we switch off the magnetic trap, we have to fulfill the adiabaticity condition

$$\frac{d\omega}{dt} \ll \omega_{trap,max}^2, \quad (5.1)$$

which we do with our switching times of $< 50 \mu s$. We first generate a Bose-Einstein condensate in the copper Z trap with the method described in section 4.3.5. Then it is released from the trap and we take absorption pictures at different expansion times. A bimodal function is fitted to the expanding cloud, to account for the thermal and for the condensed fractions of the sample (see section 4.2.5). Figure 5.1 shows the aspect ratios of the widths of the inverted parabola obtained from the fits at different expansion times [109]. Note here that the theoretical curve is not a fit, we just used the trap frequencies, which we calculate using the model introduced in section 3.2. These trap frequencies are then inserted in equation 1.55. The widths were corrected with a constant factor, which accounts for the smearing of the cloud due to the long exposure time of the images (the fitted widths appear bigger due to the falling cloud while the picture is taken).

The presented theory in sections 1.5.1 and 1.5.2 can also be applied to time dependent traps, in such a sense, that the confining potential is changed from an initial trap to a final trap (still being adiabatic). For this experiment we first prepare the Bose-Einstein condensate in a well defined trap, the initial trap (the red curves in figure 5.2). Then we ramp down the X-bias field in 25 ms, which relaxes the trap (the green curves in figure 5.2). This trap is called the final trap. The relaxation causes a collective shape oscillation of the Bose-Einstein condensate in the final magnetic trap, meaning that the cloud changes its size with time (later we will see, that in addition we also excite a center of mass motion in the radial direction). This oscillation is governed by equation 1.45 for the regime of $\epsilon \ll 1$ and small perturbations. The ensemble is kept in the final trap for a variable holding

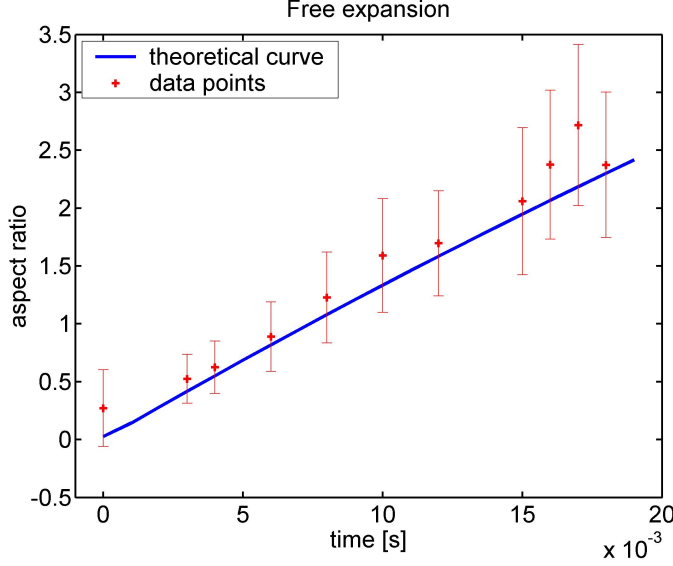


Figure 5.1: Free expansion of a Bose-Einstein condensate: the data points are the aspect ratio of cuts in X and Z direction through the cloud. The estimated error for the fits is $10 \mu\text{m}$. The blue curve is the theoretical prediction for the aspect ratio for a trap of: $\omega_Y = 2\pi 827.1 \text{ Hz}$ and $\omega_X = 2\pi 22.5 \text{ Hz}$.

time, and then it is released. Figure 5.3 shows the expansion characteristic of a Bose-Einstein condensate, which is oscillating in contrast to a condensate at rest (for this we did not ramp down the X-bias field, but switched off the trap instantaneously). From figure 5.3 it is already clear, that the Bose-Einstein condensate, which performs the collective shape oscillation, expands differently. This different expansion is due to the conversion of potential energy of the starting trap into kinetic energy. This kinetic energy changes the momentum distribution, and this change causes the different expansion behavior.

As we discussed in section 1.5.2, it is possible to deduce the longitudinal trap frequency from the expansion behavior [110, 111]. We measure this longitudinal trap frequency by varying the holding time (1 ms steps) and taking absorption pictures after 19 ms of expansion. We compute from the bimodal fit, which we apply to the absorption pictures, the width in Y and X direction and the aspect ratio of the widths. In figure 5.4 the aspect ratio as a function of the holding time is shown. The red curve is a fit to the data points, using a sine function with a phase and a damping factor. As we found out in section 1.5.2 with the numerical model, the aspect ratio is not clearly a sine function, because of the non linear coupling (see figure 1.5).

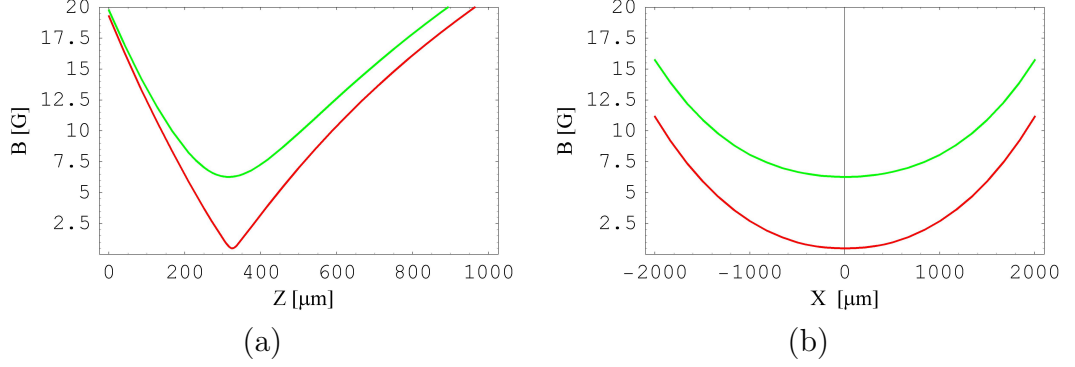


Figure 5.2: Trapping potentials: a) shows the trapping potential in radial and b) in axial directions. The red curves represent the potential, in which we create the Bose-Einstein condensate ($\omega_Y = 2\pi 827 \text{ Hz}$ and $\omega_X = 2\pi 22.5 \text{ Hz}$). The blue curve is the final potential in which the Bose-Einstein condensate oscillates ($\omega_Y = 2\pi 234.7 \text{ Hz}$ and $\omega_X = 2\pi 22.4 \text{ Hz}$).

The magenta curve in figure 5.4 shows the aspect ratio which we get from the numerical model (for 19 ms expansion). When comparing the numerical model curve (magenta, note here that the numerical curve is not a fit to the data) with the data points, there are indications, that the curve from the model (which includes a nonlinear coupling term) accounts better for the obtained data [112]. However our model does not account for a damping of the oscillation [113].

The sine function fit gives us an oscillation frequency of $\omega_{osc}^{slow} = 34.6 \text{ Hz}$. The theoretical prediction (which is the solution of equation 1.57), is $\omega_{osc}^{slow} = \sqrt{5/2}\omega_X = 35.5 \text{ Hz}$ (for small perturbations). This value is in good agreement to our measured result. In a second run, which was performed in the same way, we could confirm the good agreement.

Note here that we monitor the shape oscillation over 134 ms. Remarkable here is not only the good agreement of the shape oscillation frequency with the theoretical prediction, but also the stability of the condensation process.

One feature of our wire traps is, that when we change the X-bias field, not only the the trap floor B_{IP} is changed, but also the spatial position of the minimum is changed with respect to the chip surface (see section 3.2.2). This change is in the μm range, in our case $\sim 9 \mu\text{m}$. Figure 5.5 is a zoom in of the trapping potentials in Z direction (compare with figure 5.2a). When we change from the initial trap to the final trap, the small position change will cause the Bose-Einstein condensate to perform a center of mass motion in Z direction in the final trap [114]. We can assume that the trap is harmonic

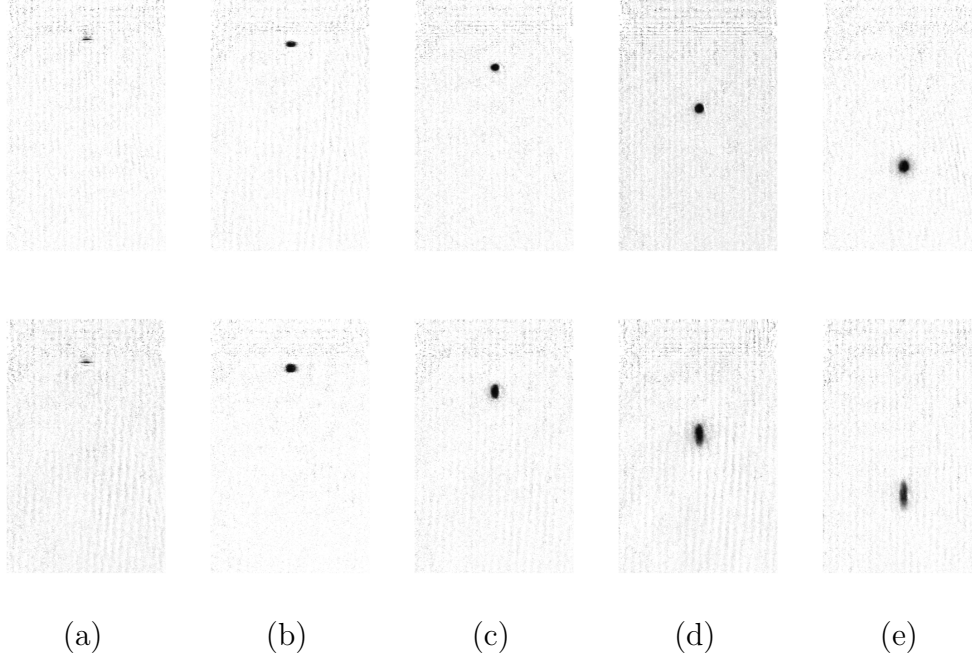


Figure 5.3: Free expansion of an oscillating Bose-Einstein condensate (upper row) and a Bose-Einstein condensate at rest (lower row) . The clear difference in the expansion behavior is visible. After 16 ms (column e)), the sample which oscillates in the magnetic trap appears round, while the non oscillating reveals the known characteristic. The trap frequencies were for the initial trap $\omega_Y = 2\pi 827 \text{ Hz}$ and $\omega_X = 2\pi 22.5 \text{ Hz}$ and for the final trap $\omega_Y = 2\pi 234.7 \text{ Hz}$ and $\omega_X = 2\pi 22.4 \text{ Hz}$. The ramp down time for the X-bias field was 25 ms. Note here that the aspect ratio of the lower row (non-oscillating) was used for figure 5.1. The expansion times were 0, 4, 8, 12 and 16 ms for a), b), c), d), e).

in this region, and therefore the sample will perform a harmonic oscillator motion. If we open the trap and take an absorption picture after some expansion time, the position of the expanded sample at the time of the image will depend on this center of mass motion and on the time we opened the trap. If the Bose-Einstein condensate is closer to the chip (due to the center of mass motion), we will detect the cloud at a different position than we would detect it when the sample is further away from the chip.

To measure this position dependence, we can use the same experimental data set cycle which we used to study the collective shape oscillations, but now plotting the position of the Bose-Einstein condensate versus the holding time (see figure 5.6a)). As sine function was applied to the data, and the

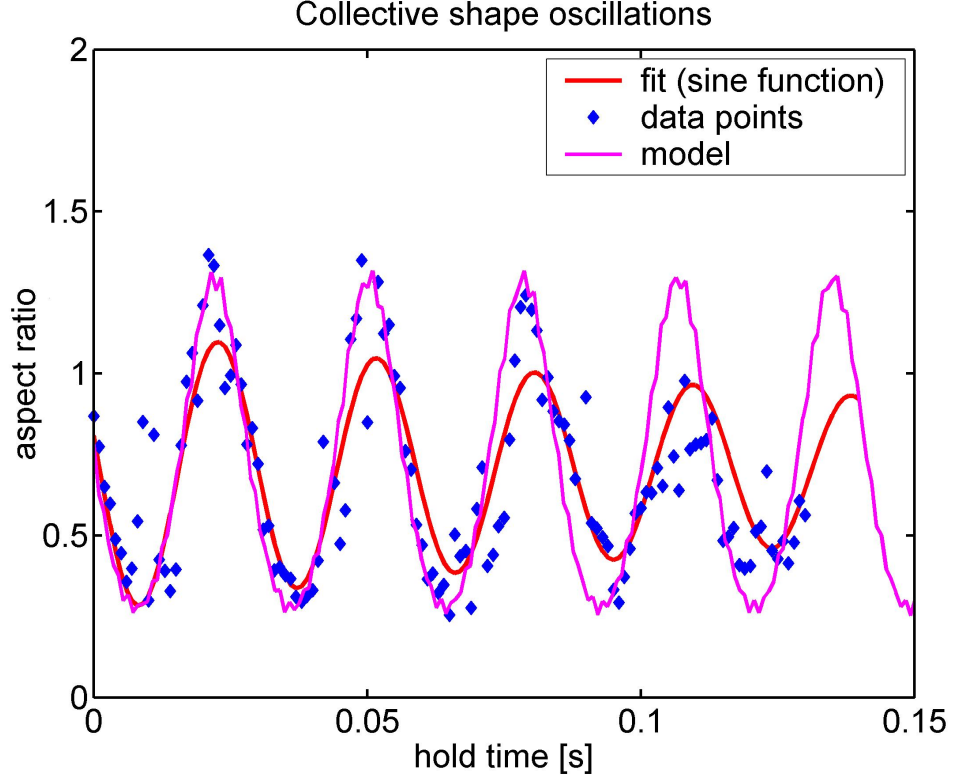


Figure 5.4: Collective shape oscillations of a Bose-Einstein condensate: the initial frequencies are $\omega_Y = 2\pi 827 \text{ Hz}$ and $\omega_X = 2\pi 22.5 \text{ Hz}$, the final trap frequencies are $\omega_Y = 2\pi 234.7 \text{ Hz}$ and $\omega_X = 2\pi 22.4 \text{ Hz}$. The ramp time is 25 ms and we let the sample expand for 19 ms. We plot the aspect ratio of the widths against the holding time. The fit (red curve) is a damped sine function. The fit gives us a oscillation frequency of $\omega_{osc}^{slow} = 34.6 \text{ Hz}$ (the theoretical prediction is $\omega_{osc}^{slow} = 35.5 \text{ Hz}$). The magenta curve is the aspect ratio, which we obtain from our model (initial and final trap frequencies are the same as for the data, the ramp down time in this case is 28 ms; note that the curve is not a fit to the data points except a phase offset).

best fit gave us a frequency of $\nu_{osc}^{position} = 219 \text{ Hz}$. We also analyzed the data using a fast Fourier transformation (see figure 5.6b)), which got a clear peak at a frequency of $\nu_{osc}^{position} = 225 \text{ Hz}$. The results differ slightly, but still they are in good agreement. The radial trap frequency of the final trap is $\omega_Y = 2\pi 234.7 \text{ Hz}$ (calculated with our Mathematica model), which is in good agreement to the measured one.

To measure the radial frequency, usually the trap is modulated with an

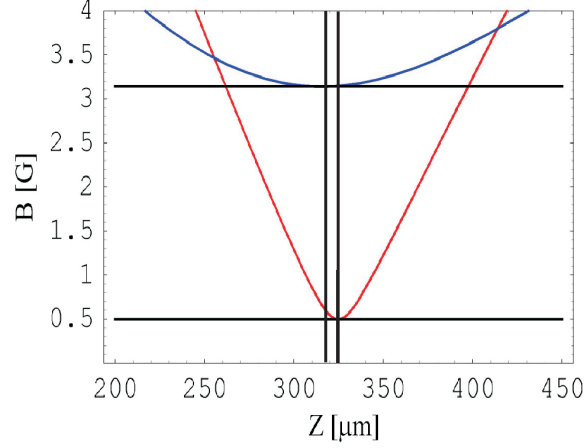


Figure 5.5: Trapping potential in radial direction (z direction): the red curve corresponds to trap frequencies of $\omega_Y = 2\pi 827 \text{ Hz}$ and $\omega_X = 2\pi 22.5 \text{ Hz}$ (the X-bias field is still on), the green curve (scaled with a factor of 0.5) corresponds to $\omega_Y = 2\pi 234.7 \text{ Hz}$ and $\omega_X = 2\pi 22.4 \text{ Hz}$ (X-bias field is switched off). The two vertical lines indicate the position of the minimum of the potentials. Due to the switch off of the X-bias field the minima shifts $9 \mu\text{m}$. This causes the Bose-Einstein condensate to perform a center of mass motion in the green potential. Note here, that the chip surface would be at $Z=0$.

appropriate frequency, and due to parametric heating (when the modulation frequency matches the trap frequency) and atom loss can be observed [109]. With our traps, a modulation is not required, and both trap frequencies can be measured in one experimental cycle from the same data set.

5.2 Basics studies of the transfer to the atom chip

One crucial point in our setup is the transfer to the atom chip. So far we used the copper H structure underneath the atom chip. The structure allows us to trap a large number of atoms, but the magnetic manipulation possibilities are little. Therefore we developed the atom chip with its more complex structures. The structures on the atom chip, and thus the magnetic manipulation possibilities, just depend on the design of the used wires on the atom chip.

In order to load the atom chip, we use a Z wire structure on the chip, similar to the copper Z structure, but smaller. The chip we use has a $2.2 \mu\text{m}$

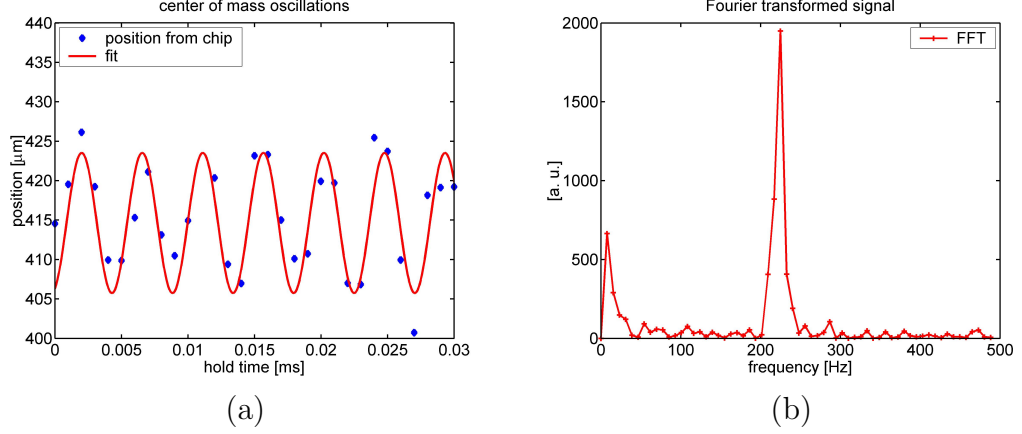


Figure 5.6: Position of the Bose-Einstein condensate: due to the position change of the trap minimum, when we change the trap frequencies from $\omega_Y = 2\pi 827 \text{ Hz}$ and $\omega_X = 2\pi 22.5 \text{ Hz}$ to $\omega_Y = 2\pi 234.7 \text{ Hz}$ and $\omega_X = 2\pi 22.4 \text{ Hz}$, we excite a center of mass motion in radial direction of the final trap. a) shows the position of the expanded sample (19 ms of expansion time), which changes due to the center of mass motion. b) is the fast Fourier transformation of the data points. A clear peak appears at a frequency of $\nu_{osc}^{position} = 225 \text{ Hz}$, which is in good agreement to the result, which we get out from our model ($\omega_Y = 2\pi 234.7 \text{ Hz}$).

gold layer, the Z structure has a 2 mm long and 200 μm wide central wire. This structure we will refer to as the gold Z. The current for the gold Z is provided by a specially designed power supply. We basically use a battery and an IGBT to regulate the current. This ensures ultra low noise currents (for the noise spectra please see Appendix E).

For the transfer we first prepared a cold atom cloud ($T \sim 5 \mu\text{K}$ and $N \sim 10^6$) in the copper Z trap by evaporative cooling (we use a similar procedure, which leads to the Bose-Einstein condensate, but we halt the radio frequency ramp at a higher value). After we prepared the desired sample, we switch off the radio frequency. The X-bias field is ramped down in 100 ms. This we have to do, because we could overcompensate the B_{IP} during the transfer or in the gold Z, which would lead to a magnetic hole in the trap and this would make Majorana spin flips possible (see equation ??). Then we ramp up the current in the gold Z in two steps, while we ramp down the Y-bias field and the current in the copper Z (also in two steps). When we do the transfer, we have to fulfill the adiabaticity condition (see equation 5.1). This motivates the transfer time of 750 ms. In figure 5.7 the current ramps for the transfer are illustrated. We measure the current through the bias field and the wire structures with Hall probes in the current circuits. From these currents

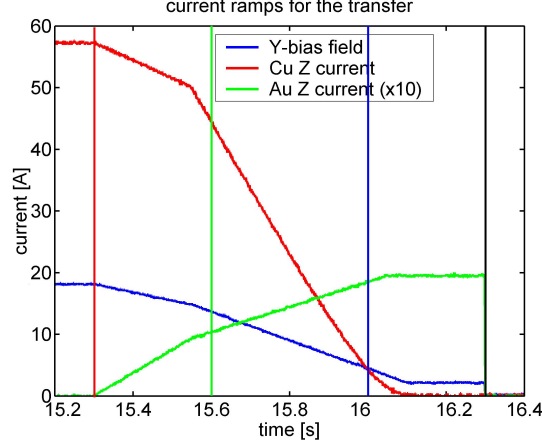


Figure 5.7: Transfer to the chip: the current through the Z copper structure (blue), the Y-bias field (red) and the gold Z (green) are plotted. The vertical lines indicate times: 15.3, 15.6, 16, 16.3s (red, green, blue, black).

we can compute the behavior of the trapping potentials. In the model we account for the shift in X direction ($\sim 150\mu\text{m}$). In figure 5.8 the trapping potentials are shown. Here again we incorporate for the complete geometry including the leads and connections to the copper structure as well as to the gold structure. Figure 5.9 shows the position change of the trap during the transfer (figure 5.9a illustrates the distance to the chip, figure 5.9b shows the movement in X direction; here the data are displayed with respect to the initial trap). The position of the cloud is measured in the trap (expansion time is 0 ms, in order to get the real trap position). Then a Gaussian fit was applied to the absorption pictures and the maximum of the cloud in longitudinal direction (X direction), as well as the distance to the atom chip was determined. In section 4.1.3 we mentioned that the atom chip is glued on top of the copper H structure. When we did this, we accidentally displaced the atom chip by $\sim 150\mu\text{m}$ with respect to the copper structure in longitudinal direction. This affects the transfer, because the trap can not be changed without moving the atoms in X direction (horizontal direction). This displacement will distort the cold cloud.

The calculated position in the longitudinal (X direction) and vertical (Z direction) direction do not match the data points (see figure 5.9a) and b)). The calculated curve reflects the general behavior of the data points, but it does not fit to a high accuracy. The reason for this can be that the chip is slightly rotated or that the measured current ramps differ from the actual current (we performed model calculations, where we used currents $\sim 10\%$

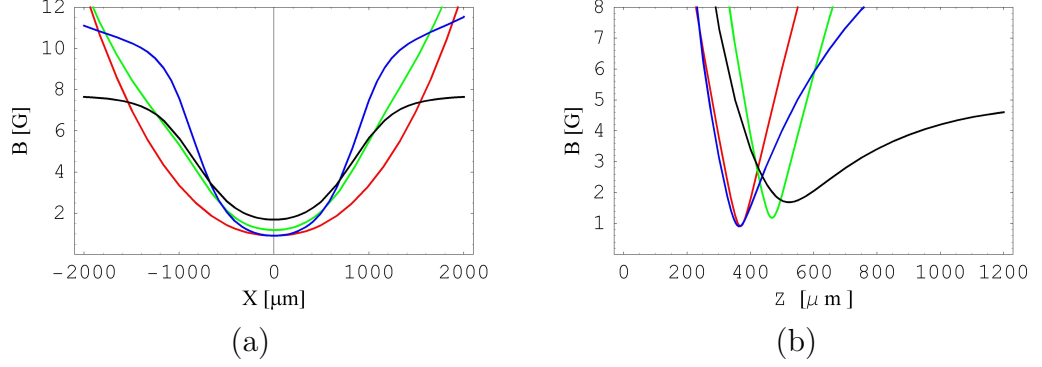


Figure 5.8: Trapping potentials during the transfer: a) shows the longitudinal b) the radial potentials. The order in time is red (15.3 s), green (15.6 s), blue (16.0 s) and black (16.3 s). We start (red) from a trap with trap frequencies of $\omega_Y = 2\pi 827$ Hz and $\omega_X = 2\pi 22.5$ Hz, and we end in a trap (black) of $\omega_Y = 2\pi 213.5$ Hz and $\omega_X = 2\pi 28.6$ Hz. The chip surface in plot b) is at position 0. Note here that in the longitudinal direction a), the trap minimum of the final trap (black) is 150 μm displaced with respect to the starting trap (red).

lower than the measured, and found a better agreement). With this transfer method, we were able to transfer the atoms to the atom chip conserving both, the initial temperature (we start with an initial temperature of ~ 5 μK) and the number of atoms (start is 10^6 atoms).

Note here, that before we studied the transfer in detail, we tried successfully a transfer of a Bose-Einstein condensate to the atom chip (see figure 5.10). We found, that we loose an order of magnitude in the atom number (we ended up with 3×10^4 atoms), and the condensate was excited [71]. The used ramps were single step ramps, and during the transfer we kept the radio frequency on (we adjusted the radio frequency according to the trap floor), in order to shield the Bose-Einstein condensate from the thermal atoms. However this transfer was not satisfying, because of the atom loss and the distortion of the condensate.

Another important property, as pointed out already in section 4.3.5 and displayed in figure 4.33, is the lifetime of the atoms in the magnetic trap. It gives the time scale on which atoms can be further cooled or manipulated. Figure 5.11a) shows the number of atoms for different holding times in the gold Z after the transfer (the atom number was determined from pictures, which were taken after 3 ms of expansion; compare to section 4.3.5). We fit an exponential decay to the data points using the function $e^{-t/\tau}$. We find a lifetime of $\tau \sim 13$ s, which is small compared to the lifetime of the copper

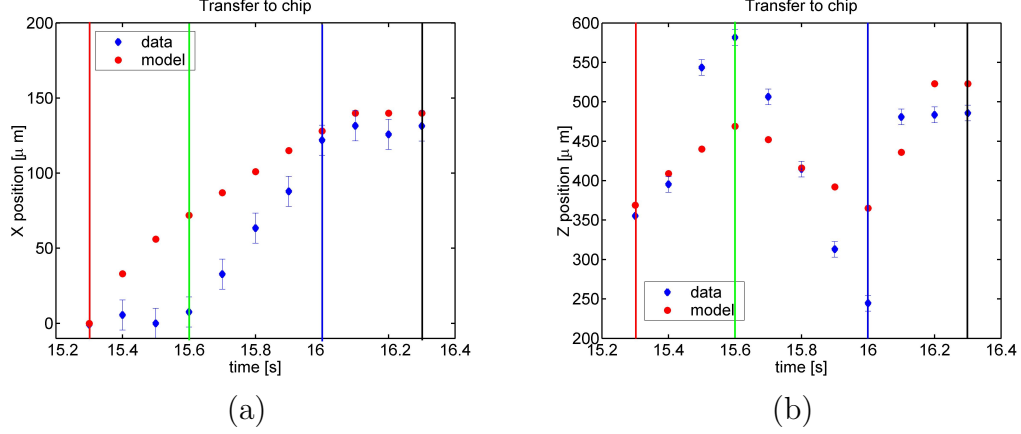


Figure 5.9: Position measurement during the transfer: we ramp up the current in the gold Z in two steps, and subsequently we ramp down the current for the copper Z and the bias field (see figure 5.7). Blue are the data points and red are positions calculated with our model using the applied current ramps. a) shows how the atoms move in X direction due to the displacement of the atom chip with respect to the copper structure (note here, that the points are calibrated to the starting position). b) shows how the atoms change their position in radial direction (distance from the atom chip surface). The vertical lines correspond to 15.3 s (red), 15.6 s (green), 16 s (blue) and 16.3 s (black).

Z (here we find a value of ~ 55 s). In the case of the gold Z we can exclude a surface effect, because we do not see a decrease of the temperature, and we measured the life time with a cold atom cloud ($\sim 5 \mu\text{K}$). In addition the distance to the chip is $\sim 450 \mu\text{m}$. We can also exclude current noise, because we developed special car battery driven power supplies to minimize the noise (see Appendix E for the noise spectra of the power supplies). A possible reason for the short life time can be, that we destroy locally the vacuum. This can be caused by the current, which we run through the gold Z, which heats the structure and some residual dirt may evaporate.

We also performed heating measurements, which are illustrated in figure 5.11b). The data were recorded in one go, together with the lifetime measurement (see figure 5.11a)¹. The measured heating rate is $\sim 500 \text{ nK/s}$, which appears large, but it is still in the range where experiments are possible.

¹The error bars correspond to the standard deviation from the fitted mean value. Note that this is the total error connected to the atom number, i.e. the error due to experimental fluctuations and errors during detection and processing.

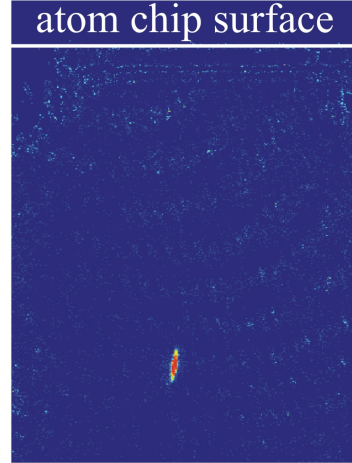


Figure 5.10: Bose-Einstein condensate in the atom chip: we transferred the condensate from the copper Z structure to the gold Z with single step ramps (for the current in the copper Z, gold Z and the Y-bias field). During the transport we lost an order of magnitude in atom number ($N \sim 3 \cdot 10^4$). The picture was taken after 16 ms of expansion.

5.3 Two wire trap

In section 3.2 we discussed how we can generate magnetic micro traps with wires and bias fields. The bias fields in the experimental realization so far, were generated by external coils (see section 4.3.1). But this restriction to external coils is not necessary. It turns out that for some applications, a single straight wire is the much better choice. One example would be a wire, which is not straight, but makes a 90° turn. If one wants to use such a structure for a side guide, a constant bias field would not be sufficient (see section 3.2.1). In such a case the bias field must rotate with the bending wire in order to have a side guide all along the wire. Here we will to discuss a case, where we used the bias field of a wire to generate a three dimensional magnetic trap on the atom chip. We used the already discussed Z geometry on the atom chip (see section 5.2) for the wire. The bias field is generated by the copper structure (see section 4.1.3 for the copper structure and figure 4.11). In order to get a magnetic minimum, when using two wires, the current in the central wires must be counter propagating. The three dimensional confinement is done by the leads of the gold Z and the leads of the copper Z, since these currents propagate in the same direction. Figure 5.13 shows an explosion drawing

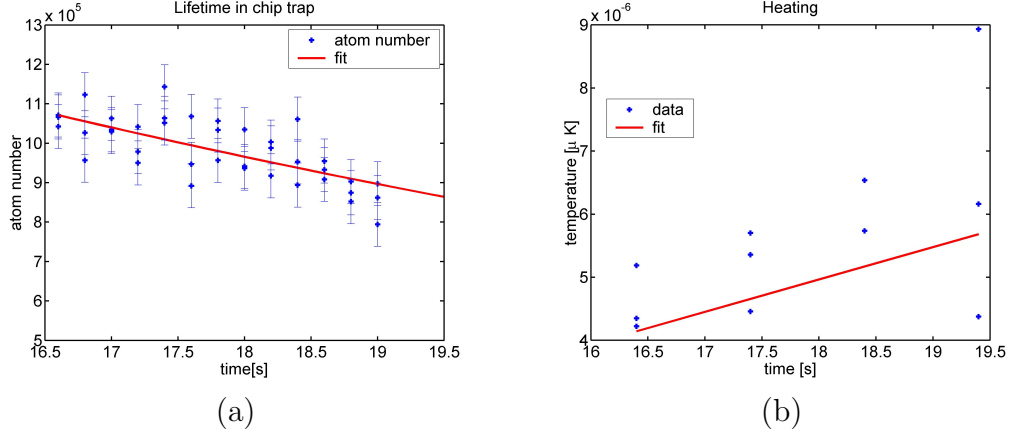


Figure 5.11: Lifetime (figure a)) and heating rate (figure b)) in the gold Z: a) we keep the atoms in the magnetic trap for different times and take absorption pictures after 3 ms of expansion. The atoms are initially $\sim 5 \mu\text{K}$ cold. From the fit (exponential decay $e^{-t/\tau}$), we get a life time of $\tau \sim 13$ s. b) Heating rate in the gold Z: we prepare an atomic cloud of $\sim 5 \mu\text{K}$ and monitor how the atoms heat up with time. No radio frequency is applied to the sample, because it would mask heating. We measure a heating rate of $\sim 513 \text{ nK/s}$ ($\pm 170 \text{ nK/s}$). Note here that the heating rate can only be an upper estimate.

of the atom chip holder. The green and red lines indicate the current path, the arrows the direction. As one can see, for this experiment the most outer ports of the copper H structure are connected. These ports are 12.75 mm apart (see Appendix C for the technical drawing). The trapping potentials generated in this way do not differ strongly from the one which we used so far. In figure 5.14 the longitudinal and radial trapping potentials are shown. The depth of the trapping potential is just $350 \mu\text{K}$, which puts a restriction on the temperature of the atoms in the trap. When we load the two wire trap, we pre cool the atoms by evaporation in the small copper Z trap, as we discussed in section 4.3.5. Then we transfer the atoms to the atom chip, as discussed in section 5.2. Subsequently we ramp up the current in the large copper Z while the Y-bias field is reduced to zero. The field generated by the copper wire replaces the Y-Bias field and establishes a magnetic trap with the gold Z. Note that there is no further bias field used. This is a major step towards further miniaturization of Bose-Einstein condensation setups, i.e. for mobile applications. With such a procedure we were able to load the two wire trap with 10^6 atoms at a temperature of $T=20\mu\text{K}$. Figure 5.12 shows an absorption picture after 3 ms of expansion. The structures to the left of the picture are the bonding wires to the atom chip structures. As

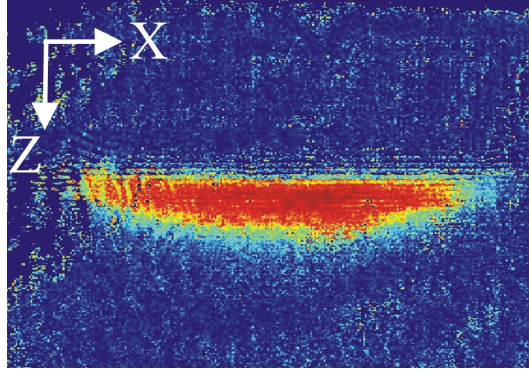


Figure 5.12: Two wire trap: the figure shows a two wire trap. The trap frequencies were $\omega_Y = 2\pi 298.1 \text{ Hz}$ and $\omega_X = 2\pi 28.1 \text{ Hz}$ (distance to chip $Z=359 \text{ }\mu\text{m}$). The distortions to the left of the picture are shadows of the bonding.

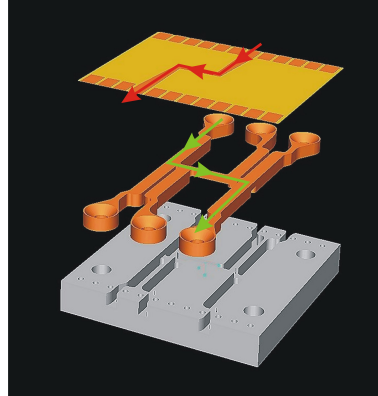


Figure 5.13: The technical drawing shows the atom chip holder and the atom chip on top (with a symbolic Z structure). The current in the different wires is counter propagating in order to form a trapping potential (see figure 5.14). The distance of the center of the copper structure to the chip surface is 1.2 mm.

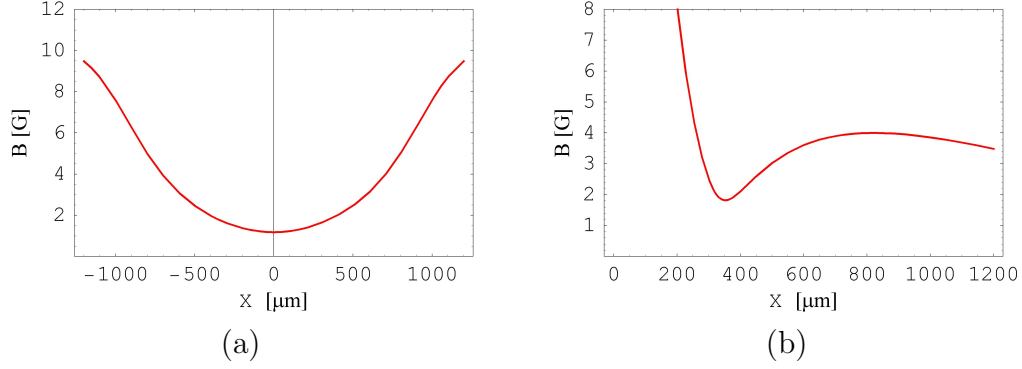


Figure 5.14: Trapping potentials generated using a wire for the bias field: we run a current of 8.4 A through the copper structure, and 2 A through the gold Z (see figure 5.13). With this configuration we get trap frequencies of $\omega_Y = 2\pi 298.1$ Hz and $\omega_X = 2\pi 28.1$ Hz at a distance of $Z=359$ μm .

the cloud shifts due to the displacement in X direction of the atom chip (see figure 5.9b)), the bonding wires become more visible.

Chapter 6

Summary and outlook

With the first realization of trapping thermal atoms using magnetic wire traps, a new and promising field in ultra cold atom physics was opened. The simple generation of complex trapping potentials is striking, as it was up to this point not possible to realize such potentials.

The realized potentials opened a new path to manipulate atoms. For most experiments a coherent matter wave, a Bose-Einstein condensate, is needed. Therefore the development of magnetic wire traps to generate trapping potentials in which Bose-Einstein condensation is possible was pursued by several groups.

In the presented work, we developed an experiment, which combines 'macroscopic' wire structures with microscopic wires. The reason for this approach is, that in general the trapping volume and the trap depth of microscopic wire traps is small. This would put restrictions on the atom number and temperature of the atomic sample.

With the development of a 'macroscopic' copper structure, we were able to overcome these restrictions. The copper structure consists of a combination of differently sized Z- and U-shaped wires. The U wires in conjunction with a bias field generate quadrupole fields, suitable to operate a magneto optical trap. The combination of Z wires and bias fields form Ioffe-Pritchard type traps, with a non zero magnetic minimum. In such a trap, Bose-Einstein condensation was realized. To have the richness in physics that the microscopic wire structures offer, we mounted the atom chip on top of this 'macroscopic' copper structure. For the atom chip itself we employed fabrication techniques known from the semiconductor industry. These methods enabled us to fabricate wire sizes down to the μm region.

In order to get to the point of loading the initial magnetic trap generated by the copper structure with a large number of atoms (10^8) at a reasonable temperature ($T \sim 200\mu\text{K}$), we developed an experimental cycle which com-

bined different techniques. Here we want to mention just the key points of our setup, which are: a two vacuum chamber setup, a laser system for cooling and detecting atoms, optics for imaging small atom clouds, computerized experiment control, diagnostic software, electronic components (switches, laser stabilization, light detection, ...) and low noise current sources.

After we were able to load a sufficiently large number of atoms into the initial trap (the copper Z), we developed a compression cycle for the magnetic trap in combination with a radio frequency ramp for evaporative cooling which was awarded with the successful creation of a Bose-Einstein condensate.

We studied the condensation process and basic properties of the Bose-Einstein condensate like the critical temperature T_C and the atom number. The used magnetic Z trap enabled us to excite collective shape oscillations of the Bose-Einstein condensate. This is done by changing the trap geometry in the radial direction from a relatively stiff trap (the initial trap) to a more shallow trap (final trap). Potential energy from the initial trap is converted into kinetic energy, which leads to a dynamic oscillation in the final trap. If we expand the Bose-Einstein condensate, the oscillation dynamics in the trap can be seen in the expansion characteristics (the shape of the cloud changes). Recording this behavior for a given expansion time and a variable time in the final trap, we can measure the longitudinal oscillation frequency.

Furthermore, due to the change from the initial to the final trap, we introduce in addition a position shift. This shift causes a center of mass motion in the radial direction of the final trap. When we open the trap after a variable time in the final trap, and monitor the position of the fallen cloud after a fixed expansion time, we can resolve this oscillation. Note here, that the measurement procedure for the collective shape oscillation and the center of mass motion is the same. This allows us to deduce both trap frequencies, the longitudinal and radial frequency, from the same experimental data.

In addition we studied the transfer of an ultra cold atom cloud from the copper structure to a Z shaped wire on the atom chip (a 200 μm wide and 2.2 μm thick wire, the central bar is 2 mm). Here we found, that due to a displacement of the atom chip with respect to the copper structure, the transfer is difficult. Nevertheless, we were able to develop a procedure, which enabled us to preserve the atom number and temperature.

Once on the atom chip, we were able to realize the so called two wire trap, which is a trap where no external bias field is needed. The gold Z wire on the chip provides the wire field, while the copper structure underneath (also a wire) provides the necessary bias field.

With the developed setup, we set the cornerstone for further atom chip experiments. The condensation cycle is well established and we were able

to perform initial experiments, which gave us an insight into condensate dynamics. This can be extended, as we investigated just the small perturbation regime. In principle it should be possible to investigate also large perturbations. In this regime, the presented theory breaks down (the kinetic part in the Gross-Pitaevskii equation can not be longer ignored), and new phenomena in the extreme nonlinear regime can be expected, including chaotic behavior.

The first step to future experiments should be the stable transportation or condensation of a Bose-Einstein condensate in a structure of the atom chip. The transport of a Bose-Einstein condensate from the copper structure to the gold Z was demonstrated in this setup, but we found that this transport bares the needed robustness. To improve this, the atom chip should be replaced, and when mounting it, the positioning with respect to the copper structure should be more accurate.

As the developed setup is flexible, the performed experiments just depend on the atom chip one puts into this setup. Experiments investigating atoms, confined in low dimensional traps, can be performed with little effort in changing the setup. Interferometric experiments investigating coherence/decoherence effects promise to give a better understanding of the involved physics. This will be necessary, because the use of atom chips in quantum information processing will depend on these decoherence effects.

The setup can also be combined with optical traps, as we took special care for good optical access during development. With this combination, another wide field opens up. For example an optical tweezer can be used to trap the Bose-Einstein condensate, which was generated in the copper structure, and by moving the focal point the Bose-Einstein condensate can be transferred to all locations on the atom chip [115]. This would further ease the use of the atom chip, because the entire surface can then be covered with wires for experiments, as the Bose-Einstein condensate must not be guided to the interesting wire region (at the moment the atom chip has a central trapping structure, the gold Z, and to each side experiments can be performed; with the proposed combination this restriction falls).

'Light' on the atom chip, in the sense of bringing the light to the chip with fibers, would also enrich the possibilities. It can be used to detect atoms, using optical cavities, or to collect light scattered from the atomic sample. These possibilities are currently investigated for a PhD thesis [69, 116].

As it was recently shown [60] it is also possible to combine magnetic wire traps with electrical fields. This combination will lead to traps, which depend on the internal state of the atom. This state depending trapping can be used for quantum information processing.

One sees from this short list, that the miniaturization of magnetic traps

leads to new experimental possibilities and thus to new insights into ultra cold atom physics.

Appendix A

⁸⁷Rb line data

Atomic number	Z	37
isotopic abundance	η	27.83%
mass number	A	87
Masse	m	$1.443 \cdot 10^{-24}$ kg
		86.909 u
density at 25°	ρ_m	1.53 g/cm ³
melting point	T _M	39.31°C
boiling point	T _B	688°C
vapor point at 25°C	P _V	$4.0 \cdot 10^{-7}$ mbar
nuclear spin	I	3/2

Table A.1: Physical properties of Rubidium 87

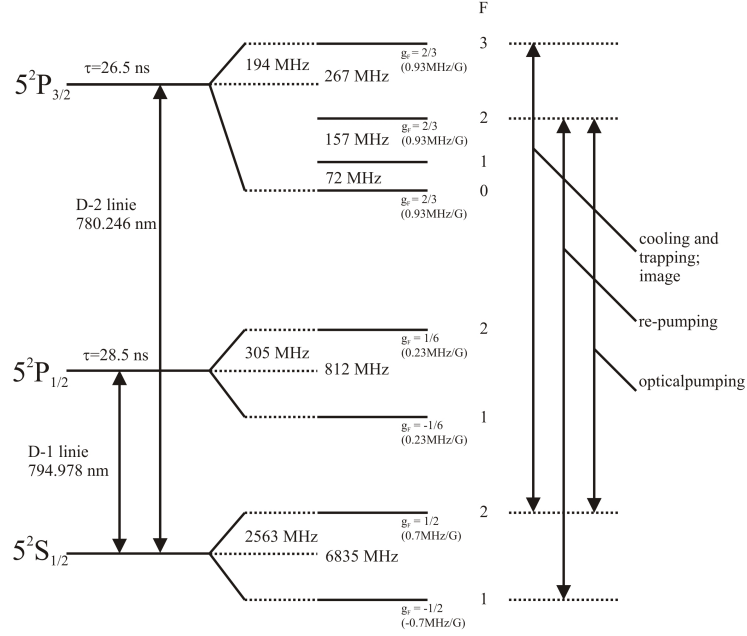


Figure A.1: The hyper fine energy scheme of the ^{87}Rb D 2 line. It shows all optical accessible transition, which are of interest in this work. The cooling and repumping transition as well as the transition for optical pumping and imaging are marked.

wavelength of the D2 line (vacuum)	λ	780.246291 nm
frequency	ω_0	$2\pi \cdot 384.227981877$ THz
life - time	τ	26.24 ns
natural linewidth	$\Gamma = \frac{1}{3\lambda^3\tau}$	$2\pi \cdot 6.065$ MHz
saturation intensity	$I_S = \frac{\pi\hbar c}{\lambda^3\tau}$	1.656 mW/cm ²
recoil velocity	$v_R = \frac{h}{\lambda m}$	5.8845 mm/s
recoil temperature	$T_r = \frac{\hbar^2}{3\lambda^2 m k_B}$	361.95 nK
Doppler temperature	$T_D = \frac{\hbar\Gamma}{2k_B}$	145.5 μK
s-wave scattering length of $^{87}\text{Rb}_2$ triplet state	a	$+106 \pm 4$ a ₀ $+5.6074 \pm 0.2116$ nm

Table A.2: Atom optical properties and most important units of Rubidium 87 for the D₂-line ($5^2S_{1/2} \rightarrow 5^2P_{3/2}$) if not otherwise mentioned [79]

Appendix B

The vacuum chamber

The vacuum chamber was built at the very beginning of our projects. The science chamber was built according to our accounts¹, and combines good optical access with the needs of the atom chip holder and current feed through. We used Helicoflex gaskets, as they allow us to minimize the distance window \rightarrow atomic sample (a small distance is needed for good imaging) and to use good optical windows.

In addition the science chamber was designed pan cake shaped. Here again the outline minimizes the distance outer contour \rightarrow atomic sample. This ensures also a good optical access and the possibility to use the chamber for a wider range of experiments. Note here, that we took special care in the choice of the used non magnetic steel in order to avoid residual magnetic fields.

¹Thanks to Toni Schönherr

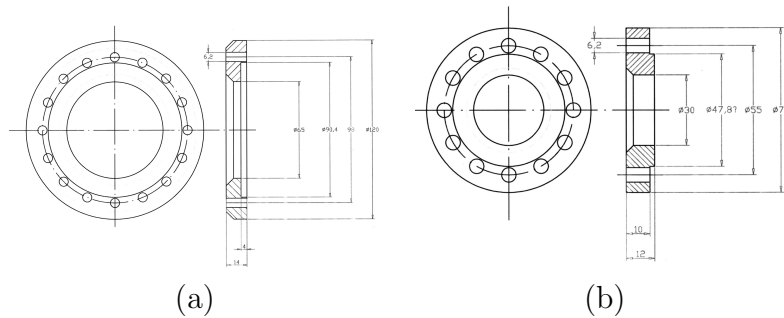


Figure B.1: The Helicoflex gaskets: the gaskets are pressed directly onto the chamber and the glass window. To keep it in position, stainless steel rings are used.

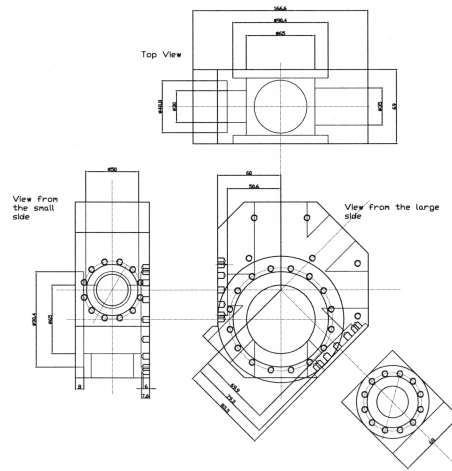


Figure B.2: The main body of the science chamber: it consists out of stainless steel and is hand fabricated. The shape and the used Helicoflex gaskets ensure good optical access and small atom \leftrightarrow window distances.

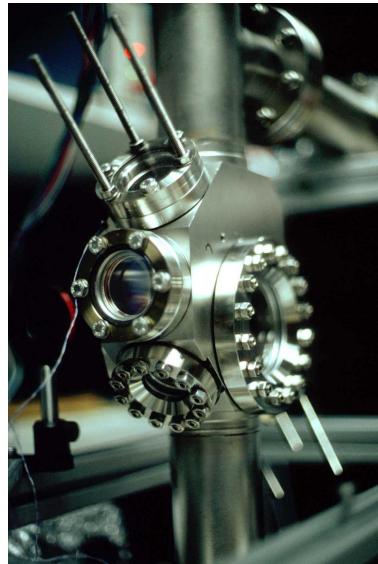


Figure B.3: The science chamber 'naked': the holding pins for the quadrupole coils and windows can be seen. The chamber was hand made. In the back ground the second Titanium sublimation pump is visible.

Appendix C

The H structure

The H structure, which provides the magnetic quadrupole field for the U-mirror MOT and the magnetic field for the Z-wire trap, was machined out of one piece of oxygen free copper, using a spark erosion technique. It is fitted into the Macor piece to a maximum in precession, as the copper H structure and the used bias fields should be perpendicular to each other.

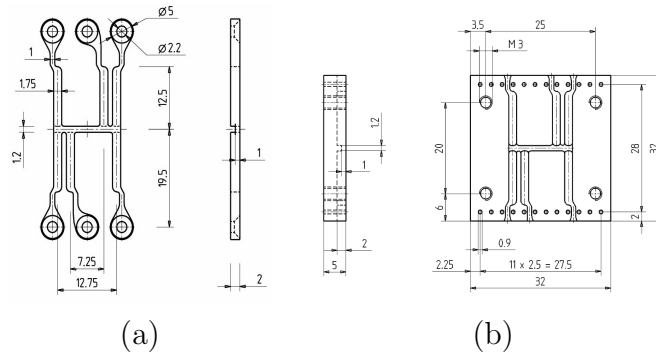


Figure C.1: The H structure: a) the copper structure is manufactured out of one piece of oxygen free copper, using a spark erosion technique; it is manufactured in house. b) the Macor piece: it is made to fit the copper H structure, and so provide mechanical support to it. Note here that the copper H structure and the Macor piece are made together, which means, that only two selected pieces belong to each other. This is necessary to ensure the mechanical support.

Appendix D

Complex analytical expressions

In general the displayed expressions were derived with Mathematica.

In section 3.2.2, we discussed the U-wire trap. The analytical expression for the fields is:

$$\begin{aligned} \vec{B}(x_0, 0, z_0) = & \left(\left[B_{bx} - \frac{ILz_0\mu_0}{2\pi r_0^2 \sqrt{L^2 + 4r_0^2}} \right]^2 \right. \\ & \left. + \left[B_{bz} - \frac{IL\mu_0}{2\pi(L^2 + 4z_0^2)} \left(\frac{-x_0(L^2 + 4r_0^2)}{r_0^2 \sqrt{L^2 + 4r_0^2}} + 2 \right) \right]^2 \right)^{1/2} \end{aligned} \quad (\text{D.1})$$

As we discussed in section 3.2.2, the Z-wire trap is slightly rotated around the x axis. When we calculate the trap frequencies (proportional to $\partial_j^2 B$) for this geometry we have to find new eigenvectors for the rotated system. This can be done by diagonalization of the Hesse matrix (see equation 3.2.2). The second derivative in the new coordinate system $(\tilde{x}, \tilde{y}, \tilde{z})$ are:

$$\begin{aligned} \frac{\partial^2 B}{\partial \tilde{x}^2} &= \frac{\mu_0 I}{16\pi z^5 (D^2 + 4z^2)^3} \cdot \\ & \quad (D^8 + 20D^6 z^2 + 144D^4 z^4 + 2^9 D^2 z^6 - 2^8 z^8 - \sqrt{R(D, z)}) \\ \frac{\partial^2 B}{\partial \tilde{y}^2} &= \frac{\mu_0 I}{16\pi z^5 (D^2 + 4z^2)^3} \cdot \\ & \quad (D^8 + 20D^6 z^2 + 144D^4 z^4 + 2^9 D^2 z^6 - 2^8 z^8 + \sqrt{R(D, z)}) \\ \frac{\partial^2 B}{\partial \tilde{z}^2} &= \frac{\mu_0 I}{8\pi z^5 (D^2 + 4z^2)^3} (D^8 + 20D^6 z^2 + 2^7 D^4 z^4 - 2^7 D^2 z^6 - 2^9 z^8) \end{aligned}$$

where

$$R(D, z) = L^{16} + 40L^{14}z^2 + 688L^{12}z^4 + 5248L^{10}z^6 + 18176L^8z^8 \\ + 30720L^6z^{10} + 13 * 2^{13}L^4z^{12} + 2^{16}L^2z^{14} + 2^{16}z^{16}$$

For a wire, which is broad and thick, the analytical solution¹ of the field in x and y direction is:

$$B(x) = \left(\frac{-j\mu_0}{4\pi} \right) * \left(\left(\frac{W}{2} + x \right) \log \left(\frac{\left(\frac{W}{2} + x \right)^2 + \left(\frac{H}{2} + y \right)^2}{\left(\frac{W}{2} + x \right)^2 + \left(\frac{-H}{2} + y \right)^2} \right) \right. \\ - \left(\frac{-W}{2} + x \right) \log \left(\frac{\left(\frac{-W}{2} + x \right)^2 + \left(\frac{H}{2} + y \right)^2}{\left(\frac{-W}{2} + x \right)^2 + \left(\frac{-H}{2} + y \right)^2} \right) \left(\frac{H}{2} + y \right) \\ \left(\arccos \left(\frac{\left(\frac{W}{2} + x \right)^2 - \left(\frac{H}{2} + y \right)^2}{\left(\frac{W}{2} + x \right)^2 + \left(\frac{H}{2} + y \right)^2} \right) - \arccos \left(\frac{\left(\frac{-W}{2} + x \right)^2 - \left(\frac{H}{2} + y \right)^2}{\left(\frac{-W}{2} + x \right)^2 + \left(\frac{H}{2} + y \right)^2} \right) \right) \\ \left(\frac{-H}{2} + y \right) \left(\arccos \left(\frac{\left(\frac{W}{2} + x \right)^2 - \left(\frac{-H}{2} + y \right)^2}{\left(\frac{W}{2} + x \right)^2 + \left(\frac{-H}{2} + y \right)^2} \right) \right. \\ \left. \left. - \arccos \left(\frac{\left(\frac{-W}{2} + x \right)^2 - \left(\frac{-H}{2} + y \right)^2}{\left(\frac{-W}{2} + x \right)^2 + \left(\frac{-H}{2} + y \right)^2} \right) \right) \right)$$

For the $B(y)$ component, one has to exchange W and H, x and y and the $-j$ becomes j .

¹the derivation was done by S. Aigner

Appendix E

Power supplies and noise

In figure 4.30 the signal of a current probe, which measures the Z and the Y-bias current is shown. This current probe is implemented in external switches, and it allows a ground free measurement. With the external switches we can generally reach switching times of $< 20 \mu s$.

The used power supplies¹ can be operated in two modes, the current and the voltage control mode. Figure E.1 shows the noise spectra of the two modes. As can be seen, the current control mode (CC) gives out more noise than the voltage control mode (CV), therefore the supply is operated in the CV mode.

Controlling the devices is performed by applying a voltage to the power supply, and according to this, the supply gives out the appropriate voltage. The current is then according to the load resistance, in our case the copper Z structure. When we operate the Z wire for a long time (~ 20 s), we see a drop in the current due to a change in the resistivity of the Z wire. This current drop is ~ 300 mA, and is acceptable for the performed experiments.

To be noise free means in general, that the electronic circuit has to be slow in its bandwidth. Therefore, it would respond to the controlling commands slow. To achieve fast switch on times (in the order of ~ 2 ms), a trick is used. The external switch is closed, but the control voltage is set to the maximum value. This causes the power supply to give out its maximum voltage, but because the switch is closed, no current can flow. The power supply is 'preloaded'. Then the switch is opened, and simultaneously the control value is ramped down to the value that corresponds to the desired current. With this method we can ramp up the current on the needed scale, still depending on the inductance of the load, but faster than the supply specifications (the specification is 20 ms).

¹Z: Agilent 6651A; Y: Agilent 6641A

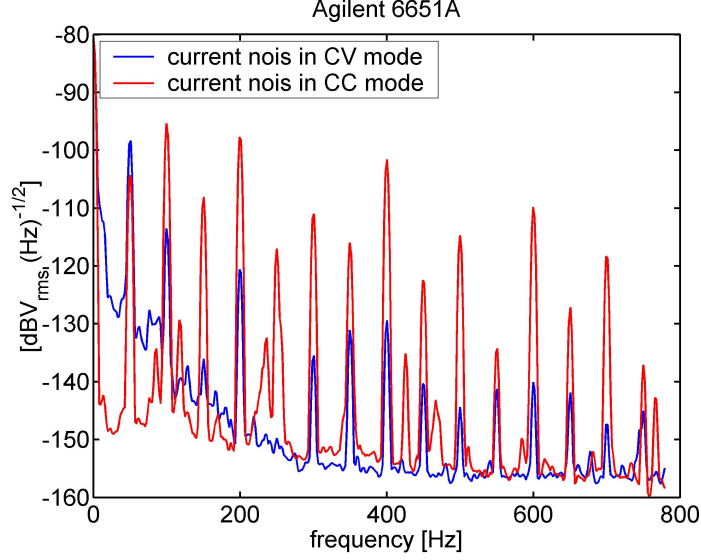


Figure E.1: Current noise spectra of the different operation modes: the power supply runs on 50 A. The noise is measured across a $0.01\ \Omega$ resistance (holds 80 W). The used spectrum analyzer (Stanford Research Systems, SR760) has a span of 780 Hz with a 1.95 Hz resolution. The blue curve is for CV operation. One sees that the noise peaks (multiples of 50 and 100 Hz) decline faster than the noise peaks in the CC mode (red curve). The noise floor of the CV mode is also slightly lower.

For experiments on the atom chip we developed a special power supply. Here we took car batteries, in order to avoid noise from the line. In figure E.3 the circuit diagram is shown. The main part is a IGBT chip, which regulates the current. To be able to run the atom chip completely independent of the environment function generator was developed (also battery operated), capable to give out arbitrary voltage ramps. It can replace the experimental computer control system.

Noise spectra of the current source (see printed circuit E.3) reveal, that the developed devices are 30dB better.

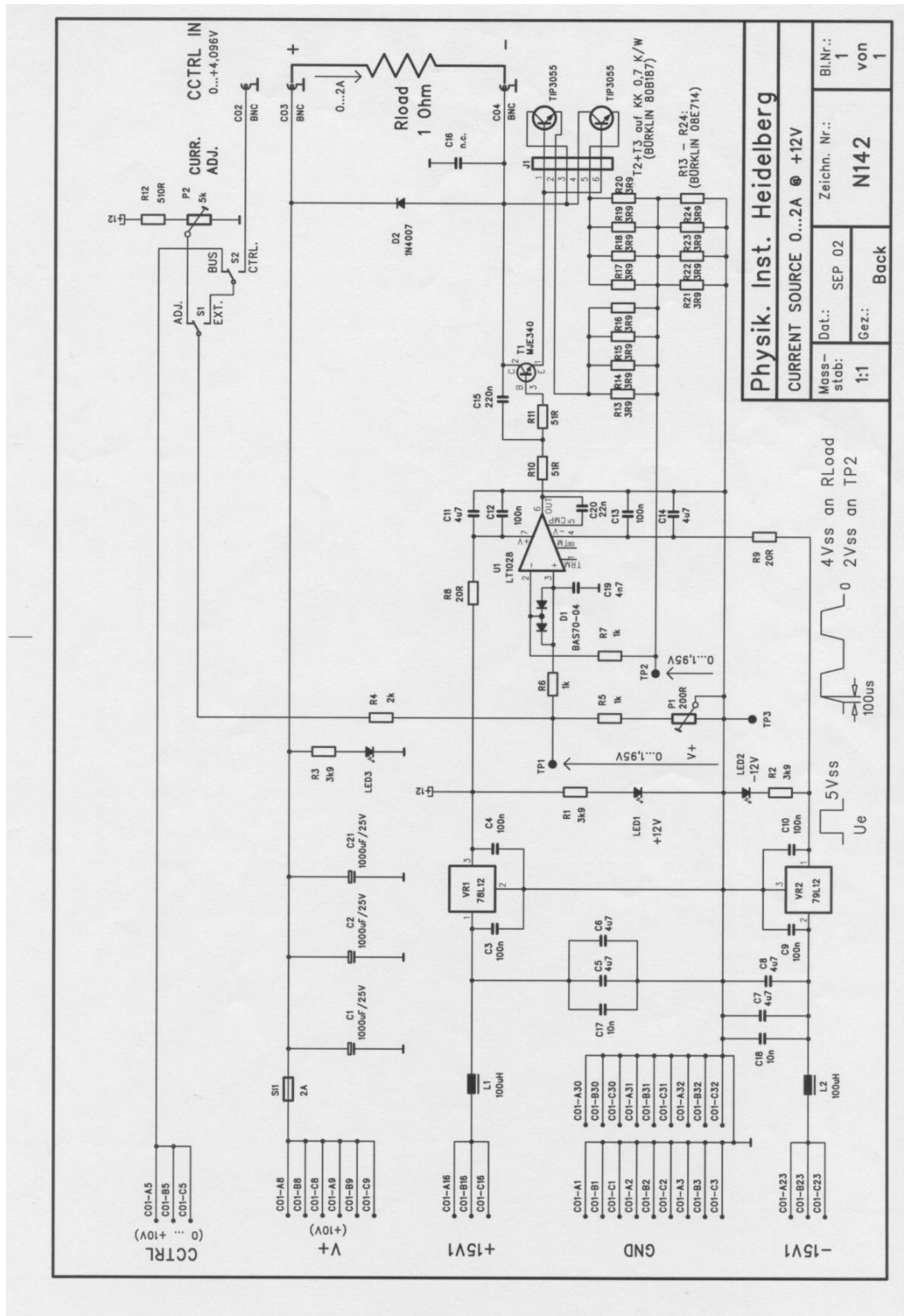


Figure E.2: Current supply for the atom chip: the developed circuit is supplied by a car battery. It can be operated only in 'constant current' mode. We took special care in effectively shielding against electric noise background, which could be picked up.

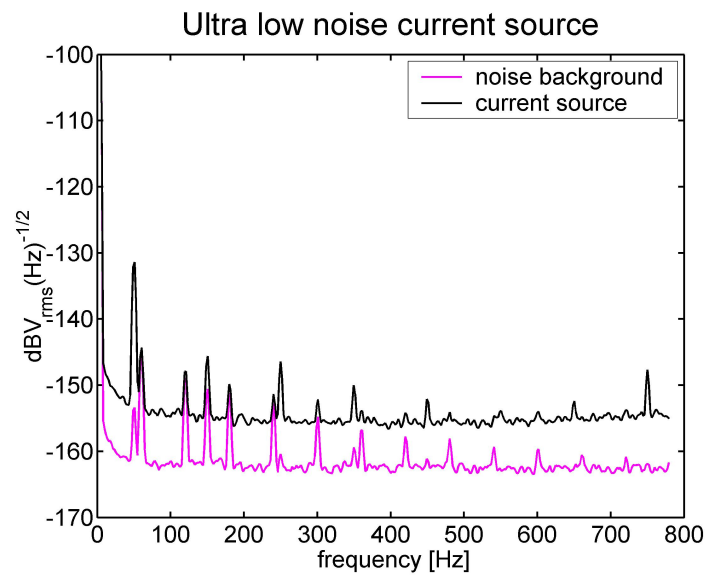


Figure E.3: Noise spectra of the self build current supplies: the spectra is 30dB better (less noise) as the spectra displayed in figure E.1.

Appendix F

Computer control

The experiment is entirely controlled by a computer based system named LABVIEW. It was mainly designed by St. Schneider [100] and is described there in detail. Here we give a short summary.

We have two main output cards for analog (12-Bit, 8 channels) as well as digital (TTL, 10 channels) signals. They are synchronized by the same clock, which ensures accurate timing. The time resolution in the experiment is 1 ms. As mentioned, we use a programmable function generator for our radio frequency ramp. This function generator is programmed via a GPIB card, which is synchronized to the two other cards.

Here we have to mention an important point. The Frequency generator can not be externally triggered. We therefore load via the GPIB connection the needed frequency ramp into the memory of the function generator, and when the loading is finished, the function generator gives out a TTL signal, which subsequently starts the complete experimental cycle. This method, although complicated, ensures perfect timing between the analog, TTL and radio frequency signals. In addition we have an analog-in card, which allows us to read in analog signals. The computer program controls all the cards, and allows a easy change of the output signals (see figure below).

As we developed the system, we had to realize that we need more channels to operate the experiment. We therefore introduced gate generators for selected channels. These channels had to fulfill the requirement, that we did not need to change the timing between pulses. The camera pulse sequence is a good example. We need three pulses for the camera to get three pictures (atoms and light, just light, no light at all). The pulse delays are always the same, and therefore we used one LABVIEW pulse to generate the pulse sequence. With the same LABVIEW pulse we also triggered the AOM, which provides the light for the absorption imaging. As we had also some logic components, it was easy to generate in this way five pulses from

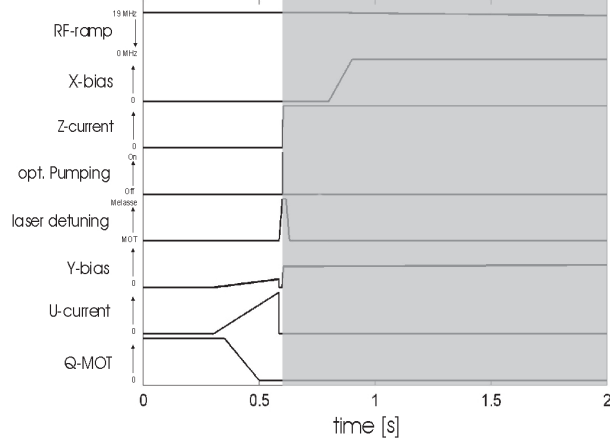


Figure F.1: Timing sequence: the figure shows the beginning of the experimental cycle, where we load the atoms from the Q-mirror MOT to the U-mirror MOT and then into the copper Z-trap.

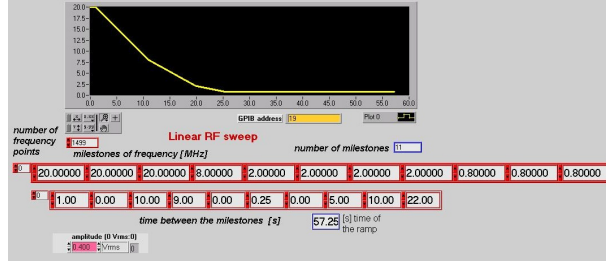


Figure F.2: Analog Pulse sequence needed to load the atoms from the Q-mirror MOT to the U-mirror MOT and subsequently to the copper Z trap.

one LABVIEW pulse.

In figure F.1 the analog pulse sequence is displayed. As mentioned, the power supplies are operated with voltage ramps (they give out according to the input voltage current ramps). The sequence show the analog ramps needed to transfer the atoms from the Q-mirror MOT to the U-mirror MOT and subsequently to the copper Z trap. Figure F.3 show the LABVIEW front end, in this case for the TTL signals. Figure F.2, shows the panel we use to program the function generator. Different radio frequency ramps can be programmed.

Figure F.4 shows the mentioned gate generators. Even they are from 'ancient times', they where reliable and precise (on a ns scale!).

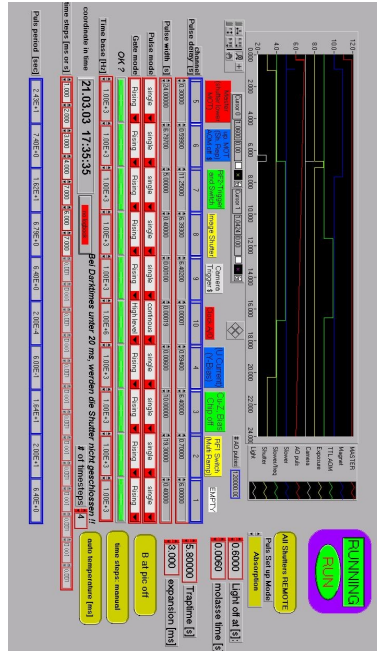


Figure F.3: TTL computer panel: here the timing of the used TTL pulses can be adjusted.

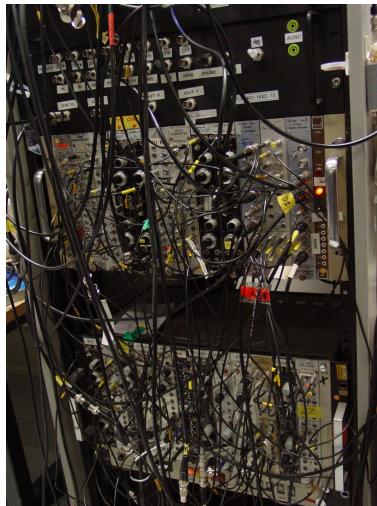


Figure F.4: The gate generators: analog rules!

Bibliography

- [1] Satyendra Bose. Plancks Gesetz und Lichtquantenhypothese. *Z. f. Phys.*, 26(3):178, 1924.
- [2] A. Einstein. Quantentheorie des einatomigen idealen Gases. *Sitzungber. Preuss. Akad. Wiss.*, 1924:261, July 1924.
- [3] A. Einstein. Quantentheorie des einatomigen idealen Gases. Zweite Abhandlung. *Sitzungber. Preuss. Akad. Wiss.*, 1925:3, January 1925.
- [4] E.L. Raab, M. Prentiss, A. Cable, S. Chu, and D.E. Pritchard. Trapping of neutral sodium atoms with radiation pressure. *Phys. Rev. Lett.*, 59(23):2631, December 1987.
- [5] J.E. Bjorkholm, R.E. Freeman, A. Ashkin, and D.B. Pearson. Observation of focusing on neutral atoms by the dipole forces of resonance-radiation pressure. *Phys. Rev. Lett.*, 41(20):1361, November 1978.
- [6] V.S. Bagnato, G.P. Lafyatis, A.G. Martin, E.L. Raab, R.N. Ahmad-Bitar, and D.E. Pritchard. Continuous stopping and trapping of neutral atoms. *Phys. Rev. Lett.*, 58(21):2194, May 1987.
- [7] A.L. Migdall, J.V. Prodan, W.D. Phillips, T.H. Bergeman, and H.J. Metcalf. First observation of magnetically trapped neutral atoms. *Phys. Rev. Lett.*, 54(24):2596, June 1985.
- [8] Harald F. Hess, David A. Bell, Gregory P. Kochanski, Richard A. Cline, Daniel Kleppner, and Thomas J. Greytak. Observation of three-body recombination in spin-polarized hydrogen. *Phys. Rev. Lett.*, 51(6):483, August 1983.
- [9] O.J. Luiten, M.W. Reynolds, and J. T. M. Walraven. Kinetic theory of the evaporative cooling of a trapped gas. *Phys. Rev. A*, 53(1):381, January 1996.

- [10] M.H. Anderson, J.R. Ensher, M.R. Matthews, C.E. Wieman, and E.A. Cornell. Observation of Bose-Einstein condensation in a dilute atomic vapor. *Science*, 269(0):198, July 1995.
- [11] K.B. Davis, M.-O. Mewes, M.R. Andrews, N.J. van Druten, D.S. Durfee, D.M. Kurn, and W. Ketterle. Bose-Einstein condensation in a gas of sodium atoms. *Phys. Rev. Lett.*, 75(22):3969, November 1995.
- [12] C.C. Bradley, C.A. Sackett, J.J. Tollett, and R.G. Hulet. Evidence of Bose-Einstein condensation in an atomic gas with attractive interactions. *Phys. Rev. Lett.*, 75(9):1687, August 1995. *ibid.* **79**, 1170 (1997).
- [13] Dale G. Fried, Thomas C. Killian, Lorenz Willmann, David Landhuis, Stephen C. Moss, Daniel Kleppner, and Thomas J. Greytak. Bose-Einstein condensation of atomic hydrogen. *Phys. Rev. Lett.*, 81(18):3811, November 1998.
- [14] S.L. Cornish, N.R. Claussen, J.L. Roberts, E.A. Cornell, and C.E. Wieman. Stable ^{85}Rb Bose-Einstein condensates with widely tunable interactions. *Phys. Rev. Lett.*, 85(9):1795, August 2000.
- [15] G. Modugno, G. Ferrari, G. Roati, R.J. Brecha, A. Simoni, and M. Inguscio. Bose-Einstein condensation of Potassium atoms by sympathetic cooling. *Science*, 294:1320, 2001.
- [16] A. Robert, O. Sirjean, A. Browaeys, J. Poupard, S. Nowak, D. Bori on, C.I. Westbrook, and A. Aspect. A Bose-Einstein condensate of metastable atoms. *Science*, 292(461):461, 2001.
- [17] F.P. Dos Santos, J. L eonard, J. Wang, C. J. Barellelet, and C. Cohen-Tannoudji. Bose-Einstein condensation of metastable Helium. *Phys. Rev. Lett.*, 86:3459, 2001.
- [18] T. Weber, J. Herbig, M. Mark, H.-C. N agerl, and R. Grimm. Bose-Einstein condensation of Cesium. *Science*, 299:232, 2003.
- [19] Y. Takasu, K. Maki, K. Komori, T. Takano, K. Honda, and M. Kumakura. Spin-singlet Bose-Einstein condensation of two-electron atoms. *Phys. Rev. Lett.*, 91(4):040404, July 2003.
- [20] J. Schmiedmayer. A wire for neutral atoms. *Appl. Phys. B*, 60:169, 1995.
- [21] J. Schmiedmayer. Guiding and trapping a neutrap atom on a wire. *Phys. Rev. A*, 52:R13, 1995.

- [22] J. Denschlag, D. Cassettari, A. Chenet, S. Schneider, and J. Schmiedmayer. A neutral atom and a wire: towards mesoscopic atom optics. *Appl. Phys. B*, 49(4):257, October 1999.
- [23] J. Reichel, W. Hänsel, and T.W. Hänsch. Atomic micromanipulation with magnetic surface traps. *Phys. Rev. Lett.*, 83(17):3398, 1999.
- [24] J. Fortagh, A. Grossmann, C. Zimmermann, and T.W. Hänsch. Miniaturized wire trap for neutral atoms. *Phys. Rev. Lett.*, 81(24):5310, December 1998.
- [25] R. Folman, P. Krüger, J. Denschlag, C. Henkel, and J. Schmiedmayer. Microscopic atom optics: From wires to an atom chip. *Adv. At. Mol. Opt. Phys.*, 48:263, 2002.
- [26] H. Ott, J. Fortágh, G. Schlotterbeck, and C. Zimmermann. Bose-einstein condensation in a surface microtrap. *Phys. Rev. Lett.*, 87(23):230401, December 2001.
- [27] W. Hänsel, P. Hommelhof, T. W. Hänsch, and J. Reichel. Bose-Einstein condensation on a microelectronic chip. *Nature*, 413:498, 2001.
- [28] S. Schneider, A. Kasper, Ch. vom Hagen, M. Bartenstein, B. Engeser, T. Schumm, I. Bar-Joseph, R. Folman, L. Feenstra, and J. Schmiedmayer. Bose-Einstein condensation in a simple microtrap. *Phys. Rev. A*, 67:023612, April 2003.
- [29] A. Kasper, S. Schneider, Ch. vom Hagen, M. Bartenstein, B. Engeser, T. Schumm, I. Bar-Joseph, R. Folman, L. Feenstra, and J. Schmiedmayer. A Bose-Einstein condensate in a microtrap. *J. Opt. B*, 5.
- [30] Franco Dalfovo, Stefano Giorgini, Lev P. Pitaevskii, and Sandro Stringari. Theory of Bose-Einstein condensation in trapped gases. *Rev. Mod. Phys.*, 71(3):463, April 1999.
- [31] C. J. Pethick and H. Smith. *Bose-Einstein Condensation in Dilute Gases*. Cambridge University Press, 2002.
- [32] V.S. Bagnato, D.E. Pritchard, and D. Kleppner. Bose-Einstein condensation in an external potential. *Phys. Rev. A*, 35(10):4354, May 1987.
- [33] Wolfgang Ketterle and N.J. van Druten. Bose-Einstein condensation of a finite number of particles trapped in one or three dimensions. *Phys. Rev. A*, 54(1):656, July 1996.

- [34] Klaus Kirsten and David J. Toms. Bose-Einstein condensation of atomic gases in a general harmonic-oscillator confining potential trap. *Phys. Rev. A*, 54(5):4188, November 1996.
- [35] N. Bogolubov. On the theory of superfluidity. *J. Phys.*, 11(1):23, 1947.
- [36] J. Weiner, V.S. Bagnato, S. Zilio, and P.S. Julienne. Experiments and theory in cold and ultra cold collisions. *Rev. Mod. Phys.*, 71:1, 1999.
- [37] E.P. Gross. Structure of a quantized vortex in boson systems. *Nuovo Cimento*, 20(0):454, 1995.
- [38] L.P. Pitaevskii. Vortex lines in an imperfect Bose gas. *Sov. Phys. JETP*, 13(2):451, August 1961.
- [39] Philippe Nozières and David Pines. *The Theory of Quantum Liquids, Vol. II Superfluid Bose Liquids*. Addison-Wesley, 1990.
- [40] Y. Castin and R. Dum. Bose-Einstein condensates in time-dependent traps. *Phys. Rev. Lett.*, 77(27):5315, December 1996.
- [41] S. Stringari. Collective excitations of a trapped Bose-condensed gas. *Phys. Rev. Lett.*, 77(12):2360, September 1996.
- [42] Yu. Kagan, E.L. Surkov, and G.V. Shlyapnikov. Evolution of a Bose gas in anisotropic time-dependent traps. *Phys. Rev. A*, 55(1):R18, January 1997.
- [43] Yu. Kagan, E.L. Surkov, and G.V. Shlyapnikov. Evolution of a Bose-condensed gas under variations of the confining potential. *Phys. Rev. A*, 54(3):R1753, September 1996.
- [44] H.Nyquist. Certain topics in telegraph transmission theory. *Trans. AIEE*, 47:617, 1928.
- [45] C.E. Shannon. Communication in the presence of noise. *Proc. Institute of Radio Engineers*, 37(1):10, 1949.
- [46] A. Einstein. Quantentheorie der Strahlung. *Phys. Zeits.*, 13:121, 1917.
- [47] O.R. Frisch. Experimenteller Nachweis des Einsteinschen Strahlungsrückstosses. *Z. f. Phys.*, 86(42), 1933.
- [48] T.W. Hänsch and A.L. Schawlow. Cooling of gases by laser radiation. *Opt. Commun.*, 13(1):68, January 1975.

- [49] D.J. Wineland and H.G. Dehmelt. Proposed $10^{14}\delta\nu/\nu$ laser fluorescence spectroscopy on Ti^+ mono ion oscillator. *Bull. Am. Phys. Soc.*, 20:637, 1975.
- [50] W.D. Phillips. Laser cooling, optical traps and optical molasses. In J. Zinn-Jusbin J. Dalibard, J.M. Raimond, editor, *Fundamental systems in quantum optics, Les Houches 1990*, page 169. North-Holland, Amsterdam, 1992.
- [51] H. J. Metcalf and P. van der Straten. *Laser Cooling and Trapping*. Springer, New York, 1999.
- [52] A. Ashkin and J.P. Gordon. Stability of radiation pressure traps: an optical Earnshaw theorem. *Opt. Lett.*, 8:511, 1983.
- [53] K. Lindquist, M. Stephens, and C. Wieman. Experimental and theoretical study of the vapor-cell Zeeman optical trap. *Phys. Rev. A*, 46(7):4082, 1992.
- [54] C.G. Townsend, N.H. Edwards, C.J. Cooper, K.P. Zetie, C.J. Foot, A.M. Steane, P. Szriftgiser, H. Perrin, and J. Dalibard. Phase-space density in the magneto-optical trap. *Phys. Rev. A*, 52(2):1423, August 1995.
- [55] J. Dalibard and C. Cohen-Tannoudji. Laser cooling below the Doppler limit by polarization gradients: simple theoretical-models. *J. Opt. Soc. Am. B*, 6(11):2023, November 1989.
- [56] R. Grimm, M. Weidemüller, and Yu.B. Ovchinnikov. Optical dipole traps for neutral atoms. *Adv. At. Mol. Opt. Phys.*, 42:95, 2000.
- [57] W. Wing. On neutral particle trapping in quasistatic electromagnetic fields. *Prog. Quant. Elect.*, 8.
- [58] Wolfgang Ketterle and David E. Pritchard. Trapping and focusing ground state atoms with static fields. *Appl. Phys. B*, 54:403, 1992.
- [59] L.V. Hau, M.Burns, and J.A. Golovchenko. Bond states of guided matter waves: An atom and a charged wire. *Phys. Rev. A*, 45:6468, 1992.
- [60] P. Krüger, X. Luo, M.W. Klein, K. Brugger, A. Haase, S. Wildermuth, S. Groth, I. Bar-Joseph, R. Folman, and J. Schmiedmayer. Trapping and manipulating neutral atoms with electrostatic fields. In *arXiv:quant-ph/0306111v1*, 2003.

- [61] J. Denschlag. *Kalte Atome in singulären Potentialen*. PhD thesis, University of Innsbruck, 1999.
- [62] J. Denschlad, D. Cassetari, and J. Schmiedmayer. Guiding neutral atoms with a wire. *Phys. Rev. Lett.*, 82(10):2014, March 1999.
- [63] C.V. Sukumar and D.M. Brink. Spin-flip transitions in a magnetic trap. *Phys. Rev. A*, 56(3):2451, September 1997.
- [64] S. Gove and H. Thomas. Magnetic trapping of neutral particles: Classical and quantum-mechanical study of a Ioffe-Pritchard type trap. *J. Appl. Phys.*, 87:3989, 2000.
- [65] J.D. Weinstein and K.G. Lipprecht. Microscopic magnetic traps for neutral atoms. *Phys. Rev. A*, 52(5):4004, 1995.
- [66] A. Haase, D. Cassettari, B. Hessmo, and J. Schmiedmayer. Trapping neutral atoms with a wire. *Phys. Rev. A*, 64:043405, 2001.
- [67] T. Schumm. Auf dem Weg zu einem Rubidium 87 Bose-Einstein Kondensat in magnetischen Drahtfallen. Diploma thesis, Universität Heidelberg/Freie Universität Berlin, 2001.
- [68] C. Becker. Eine neuartige magnetooptische falle für Atomchip-Experimente. Diploma thesis, Universität Heidelberg, 2002.
- [69] A. Haase. Trapping atoms with a paperclip. Diploma thesis, Universität Innsbruck/Freie Universität Berlin, 2000.
- [70] J. Reichel. Microchip traps and Bose-Einstein condensation. *Appl. Phys. B*, 75:469, 2002.
- [71] A.E. Leanhardt, A.P. Chikkatur, D. Kieplinski, Y. Shin, T.L. Gustavson, W. Ketterle, and D.E. Pritchard. Propagation of a Bose-Einstein condensate in a magnetic waveguide. *Phys. Rev. Lett.*, 89:040401, 2002.
- [72] C. Henkel, P. Krüger, R. Folman, and J. Schmiedmayer. Fundamental limits for coherent manipulation on atom chips. *Appl. Phys. B*, 76:173, 2003.
- [73] M.E. Gehm, K.M. O'Hara, T.A. Savard, and J.E. Thomas. Dynamics of noise-induced heating in atom traps. *Phys. Rev. A*, 58(5):3914, November 1998.

- [74] Harald F. Hess. Evaporative cooling of magnetically trapped and compressed spin-polarized hydrogen. *Phys. Rev. B*, 34(5):3476, September 1986.
- [75] Wolfgang Ketterle and David E. Pritchard. Atom cooling by time-dependent potentials. *Phys. Rev. A*, 46(7):4051, October 1992.
- [76] K.B. Davis, M.-O. Mewes, and W. Ketterle. An analytical model for evaporative cooling of atoms. *Appl. Phys. B*, 60:155, 1995.
- [77] Wolfgang Ketterle and N.J. van Druten. Evaporative cooling of trapped atoms. *Adv. At. Mol. Opt. Phys.*, 37(0):181, 1996.
- [78] J. Söding, D. Guéry-Odelin, P. Desbiolles, F. Chevy, H. Inamori, and J. Dalibard. Three-body decay of a rubidium Bose-Einstein condensate. *Appl. Phys. B*, 69(4):257, October 1999.
- [79] D.A. Steck. Rubidium 87 D Line Data, 2002. Los Alamos National Laboratory, <http://george.ph.utexas.edu/dsteck/alkalidata/rubidium87numbers.pdf>.
- [80] B. Dahmani, L. Hollberg, and R. Drullinger. Frequency stabilization of semiconductor lasers by resonant optical feedback. *Opt. Lett.*, 12(11):876, 1987.
- [81] A. Hemmerich, D.H. McIntyre, D. Schropp, D. Meschede, and T.W. Hänsch. Optically stabilized narrow linewidth semiconductor laser for high resolution spectroscopy. *Opt. Comm.*, 75(2):118, 1990.
- [82] M.G. Boshier, D. Berkeland, E.A. Hinds, and V. Sandoghdar. External-cavity frequency-stabilization of visible and infrared semiconductor lasers for high resolution spectroscopy. *Opt. Comm.*, 85(4):355, 1991.
- [83] C.E. Wiemann and L. Hollberg. Using diode laser for atomic physics. *Rev. Sci. Instrum.*, 62(1):1, 1991.
- [84] L. Ricci, M. Weidemüller, T. Esslinger, A. Hemmerich, C. Zimmermann, V. Vuletic, W. König, and T.W. Hänsch. A compact grating-stabilized diode laser system for atomic physics. *Opt. Comm.*, 117:541, 1995.
- [85] Wolfgang Demtröder. *Laserspektroskopie. Grundlagen und Techniken*. Springer Verlag, Heidelberg, 2000.

- [86] P. Horowitz and W. Hill. *The art of electronics*. Cambridge university press, 1989.
- [87] M. Rückel. Frequenzstabilisierung eines Diodenlasers über das Frequency-Offset-Locking. Diploma thesis, Universität Heidelberg, 2002.
- [88] R.W.P. Drever, J.L. Hall, F.V. Kowalski, J.Hough, G.M. Ford, A.J. Munley, and H. Ward. Laser phase and frequency stabilization using an optical resonator. *Appl. Phys. B*, 31:97, 1983.
- [89] G.C. Bjorklund, M.D. Levenson, W. Lenth, and C. Ortiz. Frequency modulation (FM) spectroscopy. *Appl. Phys. B*, 32:145, 1983.
- [90] U. Schünemann, H. Engler, R. Grimm, M. Weidemüller, and M. Zielonkowski. Simple scheme for tunable frequency offset-locking of two lasers. *Rev. Sci. Instrum*, 70:242, 1999.
- [91] S. Haupt. Setup of a new experiment with ultracold ^{87}Rb atoms: Towards quantum information processing on an atom chip. Diploma thesis, Universität Heidelberg, 2003.
- [92] K. Petermann. *Laser diode modulation and noise*. Kluwer Academic Publisher, 1991.
- [93] F. Mogensen, H. Olesen, and Jacobsen G. Locking conditions and stability properties for a semiconductor laser with external light injection. *IEEE J. Quantum Electron.*, 21:784, 1985.
- [94] H. Rohde. Injektionsstabilisierung von Laserdioden. Diploma thesis, Universität Innsbruck, 1996.
- [95] A. Kasper. Stabilisierung eines Diodenlasers bei 670nm. Diploma thesis, Universität Innsbruck, 1999.
- [96] S. Schneider. *Me and The Machine ... Experiments with Bose-Einstein Condensation of ^{87}Rb* . PhD thesis, University of Heidelberg, 2003.
- [97] C.v.Hagen. Bose-Einstein condensation in a surface mounted wire trap - from a large scale wire trap to an atom chip. Diploma thesis, Universität Heidelberg, 2003.
- [98] K.I. Lee, J.A. Kim, H.R. Noh, and W. Jhe. Single-beam atom trap in a pyramidal and conical hollow mirror. *Opt. Lett*, 21(15):1177, March 1996.

- [99] W. Wohlleben, F. Chevy, K. Madison, and J. Dalibard. An atom faucet. *Eur. Phys. J. D*, 15:237, 2001.
- [100] St. Schneider. *Bose-Einstein Kondensation in einer magnetischen Z-Falle*. PhD thesis, Universität Heidelberg, 2003.
- [101] M. Bartenstein. Aufbau und Charakterisierung einer kontinuierlich betriebenen Doppel-MOT für ^{87}Rb . Diploma thesis, Universität Innsbruck/Freie Universität Berlin, 2001.
- [102] C. Cassetari. *Cold atoms in microscopic traps: from wires to chips*. PhD thesis, Universität Innsbruck, 2000.
- [103] J. Schuster. *Stoßlawinen in einem Bose-Einstein Kondensat*. PhD thesis, LMU München, 2000.
- [104] W. Ketterle, D.S. Durfee, and D.M. Stamper-Kurn. Making, probing and understanding Bose-Einstein condensates. In M. Inguscio, S. Stringari, and C.E. Wieman, editors, *Proceedings of the International School of Physics - Enrico Fermi*, page 67. IOS Press, 1999.
- [105] K. Dieckmann. *Bose-Einstein condensation with high atom number in a deep trap*. PhD thesis, Universiteit van Amsterdam, 2001.
- [106] B. Engeser. Optische Abbildung einer atomaren Dichteverteilung. Diploma thesis, Universität Heidelberg, 2002.
- [107] T. Strassel. Xxx. Diploma thesis, Universität Heidelberg, 2003.
- [108] Yu. Kagan. Kinetics of Bose-Einstein condensate formation in an interacting Bose gas. In A. Griffin, D.W. Snoke, and S. Stringari, editors, *Bose-Einstein Condensation*, page 202. Cambridge University Press, 1995.
- [109] U. Ernst, A. Marte, F. Schreck, J. Schuster, and G. Rempe. Bose-Einstein condensation in a pure Ioffe-Pritchard field configuration. *Europhys. Lett.*, 41(1):1, January 1998.
- [110] M.-O. Mewes, M.R. Andrews, N.J. van Druten, D.M. Kurn, D.S. Durfee, C.G. Townsend, and W. Ketterle. Collective excitations of a Bose-Einstein condensate in a magnetic trap. *Phys. Rev. Lett.*, 77(6):988, August 1996.

- [111] D.M. Stamper-Kurn, H.-J. Miesner, S. Inouye, M.R. Andrews, and W. Ketterle. Collisionless and hydrodynamic excitations of a Bose-Einstein condensate. *Phys. Rev. Lett.*, 81(3):500, July 1998.
- [112] H. Ott, J. Fortágh, S. Kraft, A. Günther, D. Komma, and C. Zimmermann. Nonlinear dynamics of a Bose-Einstein condensate in a magnetic waveguide. *Phys. Rev. Lett.*, 91(4):040402, July 2003.
- [113] D.S. Jin, M.R. Matthews, J.R. Ensher, C.E. Wieman, and E.A. Cornell. Temperature-dependent damping and frequency shifts in collective excitations of a dilute Bose-Einstein condensate. *Phys. Rev. Lett.*, 78(5):764, February 1997.
- [114] D.S. Jin, J.R. Ensher, M.R. Matthews, C.E. Wieman, and E.A. Cornell. Collective excitations of a Bose-Einstein condensate in a dilute gas. *Phys. Rev. Lett.*, 77(3):420, July 1996.
- [115] T.L. Gustavson, A.P. Chikkatur, A.E. Leanhardt, A. Görlitz, A. Gupta, D.E. Pritchard, and W. Ketterle. Transport of Bose-Einstein condensates with optical tweezers. *Phys. Rev. Lett.*, 88(2):020401, December 2001.
- [116] M. Wilzbach. Aufbau eines Experiments zur miniaturisierten und integrierten Detektion neutraler Atome. Diploma thesis, Universität Heidelberg, 2002.